PROBING SUPERGRAVITY UNIFIED THEORIES AT THE LARGE HADRON COLLIDER

A dissertation presented

by

Zuowei Liu

to
The Department of Physics

In partial fulfilment of the requirements for the degree of
Doctor of Philosophy

in the field of

Physics

Northeastern University
Boston, Massachusetts
August, 2008

PROBING SUPERGRAVITY UNIFIED THEORIES AT THE LARGE HADRON COLLIDER

by

Zuowei Liu

ABSTRACT OF DISSERTATION

Submitted in partial fulfillment of the requirement
for the degree of Doctor of Philosophy in Physics
in the Graduate School of Arts and Sciences of
Northeastern University, August, 2008

Abstract

The discovery of supersymmetry is one of the major goals of the current experiments at the Tevatron and in proposed experiments at the Large Hadron Collider (LHC). However when sparticles are produced the signatures of their production will to a significant degree depend on their hierarchical mass patterns. Here we investigate hierarchical mass patterns for the four lightest sparticles within one of the leading candidate theories - the SUGRA model. Specifically we analyze the hierarchies for the four lightest sparticles for the mSUGRA as well as for a general class of supergravity unified models including nonuniversalities in the soft breaking sector. It is shown that out of nearly 10^4 possibilities of sparticle mass hierarchies, only a small number survives the rigorous constraints of radiative electroweak symmetry breaking, relic density and other experimental constraints. The signature space of these mass patterns at the LHC is investigated using a large set of final states including multi-leptonic states, hadronically decaying τs, tagged b jets and other hadronic jets. In all, we analyze more than 40 such lepton plus jet and missing energy signatures along with several kinematical signatures such as missing transverse momentum, effective mass, and invariant mass distributions of final state observables. It is shown that a composite analysis can produce significant discrimination among sparticle mass patterns allowing for a possible identification of the source of soft breaking. While the analysis given is for supergravity models, the techniques used in the analysis are applicable to wide class of models including string and brane models.

Acknowledgements

I am deeply indebted to my advisor, Professor Pran Nath, for bringing me to the field of theoretical physics, and also for the enormous amount of time and efforts that he has taken to help me progress in my understanding of physics. My thesis would not have been possible without his constant guidance. His commitment to research and dedication to physics, and even his unique style of language and his sense of humor have all greatly influenced me. Being his student is a great fortune of my life.

I thank the other members of my committee, Professor George Alverson and Professor Tomasz Taylor for their help and patience during my Ph.D. study. I am also thankful to other members of the high energy group for many fruitful interactions throughout the years, especially Professor Brent Nelson and Professor Darien Wood.

I wish to thank Daniel Feldman, my collaborator, with whom the research contained in this thesis was completed and whose extraordinary energy and enthusiasm for physics has set a great example for me. I also thank him for his constant encouragement and help over the years.

I thank the Physics department for giving me this wonderful opportunity to study here, and for their financial support during the process of my graduate study. I would also like to thank the Office of the Provost and Dr. Luis M. Falcon for awarding me the Dissertation Writing Fellowship during my thesis writing.

I am very grateful to my fellow graduate students: Ismet Altunkaynak, Tanmoy Das,

Gabriel Facini, Peng He, Yongjian Huang, Jing Lou, Eugen Panaitescu, Thayaparan Paramanathan, Romain Scheck, Fei Wang, Zhen Wu, Weiqiao Zeng. With their friendship, I have spent a good time at Northeastern University.

Last and most, I thank my parents who have always been there for me. None of these would be made possible without the everlasting love and support of my parents who have devoted their lives to making me an educated person.

Contents

Chapter 1

Introduction

While the Standard Model of particle interactions is highly successful, important gaps remain in extending the model to a more complete unification, including the electroweak and the strong, and eventually the gravitational interactions. Over the past decades, supersymmetry (SUSY) has turned out to be one of the leading candidates for physics beyond the Standard Model. In this thesis, we investigate the signatures at the CERN Large Hadron Collider (LHC) for some of the supersymmetric theories. This analysis can be thought as a map from the parameter space of the underlying theories onto the signature space of the LHC, as indicated in Fig. (1.1). The parameter space is spanned by the input parameters of the theoretical models, and the number of the independent input parameter can be as many as ~ 110 in the Minimal Supersymmetric Standard Model (MSSM). It is not realistic to investigate models with such a large parameter space for their LHC signatures. However, it is possible to do so in some well motivated models where the dimensionality of the parameter space reduces significantly. Specifically we will focus on models where the dimension M of the parameter space is small, as often $M = 4$.

The strategy of this analysis is as follows. We start with a point in the M-

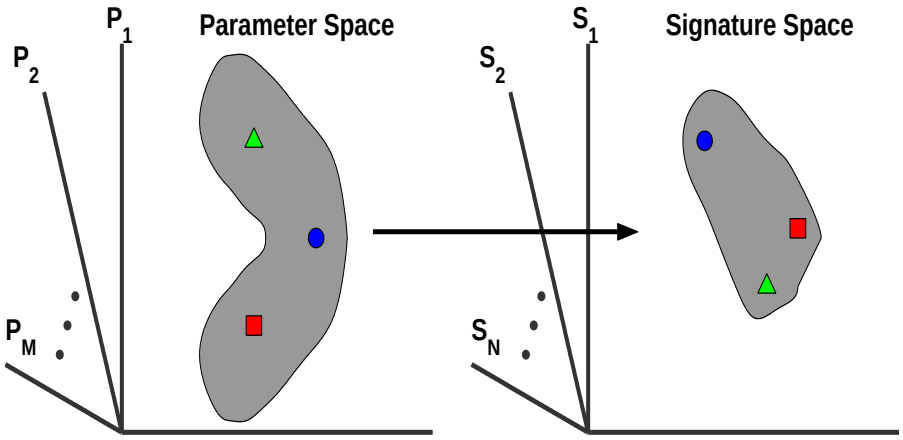

Figure 1.1: The map between the parameter space and the signature space.

dimensional parameter space, investigate the theoretical predictions of this model point, simulate its behavior within the Large Hadron Collider, and finally extract many possible LHC signatures which is represented by a point in the N-dimensional signature space as shown in Fig. (1.1). The dimensionality of the signature space can be expanded by adding more LHC signatures. However, many of the signature channels are strongly correlated so the independent set of signatures is typically much smaller than the number of signatures investigated.

The analysis in this thesis focuses on supergravity models, including the minimal supergravity grand unification models (mSUGRA) and SUGRA models with nonuniversalities (NUSUGRA). The mSUGRA model depends on four soft breaking parameters, and the SUGRA with nonuniversalities that we investigate here contain two more which characterize the nonuniversalities in different sectors. We perform an exhaustive scan with Monte Carlo simulations in the mSUGRA soft parameter space (4-D parameter space) and in NUSUGRA parameter space (6-D parameter space). The model points that pass the various cosmological and collider constraints are classified by their mass hierarchical patterns. These hierarchical patterns are defined by the four lightest sparticles. We will see that the hierarchical mass patterns to a great

degree influence the LHC signatures. Most of the analysis given here will attempt to correlate the hierarchical mass patterns with specific signatures at the LHC in the mSUGRA model. Extension of the analysis to NUSUGRA will also be discussed.

The thesis is organized as following. In chapter (2) we give a brief introduction to the Standard Model (SM), and in chapter (3) we discuss Supersymmetry (SUSY), and the Minimal Supersymmetric Standard Model (MSSM). In chapter (4), we give an introduction to supergravity unified models. We list the various experimental constraints that are imposed on the supergravity models in chapter (5).

An analysis of hierarchical mass patterns within the mSUGRA and NUSUGRA models is given in chapter (6). Here the correlations between the sparticle patterns and the nature of the soft breaking are also analyzed. In chapter (7), we give a detailed description of our simulations of the CERN Large Hadron Collider which includes the various steps of our simulation, the detector cuts, and the various signatures we investigate. In chapter (8), we analyze the signatures arising from the sparticle patterns, and also use the signatures to discriminate the patterns. Several important kinematical signatures are analyzed in chapter (9), including the missing transverse momenta, effective mass, and the dileptonic invariant mass distributions. In order to utilize as many signatures as possible, a global analysis using the so called fuzzy vector technique is given in chapter (10). An analysis regarding the signature degeneracies from different models and the ability of resolving the parameter space using the LHC data is carried out in chapter (11).

In addition to the signature analysis for the LHC, we also investigate other experimental signatures within the context of the sparticle pattern discrimination. These include the analysis of Higgs production at Tevatron in chapter (12), the $B_s \to \mu^+\mu^-$ constraints in chapter (13), and the direct detection of dark matter in chapter (14).

Chapter 2

The Standard Model

The Standard Model (SM) [1, 2] of particle physics is a theory that describes three of the four known interactions, which are the electrodynamics, the weak interactions and the strong interactions. The SM is based on the gauge group $SU(3)_C \times SU(2)_L \times U(1)_Y$ where C stands for color, L stands for left chiral, and Y stands for hypercharge. There are three generations of quarks and leptons in the SM which are represented by left-handed doublets and right handed singlets in the $SU(2)_L$ gauge group,

$$q_i = \begin{pmatrix} u_L \\ d_L \end{pmatrix}_i ; \qquad \ell_i = \begin{pmatrix} \nu_L \\ e_L \end{pmatrix}_i ; \qquad u_{Ri}; \qquad d_{Ri}; \qquad e_{Ri} \tag{2.1}$$

where $\Psi_{L,R} = P_{L,R}\Psi$, $P_L = (1 - \gamma_5)/2$, $P_R = (1 + \gamma_5)/2$, and $i = 1, 2, 3$ is the generation index. In order to give mass to quarks and leptons, as well as to vector bosons, an additional scalar $SU(2)_L$ doublet is introduced in the theory

$$\phi = \begin{pmatrix} H^{(+)} \\ H^{(0)} \end{pmatrix}. \tag{2.2}$$

The three fundamental interactions (the electroweak and the strong interactions) are mediated by eight $SU(3)$ color gluons, G^a_μ; three $SU(2)_L$ gauge bosons, A^i_μ; and one $U(1)$ hypercharge gauge field, B_μ. All the above gauge bosons are realized in the adjoint representations of their corresponding gauge groups, and the strength of the interactions are described by their coupling constants g_3, g_2 and g'.

The dynamics of the Standard Model consists of the following three parts:

1. Gauge interactions,

2. Yukawa interactions,

3. Higgs potential.

The gauge interactions arise via the gauge covariant derivative

$$D_\mu = \partial_\mu - i\left[g_3 \sum_{a=1}^{8} G^a_\mu T^a_C + g_2 \sum_{i=1}^{3} A^i_\mu T^i_L + g' B_\mu \frac{Y}{2}\right] \tag{2.3}$$

where T^a_C=($\lambda^a/2$; 0) for (quarks; leptons, Higgs), where the λ^a are the eight Gell-Mann matrices; T^i_L=($\sigma^i/2$; 0) for $SU(2)_L$ (doublets; singlets), where σ^i are the three Pauli matrices; and Y is the hypercharge defined by $Q = T^3_L + Y/2$.

Since the explicit fermion mass terms violate the gauge symmetries, adding mass terms in the SM is done through the Yukawa interactions and the mechanism of spontaneous symmetry breaking. Thus we consider the Higgs potential given by

$$V(\phi) = -\mu^2 \phi^\dagger \phi + \lambda(\phi^\dagger \phi)^2 \tag{2.4}$$

where μ^2 and λ are positive. The tachyonic mass term for the Higgs field gives rise to a spontaneous symmetry breaking which results in a non-vanishing vacuum expectation

value (VEV) of the Higgs field

$$\langle\phi\rangle_0 = \begin{pmatrix} 0 \\ v/\sqrt{2} \end{pmatrix} \tag{2.5}$$

where $v = \mu/\sqrt{\lambda}$. The neutral Higgs gets redefined with respect to this VEV, $H^0 = (v+h)/\sqrt{2}$ and the new Higgs boson possesses a positive tree level (mass)^2 of $M_h^2 = 2\mu^2 > 0$.

The Yukawa interactions which preserve the gauge symmetries are given by

$$V_Y = \lambda_{ij}^{(e)} \bar{\ell}_i \phi e_{Rj} + \lambda_{ij}^{(u)} \bar{q}_i \bar{\phi} u_{Rj} + \lambda_{ij}^{(d)} \bar{q}_i \phi d_{Rj} + h.c. \tag{2.6}$$

where $\bar{\phi} = i\sigma^2\phi^*$ is the complex conjugate of the Higgs doublet given in Eq. (2.2), and $\lambda_{ij}^{(e,u,d)}$ are the Yukawa coupling constants where $i, j = 1, 2, 3$ are the generation indices. The Yukawa interactions are responsible for giving rise to the fermion masses. The flavor basis of the fermion species are not necessary the same as the mass eigen states of the particles, and the unitary transformations between the flavor eigen states and the mass eigen states is accomplished via the Cabibbo-Kobayashi-Maskawa (CKM) matrix.

The spontaneous symmetry breaking also rotates the four $SU(2)_L \times U(1)_Y$ gauge bosons to their mass eigen states by means of the gauge interaction term of Higgs fields, $\{A^1, A^2\} \rightarrow \{W^1, W^2\}$ and $\{A^3, B\} \rightarrow \{A, Z\}$ where the photon field A remains massless. Introducing the weak mixing angle, θ_W defined by $\tan\theta_W = g'/g$, we can express the photon and Z boson fields as follows

$$A = \cos\theta_W B + \sin\theta_W A^3, \tag{2.7}$$

$$Z = -\sin\theta_W B + \cos\theta_W A^3. \tag{2.8}$$

The $W^{\pm}$ and Z boson masses at tree level are given by

$$M_W = \frac{g_2 v}{2} = \frac{g_2}{2\sqrt{2\lambda}} M_h, \quad M_Z = \frac{M_W}{\cos\theta_W}, \tag{2.9}$$

showing that the Higgs mass sets the electroweak mass scale.

Standard Model is a highly successful model. It predicted the existence of the W and Z bosons before these particles were observed. Since then, the SM has passed a variety of experimental tests with great accuracy. However, from the theoretical side, many aspects of the Standard Model are not satisfactory. There is no real unification among the electroweak and the strong interactions as the SM gauge group is a product of three different gauge groups.

However, the most serious problem within the Standard Model seems to be the "gauge hierarchy" problem, or "naturalness" problem which concerns the renormalization of the Higgs mass. Within the SM, the one loop corrections to M_h are quadratic in the momentum cutoff. If the cutoff momentum were to placed at the GUT scale $M_G \sim 10^{16}$ GeV, the tree level Higgs mass is forced to the same scale, in order to reproduce the electroweak scale. This then results in the "fine tuning" problem because of the huge difference between the GUT scale and the electroweak scale. Another shortcoming of the Standard Model is that gravity is not explained in its framework.

Chapter 3

Supersymmetry & the Minimal Supersymmetric Standard Model

Supersymmetry (SUSY) [3] is a symmetry between bosons and fermions, i.e. it requires that the number of bose and fermi helicity states in a multiplet be equal. A supersymmetry transformation turns a bosonic state into a fermionic state, and vice versa. The generator Q and its hermitian conjugate $Q^\dagger$ of a supersymmetry transformation obey the so called "Graded Lie Algebra" which includes the following commutation and anti-commutation relations

$$\{Q_\alpha, Q^\dagger_{\dot\alpha}\} = 2\sigma^\mu_{\alpha\dot\alpha} P_\mu, \tag{3.1}$$

$$\{Q_\alpha, Q_\beta\} = \{Q^\dagger_{\dot\alpha}, Q^\dagger_{\dot\beta}\} = 0, \tag{3.2}$$

$$[Q_\alpha, P_\mu] = [Q^\dagger_{\dot\alpha}, P_\mu] = 0, \tag{3.3}$$

$$[P_\mu, P_\nu] = 0, \tag{3.4}$$

where $\sigma^\mu = (-1, -\vec{\sigma})$ with σ^i being the Pauli matrices, and the undotted (dotted) indices, $\alpha = 1, 2$ ($\dot\alpha = 1, 2$) are introduced when a four-component Dirac spinor is

decomposed into two two-component Weyl spinors.

The simplest SUSY multiplets are the massless chiral multiplet and the vector multiplet. The left chiral multiplet consists of one left handed Weyl spinor (spin 1/2) and its superpartner, one complex scalar field ϕ (spin 0, left-handed). The Weyl spinors can be used to represent fermionic matter fields such as quarks and leptons and the scalar fields are the superpartners, i.e. "squarks" and "sleptons". The vector multiplet in the Wess-Zumino gauge consists of one vector field (spin 1) and one Majorana spinor (spin 1/2). The vector fields represent the gauge bosons, and the additional spinors are the superpartners of the gauge bosons called "gauginos".

quark	$q_i = \begin{pmatrix} u_L \\ d_L \end{pmatrix}_i$ u_{Ri} d_{Ri}	squark	$\tilde{q}_i = \begin{pmatrix} \tilde{u}_L \\ \tilde{d}_L \end{pmatrix}_i$ $\tilde{u}_{Ri}$ $\tilde{d}_{Ri}$
lepton	$\ell_i = \begin{pmatrix} \nu_L \\ e_L \end{pmatrix}_i$ e_{Ri}	slepton	$\tilde{\ell}_i = \begin{pmatrix} \tilde{\nu}_L \\ \tilde{e}_L \end{pmatrix}_i$ $\tilde{e}_{Ri}$
Higgsino	$\tilde{H}_1 = \begin{pmatrix} \tilde{H}_1^0 \\ \tilde{H}_1^- \end{pmatrix}$ $\tilde{H}_2 = \begin{pmatrix} \tilde{H}_2^+ \\ \tilde{H}_2^0 \end{pmatrix}$	Higgs	$H_1 = \begin{pmatrix} H_1^0 \\ H_1^- \end{pmatrix}$ $H_2 = \begin{pmatrix} H_2^+ \\ H_2^0 \end{pmatrix}$

Table 3.1: Chiral supermultiplets in the Minimal Supersymmetric Standard Model.

gluon	$G_\mu^a, (a = 1, ..., 8)$	gluino	$\tilde{G}^a, (a = 1, ..., 8)$
$SU(2)$ gauge boson	$A_\mu^i, (i = 1, 2, 3)$	$SU(2)$ gaugino	$\tilde{A}^i, (i = 1, 2, 3)$
$U(1)$ gauge boson	B_μ^Y	$U(1)$ gaugino	$\tilde{B}^Y$

Table 3.2: Vector supermultiplets in the Minimal Supersymmetric Standard Model.

The Minimal Supersymmetric Standard Model (MSSM) is the simplest supersymmetric extension of the Standard Model. One promotes each of the Standard Model particles to either a chiral or a vector multiplet, which makes the particle content

roughly twice as big as in SM as shown in Table (3.1, 3.2). In the Higgs sector one has two Higgs doublets, one of which (H_2) gives mass to the up quarks and the other (H_1) gives mass to the down quarks and the charged leptons.

In total there are 32 supersymmetric particles. These include 4 Higgs boson states, of which three (h, H, A) are neutral, the first two being CP even and the third CP odd, and one charged Higgs $H^{\pm}$. In the gaugino-Higgsino sector there are two charged mass eigenstates (charginos) $\tilde{\chi}^{\pm}_{i=1,2}$, four charge neutral states (neutralinos) $\tilde{\chi}^{0}_{i=1,2,3,4}$, and the gluino $\tilde{g}$. In the sfermion sector, before diagonalization, there are 9 scalar leptons (sleptons) which are superpartners of the leptons with left and right chirality and are denoted as: $\{\tilde{e}_{L,R}, \tilde{\mu}_{L,R}, \tilde{\tau}_{L,R}, \tilde{\nu}_{e_L}, \tilde{\nu}_{\mu_L}, \tilde{\nu}_{\tau_L}\}$. Finally there are 12 squarks which are the superpartners of the quarks and are represented by: $\{\tilde{u}_{L,R}, \tilde{c}_{L,R}, \tilde{t}_{L,R}, \tilde{d}_{L,R}, \tilde{s}_{L,R}, \tilde{b}_{L,R}\}$. Mass diagonal slepton and squark states will in general be mixtures of L, R states.

In MSSM the superpotential with R-parity conservation is given by

$$W = \hat{U}^C Y_u \hat{Q} \hat{H}_u + \hat{D}^C Y_d \hat{Q} \hat{H}_d + \hat{E}^C Y_e \hat{L} \hat{H}_d + \mu \hat{H}_u \hat{H}_d \tag{3.5}$$

where $Y_{u,d,e}$ are matrices in family space. One can add a large number of soft terms to the Lagrangian. Examples of R-parity conserving terms are

$$\mathcal{L}_{soft} = \mathcal{L}^{(2)}_{soft} + \mathcal{L}^{(3)}_{soft}. \tag{3.6}$$

The soft SUSY-breaking Lagrangian contains scalar couplings

$$\mathcal{L}^{(3)}_{soft} = \tilde{u}^C h_u \tilde{Q} H_u + \tilde{d}^C h_d \tilde{Q} H_d + \tilde{e}^C h_e \tilde{L} H_d + B H_u H_d + h.c. \tag{3.7}$$

where $h_{u,d,e}$ are 3×3 matrices. There are also scalar masses

$$\mathcal{L}^{(2)}_{soft} = m^2_{H_u} H^\dagger_u H_u + m^2_{H_d} H^\dagger_d H_d + \tilde{Q}^\dagger M^2_{\tilde{Q}} \tilde{Q} + \tilde{L}^\dagger M^2_{\tilde{L}} \tilde{L} \\ + \tilde{u}^{C\dagger} m^2_{\tilde{u}}\ \tilde{u}^C + \tilde{d}^{C\dagger} m^2_{\tilde{d}}\ \tilde{d}^C + \tilde{e}^{C\dagger} m^2_{\tilde{e}}\ \tilde{e}^C \tag{3.8}$$

where $M^2_{\tilde{Q}}$, $M^2_{\tilde{L}}$, $m^2_{\tilde{u}}$, $m^2_{\tilde{d}}$, and $m^2_{\tilde{e}}$ are 3×3 matrices in family space. More generally, as already noted, there can be as many as ~ 110 parameters in the soft terms. However, as we will see, the sets of parameters decrease significantly in Supergravity Unified Models.

Chapter 4

Supergravity Unified Models

Supersymmetry provides a solution to the gauge hierarchy problem, which makes it an attractive candidate for the new physics beyond the Standard Model. The main hurdle in the development of realistic supersymmetric models in the early days was the difficulty of breaking supersymmetry in a phenomenologically viable manner. In the framework of supergravity, this problem is solved by the inclusion of the gravity into the analysis, which promotes supersymmetry from a global symmetry to a local symmetry [4, 5, 6].

To construct viable supergravity models one must couple $N = 1$ supergravity with vector gauge fields and with matter. This construction is often referred to as "applied supergravity" [6, 7, 8] and herein one couples $N = 1$ supergravity with $N = 1$ Yang-Mills fields in the adjoint representation of the gauge group G (where G could be $SU(3)_C \times SU(2)_L \times U(1)_Y$, or $SU(5), SO(10), E(6)$ etc), and with $N = 1$ matter which contains quarks and leptons and Higgs fields which belong to anomaly free combinations of representations of the gauge group. The most general effective Lagrangian thus constructed depends on three functions which are the superpotential $W(\phi_i)$, the Kahler potential $K(\phi_i, \phi_i^\dagger)$, and the gauge kinetic function $f_{\alpha\beta}(\phi_i, \phi_i^\dagger)$

where α, β are adjoint representation gauge indices, ϕ_i are the spin zero components of the left handed chiral multiplet consisting of (ϕ_i, χ_i). We note that W, K and $f_{\alpha\beta}$ are hermitian. In fact W and K enter in the effective theory only in the following fixed combination

$$\mathcal{G} = \kappa^2 K + \ell n[\kappa^6 W W^\dagger] \tag{4.1}$$

where

$$\kappa = 1/M_{\rm Pl} \tag{4.2}$$

and $M_{\rm Pl}$ is the Planck mass defined in terms of the Newton's constant G_N by

$$M_{\rm Pl} = (8\pi G_N)^{-1/2} = 2.4 \times 10^{18}{\rm GeV}. \tag{4.3}$$

The above implies that the supergravity Lagrangian effectively depends only on two functions which are $f_{\alpha\beta}$ and $\mathcal{G}$. From the above one can easily check that the effective theory is invariant under the Kahler transformation as given below

$$K \to K - f(\phi_i) - f^\dagger(\phi_i),\ W \to e^{\kappa^2 f} W. \tag{4.4}$$

It is useful to introduce the so called Kahler metric as follows

$$K^i_j = K^{,i}_{,j} \equiv \frac{\partial^2 K}{\partial \phi_i \phi^\dagger_j}\ = \kappa^{-2} \mathcal{G}^{,i}_{,j}. \tag{4.5}$$

The case $K = \sum_i \phi_i \phi^\dagger_i$ gives $K^i_j = \delta^i_j$ which is referred to as the flat Kahler metric.

One of the most important results that emerges from the applied supergravity analysis is that the effective potential of $N = 1$ theory takes the form [6, 8]

$$V = \kappa^{-4} e^{-\mathcal{G}}\ \left[(\mathcal{G}^{-1})^i_j \mathcal{G}_{,i} \mathcal{G}^{,j} - 3\right] + \frac{g^2}{2}\ \left[Re(f^{-1})_{\alpha\beta}\right]\ D_\alpha D_\beta. \tag{4.6}$$

In the above g is the gauge coupling constant, and $(f^{-1})_{\alpha\beta}$ and $(\mathcal{G}^{-1})^i_j$ are the matrix inverses of $f_{\alpha\beta}$ and $\mathcal{G}^{,i}_{,j}$ while D_α is given by

$$D_\alpha = \kappa^{-2}\mathcal{G}^{,i}(T^\alpha)_{ij}z_j \tag{4.7}$$

where T^α is the group generator. An alternative form which is often useful is to write the scalar potential explicitly in term of $\tilde{W}$ and K, and one then has

$$V = e^{\kappa K}\left[(K^{-1})^i_j\left(\frac{\partial\tilde{W}}{\partial z_i} + \kappa^2 K_{,i}\tilde{W}\right)\left(\frac{\partial\tilde{W}}{\partial z_j} + \kappa^2 K_{,j}\tilde{W}\right)^\dagger - 3\kappa^2|\tilde{W}|^2\right] + V_D \tag{4.8}$$

where V_D is as given as before. In the applied supergravity construction the kinetic energy of scalar fields is given by

$$-K^{,i}_{,j}(D^\mu\phi_i)\ (D_\mu\phi_j)^\dagger \tag{4.9}$$

where D_μ is the gauge covariant derivative.

Before proceeding further we comment on the μ term that arises in the Higgs bilinear term in the form $\mu H_1 H_2$ in the superpotential. For phenomenological reasons μ must be of electroweak size, and thus one might speculate on the origin of this term in the superpotential. In fact it is not difficult to see how such a term can arise. The simplest way to envision the generation of such a term is via the Kahler potential. Thus one can write the Kahler potential for the MSSM case so that

$$K = K_0(\phi_i\phi_i^\dagger) + c_0 H_1 H_2 \tag{4.10}$$

where ϕ_i are the MSSM scalar and c_0 is dimensionless. Note that $\mu_0 H_1 H_2$ is the most general bilinear term which one write without introducing dimensioned parameters

in the Kahler potential. Specifically operators of dimension greater than 2 will be suppressed by $1/M_{Pl}$ and thus their contributions will be small. Next one can make a Kahler transformation and move the $c_0 H_1 H_2$ term from the Kahler potential to the superpotential [9]. Indeed a term of this type arises naturally in string constructions [10].

After the transformation the superpotential has the form

$$W e^{\kappa^2 f} = W + c_0 \kappa^2 W H_1 H_2 + \cdot\cdot \tag{4.11}$$

As is discussed below spontaneous breaking of supersymmetry by gravity mediation gives a non-vanishing VEV for W and we define

$$\mu_0 = c_0 \kappa^2 \langle W \rangle \tag{4.12}$$

where as will be seen below the quantity $\kappa^2 \langle W \rangle$ is of electroweak size.

We now turn to the issue of breaking of supersymmetry. One of the reasons that globally supersymmetric models do not have phenomenologically acceptable breaking of supersymmetry is that here one has a positive definite potential which after spontaneous breaking of supersymmetry leads to a large non-vanishing vacuum energy. This problem is corrected in supergravity models. Here as seen in Eq. (4.8) one finds that the potential contains a term with a negative sign and thus after spontaneous breaking the vacuum energy can be fine tuned to zero.

The central assumption of breaking of supersymmetry in supergravity models is that supersymmetry is broken in a hidden sector and the breaking is transmitted by the gravitational interactions to the visible sector. A specific illustration of this comes

about as follows: One writes the superpotential in the form [6, 11]

$$W = W_{\rm vis} + W_{\rm hid} \tag{4.13}$$

where $W_{\rm vis}$ contains fields of the visible sector which are the MSSM fields including quarks and leptons and Higgs fields, and $W_{\rm hid}$ contains fields in the hidden sector where supersymmetry breaks. The breaking gives a non-vanishing VEV so that $\langle W\rangle = \langle W_{\rm hid}\rangle$. The size of $\langle W_{\rm hid}\rangle$ is estimated to be $m^2 M_{\rm Pl}$ where m is an intermediate scale so that $m \sim 10^{11}$ GeV. The breaking is transmitted to the visible sector by gravitational interactions producing soft breaking terms. The gravitino develops a mass which is $M_{3/2} = \kappa^2 e^{\mathcal{K}/2}|W|$. Similarly the scale of soft breaking that enters the scalar sector is given by

$$m_0^2 \sim (\kappa^2\langle W_{\rm hid}\rangle)^2. \tag{4.14}$$

Thus with $m \sim 10^{11}$ one finds $m_0 \sim 10^3$ GeV, i.e., of electroweak size. Other soft terms can be generated in a similar way. A remarkable aspect of the analysis is that in supergravity grand unified models the soft breaking is independent of the grand unified unification scale M_G which cancels out in the low energy theory [6, 12, 13]

The gauge kinetic energy terms that generate masses for the gauginos are exhibited below

$$\begin{aligned}\mathcal{L}_{\rm gauge} = \quad & -\frac{1}{4}\Re\big[f_{\alpha\beta}F^{\alpha}_{\mu\nu}F^{\beta\mu\nu}\big] + \frac{1}{4}i\Im\Big[f_{\alpha\beta}F^{\alpha}_{\mu\nu}\tilde{F}^{\beta\mu\nu}\Big] + \frac{1}{2}\Re\Big[f_{\alpha\beta}\left(-\frac{1}{2}\bar{\lambda}^{\alpha}\not{D}\lambda^{\beta}\right)\Big] \\ & -\frac{1}{8}i\Im\big[f_{\alpha\beta}e^{-1}D_{\mu}(e\bar{\lambda}^{\alpha}\gamma^{\mu}\gamma_5\lambda^{\beta})\big] + \frac{1}{4}\bar{e}^{G/2}G^{a}(G^{-1})^{b}_{a}(\partial f^{*}_{\alpha\beta}/\partial z^{*b}\lambda^{\alpha}\lambda^{\beta}) + \text{h.c.}\end{aligned}$$

In general the gauge kinetic energy function $f_{\alpha\beta}$ has a non-trivial field dependence involving fields which transform as a singlet or a non-singlet irreducible representation of the underlying gauge group. After the spontaneous breaking of supersymmetry the

above lead to gaugino masses. If one assumes that the fields transform as singlets of the underlying gauge groups, then the gaugino masses at the GUT scale will be universal and generate a term of the form $m_{1/2}\bar{\lambda}_\alpha\lambda_\alpha$. Splitting of the gauge masses can be obtained by the assumption that $f_{\alpha\beta}$ have fields which transform as non-singlet irreducible representation of the underlying gauge group.

The phenomenology of supergravity (SUGRA) models has been discussed since the inception of these models (for reviews see [14, 15, 16, 17] and there exists now a considerable amount of literature regarding the implications of SUGRA (for early works see [18], for more recent works see [19, 20, 21] and [22, 23, 24, 25, 26], for works with nonuniversalities see [27], and for works with hierarchical breaking and with $U(1)$ gauge extensions see [28, 29, 30]). While many analyses of the mSUGRA parameter space have been limited to the case of vanishing trilinear couplings, several recent works [31, 32, 33, 34, 20, 21, 35, 36, 37] have appeared relaxing this assumption, and new portions of the parameter space have been found consistent with all known experimental constraints on the model.

As mentioned already in the previous chapter, there are 32 different supersymmetric particles, or sparticles. If all the 32 sparticle masses are treated as essentially all independent, aside from sum rules (for a pedagogical analysis on sum rules in the context of unification and RG analysis see [38]) on the Higgs, sfermions, chargino and neutralino masses, then without imposition of any phenomenological constraints, the number of hierarchical patterns for the sparticles could be as many as $O(10^{25})$ or larger. This represents a mini landscape in a loose way reminiscent of the string landscape (which, however, is much larger with as many as $O(10^{1000})$ possibilities) [39]. (Here we refer to the landscape of mass hierarchies and not to the landscape of vacua as is the case when one talks of a string landscape. For the string case the landscape consists of a countably discrete set, while for the case considered here, since

the parameters can vary continuously, the landscape of vacua is indeed much larger. However, our focus will be the landscape of mass hierarchies.) Now, the number of possibilities can be reduced by very significant amounts in supergravity models with the imposition of the constraints of radiative electroweak symmetry breaking (REWSB) which we discuss below.

4.1 Radiative Electroweak Symmetry Breaking

In the minimal supergravity unification (mSUGRA) the potential at the GUT scale which gives rise to the soft breaking of supersymmetry is given by

$$V = \sum_a |\frac{\partial W}{\partial \phi_a}|^2 + m_0^2 \sum_i \phi_i^\dagger \phi_i + A_0 W^{(3)} + B_0 W^{(2)} + m_{1/2} \sum_{\alpha=3,2,1} \bar{\lambda}_\alpha \lambda_\alpha \qquad (4.15)$$

where ϕ_i are the scalar fields, $\lambda_\alpha (\alpha = 3, 2, 1)$ are the gauginos corresponding to $SU(3)_C$, $SU(2)_L$ and $U(1)_Y$ gauge groups, A_0 is the coefficient of the trilinear coupling, and B_0 is the coefficient of the bilinear coupling. For MSSM, $W^{(2)}$ takes the form

$$W^{(2)} = \mu_0 \epsilon_{ij} H_1^i H_2^j \qquad (4.16)$$

where $i, j = 1, 2$, and $W^{(3)}$ takes the form

$$W^{(3)} = \lambda_{ij}^{(u)} q_i H_2 u_j^C + \lambda_{ij}^{(d)} q_i H_1 d_j^C + \lambda_{ij}^{(e)} \ell_i H_1 e_j^C \qquad (4.17)$$

where $\lambda_{ij}^{(u,d,e)}$ are the Yukawa couplings (analogous to those in Eq. (2.6)) and H_1 and H_2 are the two Higgs doublets.

The soft breaking for the minimal supergravity model is thus given by the param-

eters

$$m_0, \quad m_{1/2}, \quad A_0, \quad B_0. \tag{4.18}$$

While the mSUGRA model is initialized at the GUT scale, the experiments are carried out at the electroweak scale. One needs the Renormalization Group Equations (RGE) to connect these two domains [40]. For discussion of the electroweak symmetry breaking, one needs the effective Higgs potential which is $V = V_0 + \Delta V_1$ where V_0 is the tree part and ΔV_1 is the one loop corrections [41, 42]

$$V_0 = m_1^2|H_1|^2 + m_2^2|H_2|^2 - m_3^2(H_1H_2 + h.c.) + \frac{1}{8}(g_2^2 + g_Y^2)(|H_1|^2 - |H_2|^2)^2, \tag{4.19}$$

and

$$\Delta V_1 = \frac{1}{64\pi^2}\sum_a (-1)^{2s_a} n_a M_a^4 \ln\left[\frac{M_a^2}{e^{3/2}Q^2}\right]. \tag{4.20}$$

Here, $m_i(t)$, $g_2(t)$, $g_Y(t)$ are all "running" parameters at scale Q where $t = \ln(M_G^2/Q^2)$. Thus [16]

$$m_i^2(t) = m_{H_i}^2(t) + \mu^2(t), \quad i = 1, 2; \tag{4.21}$$

$$m_3^2(t) = -B(t)\mu(t); \tag{4.22}$$

with the boundary conditions at the GUT scale $Q = M_G(t = 0)$:

$$m_i^2(0) = m_0^2 + \mu_0^2, \quad i = 1, 2; \tag{4.23}$$

$$m_3^2(0) = -B_0\mu_0. \tag{4.24}$$

The coupling constants are unified at the GUT scale too

$$\alpha_2(0) = (5/3)\alpha_Y(0) = \alpha_G. \tag{4.25}$$

In Eq. (4.1), $M_a \equiv M_a(v_1, v_2)$ is the tree level mass of particle a as functions of the Higgs VEVs, $v_i = \langle H_i \rangle$, and s_a and n_a are the spin and number of helicity states of particle a.

At the GUT scale, all scalar particles are of positive mass^2 values m_0^2. When one integrates down in the energy scale with RGEs, some mass^2 values can turn negative which will break down the $SU(2) \times U(1)$ symmetry as we have seen in the chapter (2). The $SU(2) \times U(1)$ symmetry breaking requires two conditions: (1) the determinant of the mass^2 matrix be negative so that there exists one negative eigenvalue; (2) the potential be bounded from below. We apply these two conditions to the tree level Higgs potential and get

$$\mathcal{D} = m_1^2 m_2^2 - m_3^4 < 0, \tag{4.26}$$

$$\mathcal{L} = m_1^2 + m_2^2 - 2|m_3^2| > 0. \tag{4.27}$$

The above two conditions cannot be satisfied simultaneously at the GUT scale since all scalar particles have the same mass. However, when one evolves down from the GUT scale to the electroweak scale, the heavy top quark contributions to $m_{H_2}^2$ naturally pushes it to turn negative so that electroweak symmetry breaking can be achieved. The fact that the top quark must be heavy was one of the predictions of the supergravity theories [43] (see [44] for a recent review of radiative breaking). Because the electroweak symmetry breaking is driven by the quantum loop corrections, this mechanism is therefore known as radiative electroweak symmetry breaking (REWSB).

Turning now to the minimization of the Higgs potential, one has the following relations

$$\mu_1^2 - m_3^2 \tan\beta + \frac{1}{2} M_Z^2 \cos(2\beta) = 0, \tag{4.28}$$

$$\mu_2^2 - m_3^2 \cot\beta - \frac{1}{2} M_Z^2 \cos(2\beta) = 0, \tag{4.29}$$

where $\tan\beta \equiv v_2/v_1$, $\mu_i^2 = m_i^2 + \Sigma_i (i = 1, 2)$ and Σ_i is the loop corrections arising from the loop Higgs potential ΔV_1. Taking μ_i^2 and m_3^2 as the input parameters, one can solve for $\tan\beta$ and M_Z

$$\sin(2\beta) = \frac{2m_3^2}{\mu_1^2 + \mu_2^2}; \tag{4.30}$$

$$\frac{1}{2}M_Z^2 = \frac{\mu_1^2 - \mu_2^2 \tan^2\beta}{\tan^2\beta - 1}. \tag{4.31}$$

One can also treat the $\tan\beta$ and M_Z as the input parameters, and eliminate two of the GUT scale parameters, say B_0 and μ_0, using Eqs. (4.30, 4.31). Since only μ^2 enters the Eqs. (4.30, 4.31), the sign of μ is undetermined. Thus one has that the low energy physics depends on the following parameters

$$m_0, \quad m_{1/2}, \quad A_0, \quad \tan\beta, \quad sign(\mu) \tag{4.32}$$

where m_0 is the universal scalar mass, $m_{1/2}$ is the universal gaugino mass, A_0 is the universal trilinear coupling, $\tan\beta$ is the ratio of the two Higgs VEVs in the MSSM, and μ is the Higgs mixing parameter that enters via the term $\mu H_1 H_2$ in the superpotential.

4.2 Hyperbolic Branch (HB) of Radiative Symmetry Breaking

The symmetry breaking condition Eq. (4.31) can be rewritten as [45, 46]

$$\Phi = \frac{1}{4} + \frac{\mu^2}{M_Z^2}, \tag{4.33}$$

where the new parameter

$$\Phi^{-1} \equiv 4\frac{\lambda^2 - \mu^2}{\lambda^2 + \mu^2} \tag{4.34}$$

is introduced for the purpose of the measure of naturalness. Using the radiative electroweak symmetry breaking constraint and ignoring the b-quark couplings, we may express the parameter Φ as

$$\Phi = -\frac{1}{4} + \left(\frac{m_0}{M_Z}\right)^2 C_1 + \left(\frac{A_0}{M_Z}\right)^2 C_2 + \left(\frac{m_{1/2}}{M_Z}\right)^2 C_3 + \left(\frac{m_{1/2}A_0}{M_Z^2}\right) C_4 + \frac{\Delta\mu^2_{loop}}{M_Z^2}, \tag{4.35}$$

where

$$\begin{aligned}
C_1 &= \frac{1}{\tan^2\beta - 1}\left(1 - \frac{3D_0 - 1}{2}\tan\beta\right), && (4.36)\\
C_2 &= \frac{\tan^2\beta}{\tan^2\beta - 1}k, && (4.37)\\
C_3 &= \frac{1}{\tan^2\beta - 1}\left(g - e\tan^2\beta\right), && (4.38)\\
C_4 &= -\frac{\tan^2\beta}{\tan^2\beta - 1}f, && (4.39)\\
\Delta\mu^2_{loop} &= \frac{\Sigma_1 - \Sigma_2\tan^2\beta}{\tan^2\beta - 1}. && (4.40)
\end{aligned}$$

Here $D_0 = 1 - (m_t/m_f)^2$ with $m_f \sim 200\sin\beta$ GeV, and e, f, g, k are defined in [47]. To investigate the limits of m_0 and $m_{1/2}$ consistent with the symmetry breaking for some given value of Φ, we rewrite the Eq. (4.2) as

$$C_1 m_0^2 + C_3 m_{1/2}'^2 + C_2' A_0^2 + \Delta\mu^2_{loop} = M_Z^2\left(\Phi_0 + \frac{1}{4}\right), \tag{4.41}$$

where

$$m_{1/2}' = m_{1/2} + \frac{A_0 C_4}{2C_3}, \quad C_2' = C_2 - \frac{C_4^2}{4C_3}. \tag{4.42}$$

For small to moderate values of $\tan\beta$, when the loop corrections are small and

C_1, C_2', and C_3 are all positive from the renormalization group analysis, Eq. (4.2) can be rewritten as

$$\frac{m_{1/2}^{'2}}{a^2} + \frac{m_0^2}{b^2} + \frac{A_0^2}{c^2} \simeq 1. \tag{4.43}$$

Here one finds that the radiative symmetry breaking demands that the allowed set of soft parameters lie on the surface of an Ellipsoid for a fixed value of μ. However, for the case with large values of $\tan\beta$, the loop corrections to μ become significant. In this case, the size of the loop corrections depends sharply on the scale Q_0 where the minimization of the effective potential is carried out. If we choose the scale at which the loop corrections are minimized, or even vanish, the loop corrections can be omitted for the analysis again except that the sign of C_1 can be flipped for some region of the parameter space. Typically the scale is not distant from the average of the smallest and largest sparticle masses. Under these conditions, the minimization condition takes the form

$$\frac{m_{1/2}^{'2}}{\alpha^2(Q_0)} - \frac{m_0^2}{\beta^2(Q_0)} \simeq \pm 1 \tag{4.44}$$

where

$$\alpha^2 = |\frac{(\Phi_0 + 1/4)M_Z^2 - C_2' A_0^2}{C_3}|, \tag{4.45}$$

$$\beta^2 = |\frac{(\Phi_0 + 1/4)M_Z^2 - C_2' A_0^2}{C_1}|. \tag{4.46}$$

The set of parameters which satisfy the above relation lie on the surface of a Hyperboloid, and thus this branch is known as the Hyperbolic Branch (HB). The interesting thing about the HB region is that m_0 and $m_{1/2}$ can become quite large with m_0 lying in the multi TeV region even with small fine tuning [45].

We note in passing that while the phenomena with soft breaking discussed above are within the framework of supergravity models many aspects of these results trans-

late to soft breaking within the framework of heterotic string models and for models based on intersecting D branes (see, e.g., [48, 49, 50, 51, 52]).

4.3 Sparticle Masses

Now let us list the mass matrices for the sparticles in the MSSM. Due to the effect of electroweak symmetry breaking, the higgsinos and the electroweak gauginos are mixed to form the mass eigenstates called neutralinos and charginos. For the neutralinos, the mass matrix takes the form

$$M_{\tilde{\chi}^0} = \begin{pmatrix} M_1 & 0 & -M_Z s_W c_\beta & M_Z s_W s_\beta \\ 0 & M_2 & M_Z c_W c_\beta & -M_Z c_W s_\beta \\ -M_Z s_W c_\beta & M_Z c_W c_\beta & 0 & -\mu \\ M_Z s_W s_\beta & -M_Z c_W s_\beta & -\mu & 0 \end{pmatrix} \tag{4.47}$$

where θ_W is the weak angle, $s_W = \sin\theta_W$, $c_W = \cos\theta_W$, $s_\beta = \sin\beta$, and $c_\beta = \cos\beta$. For the charginos, the mass matrix takes the form

$$M_{\tilde{\chi}^\pm} = \begin{pmatrix} M_2 & \sqrt{2} M_W s_\beta \\ \sqrt{2} M_W c_\beta & \mu \end{pmatrix} \tag{4.48}$$

The up squark (mass)^2 matrix at the electroweak scale is given by

$$M_{\tilde{u}}^2 = \begin{pmatrix} M_{\tilde{Q}}^2 + {m_u}^2 + M_Z^2(\frac{1}{2} - Q_u s_W^2)\cos 2\beta & m_u(A_u^* - \mu\cot\beta) \\ m_u(A_u - \mu^*\cot\beta) & m_{\tilde{u}}^2 + {m_u}^2 + M_Z^2 Q_u s_W^2 \cos 2\beta \end{pmatrix} \tag{4.49}$$

where $Q_u = \frac{2}{3}$. And the down squark (mass)^2 matrix at the electroweak scale is given

by

$$M_{\tilde{d}}^2 = \begin{pmatrix} M_{\tilde{Q}}^2 + {m_d}^2 - M_Z^2(\frac{1}{2} + Q_d s_W^2)\cos 2\beta & m_d(A_d^* - \mu \tan\beta) \\ m_d(A_d - \mu^* \tan\beta) & m_{\tilde{d}}^2 + {m_d}^2 + M_Z^2 Q_d s_W^2 \cos 2\beta \end{pmatrix} \quad (4.50)$$

where $Q_d = -\frac{1}{3}$. In deducing the above, the relations $h_{u,d,e} = Y_{u,d,e} A_{u,d,e}$ are used for the trilinear terms. Finally, the slepton (mass)^2 matrix is given by

$$M_{\tilde{l}}^2 = \begin{pmatrix} M_{\tilde{L}}^2 + m_e^2 - M_Z^2(\frac{1}{2} - s_W^2)\cos 2\beta & m_e(A_e^* - \mu \tan\beta) \\ m_e(A_e - \mu^* \tan\beta) & m_{\tilde{e}}^2 + m_e^2 - M_Z^2 s_W^2 \cos 2\beta \end{pmatrix} \quad (4.51)$$

4.4 Dark Matter in Supergravity

In most of the allowed parameter space of the mSUGRA model consistent with radiative breaking of the EW symmetry, the lightest neutralino is the LSP and hence a candidate for cold dark matter. We briefly discuss the computation of the relic density of neutralino $\Omega_\chi \equiv \rho_\chi/\rho_c$ where ρ is the mass density of relic neutralinos in the universe and ρ_c is the critical mass density needed to close the universe, i.e.

$$\rho_c = \frac{3H_0^2}{8\pi G_N}. \quad (4.52)$$

Here H_0 is the Hubble parameter at current time and G_N is the newtonian constant. Numerically, one has

$$\rho_c = 1.9 h_0^2 \times 10^{-29} \mathrm{gm/cm}^3 \quad (4.53)$$

where h_0 is now the Hubble parameter in unit of 100 km/secMpc. The current value of h_0 is $h_0 = 0.7 \pm 0.013$. In the analysis of $\Omega_\chi h_0^2$ we need to solve the Boltzman equation for n, the number density of neutralinos in the early universe, which is given

by [53]

$$\frac{dn}{dt} = -3Hn - \langle\sigma v\rangle(n^2 - n_0^2). \tag{4.54}$$

In the above, n_0 is the value of n at thermal equilibrium, $\langle\sigma v\rangle$ is the thermal average of the neutralino annihilation cross section $\sigma(\widetilde{\chi}_1^0\widetilde{\chi}_1^0 \to X)$ and v is the relative $\widetilde{\chi}_1^0$ velocity, and H is the Hubble parameter at time t. In the computation of the thermal average one can assume that the neutralinos are non-relativistic and thus one can approximate $\langle\sigma v\rangle$ by the relation

$$\langle\sigma v\rangle = \frac{\int_0^\infty dv v^2(\sigma v)e^{-v^2/4x}}{\int_0^\infty dv v^2 e^{-v^2/4x}}. \tag{4.55}$$

Here x is defined by $x = kT/m_\chi$ where T is the temperature and k is Boltzman constant. A solution to the Boltzman equation gives [16]

$$\Omega_\chi h_0^2 = 2.5 \times 10^{-11} \left(\frac{T_\chi}{T_\gamma}\right)^3 \left(\frac{T_\gamma}{2.75}\right)^3 \frac{N_f^{1/2}}{J(x_f)} \tag{4.56}$$

where T_γ is the current microwave background temperature, x_f is the "freeze out" temperature corresponding to the temperature where the annihilation rate becomes smaller than the expansion rate, so that $\widetilde{\chi}_1^0$ decouples from the background. x_f is typically small with a value $x_f \sim 0.04$. N_f is the number of degrees of freedom at freeze out and typically $N_f \simeq 289.5/8$ [54]. The factor $(T_\gamma/T_\chi)^3$ is estimated to be $(T_\gamma/T_\chi)^3 \simeq 18.5$ (for more recent evaluation, see [55]). Finally, $J(x_f)$ is the integral defined by

$$J(x_f) = \int_0^{x_f} dx\langle\sigma v\rangle x \quad (\mathrm{GeV}^{-2}). \tag{4.57}$$

Away from the poles one can carry out a power series expansion for σv so that $\sigma v = a + bv^2/6 + \cdots$. In this case the thermal average is straightforward. However, the above approximation is invalid near poles [56, 57, 58, 59] and the integration

becomes tricky since one has a double integration over a pole. However, it is possible to overcome this problem by an interchange in the order of integration as discussed in [58, 59].

A realistic computation of the relic density in supersymmetric models is however, more complicated as co-annihilations contribute to the relic density [56, 60, 61, 62]

For instance, one can have co-annihilations involving staus $\tilde{\tau}$ so that

$$\tilde{\tau}\chi \rightarrow \tau Z, \tau h, \tau\gamma \tag{4.58}$$

$$\tilde{\tau}\tilde{\tau}^* \rightarrow f_i\bar{f}_i, W^+W^-, ZZ, \gamma Z, \gamma\gamma \tag{4.59}$$

$$\tilde{\tau}\tilde{\tau} \rightarrow \tau\tau \tag{4.60}$$

$$\tilde{\tau}\tilde{\ell}_i(i \neq \tau) \rightarrow \tau\ell_i \tag{4.61}$$

For the case of co-annihilation, one must consider the total density $n = \sum_i n_i$ where i runs over all the sparticles that enter in the co-annihilations, where n now obeys the equation

$$\frac{dn}{dt} = -3Hn - \langle\sigma_{\rm eff} v_{\rm rel}\rangle(n^2 - n_{\rm eq}^2) \tag{4.62}$$

where

$$\sigma_{\rm eff} = \sum_{ij} \sigma_{ij}\gamma_i\gamma_j. \tag{4.63}$$

Here σ_{ij} is the cross section of annihilation of particles i and j, and $\gamma_i = n_{\rm eq}^i/n_{\rm eq}$ where $n_{\rm eq}^i$ refers to the number density of sparticle i at thermal equilibrium. The relic density for these processes requires numerical integration programs and we use micrOMEGAs [63] in our analysis. We note in passing that relic density is affected by Yukawa unification (see, e.g. [64] and the references therein) but we do not take such effects into account here.

4.5 CP violation

MSSM contains many sources of CP violation which arise from the soft breaking sector of the theory (for a review of CP violation in SUGRA, strings and branes see [65]). The number of phases in SUGRA models is reduced drastically. Specifically in mSUGRA one has just two CP phases which can be chosen to be the phase of the trilinear coupling A and the phase of μ. With non-universalities one can bring in new phases. A similar situation holds in string and D brane models. A stringent constraint on CP phases arises from the electric dipole moment (EDM) of the electron and of the neutron (see, e.g., [66]) which would naively imply that SUSY phases are all very small. However, this need not be the case [67] because of the cancellation mechanism [68]. With the cancellation mechanism, one finds that the phases can be large and at the same time one can satisfy the EDM constraints. Such phases can affect low energy phenomena such as the the gaugino and sfermion masses and Higgs masses [69]. CP phases can affect LHC signatures. However, in this study we do not take the effect of CP phases into account.

4.6 Proton stability

Another constraint on unified models of particle interactions arises from proton decay constraints (for a recent review see [70]). In grand unified models and also in string and brane models, one has several sources of proton decay. First of all, both in supersymmetric as well as in non-supersymmetric grand unified models one has baryon and lepton number violating dimension six operators due to the exchange of lepto-quarks. The most prominent decay mode from these is $p \to e^+\pi^0$ and the current limit on this decay is $\tau(p \to e^+\pi^0) > 1.6 \times 10^{33}$ yr. In supersymmetric theories the most dominant decay mode is $p \to \bar{\nu}K^+$ and the current limit on it is $\tau(p \to \bar{\nu}K^+) > 2.3 \times 10^{33}$ yr.

This latter limit, i.e., on the mode $\bar{\nu}K^+$, puts very stringent limits on grand unified models and on string models. At the same time these modes are subject to a much greater degree of model dependence because of the unknown nature of physics at high scales. In contrast the soft parameters are known to be independent of the high scale, specifically of the GUT scale [6]. For this reason we will not consider any specific high scale model but rather focus on weak scale supersymmetry which is determined by the soft parameters independent of the GUT scale [6].

Chapter 5

Experimental Constraints on Unified Models

Below we summarize the relevant constraints from collider and from astrophysical data that are applied throughout the analysis unless stated otherwise.

1. WMAP 3 year data: The lightest R-Parity odd supersymmetric particle (LSP) is assumed charge neutral. The constraint on the relic abundance of dark matter under the assumption that the relic abundance of neutralinos is the dominant component places the bound: $0.0855 < \Omega_{\tilde{\chi}_1^0} h^2 < 0.1189 \;\; (2\sigma)$ [71].

2. As is well known sparticle loop exchanges make a contribution to the FCNC process $b \to s\gamma$ which is of the same order as the Standard Model contributions (for an update of SUSY contributions see [72]). The experimental limits on $b \to s\gamma$ impose severe constraints on the SUSY parameter space and we use here the constraints from the Heavy Flavor Averaging Group (HFAG) [73] along with the BABAR, Belle and CLEO experimental results: $\mathcal{B}r(b \to s\gamma) = (355 \pm 24^{+9}_{-10} \pm 3) \times 10^{-6}$. A new estimate of $\mathcal{B}r(\bar{B} \to X_s\gamma)$ at $O(\alpha_s^2)$ gives [74] $\mathcal{B}r(b \to s\gamma) = (3.15 \pm 0.23) \times 10^{-4}$ which moves the previous SM mean value of 3.6×10^{-4}

a bit lower. In order to accommodate this recent analysis on the SM mean, as well as the previous analysis, we have taken a wider 3.5σ error corridor around the HFAG value in our numerical analysis. The total $\mathcal{B}r(\bar{B} \to X_s\gamma)$ including the sum of SM and SUSY contributions are constrained by this corridor. With a 2σ corridor, while some of the allowed points in our analysis will be eliminated, the main results of our pattern analysis remain unchanged.

3. The process $B_s \to \mu^+\mu^-$ can become significant for large $\tan\beta$ since the decay has a leading $\tan^6\beta$ [75] dependence and thus large $\tan\beta$ could be constrained by the experimental limit $\mathcal{B}r(B_s \to \mu^+\mu^-) < 1.5 \times 10^{-7}$ (90% CL), 2.0×10^{-7} (95% CL) [136]. This limit has just recently been updated [76] and gives $\mathcal{B}r(B_s \to \mu^+\mu^-) < 1.2\times10^{-7}$ (95% CL). Preliminary analyses [77] have reported the possibility of even more stringent constraints by a factor of 10. We take a more conservative approach in this analysis and allow model points subject to the bound $\mathcal{B}r(B_s \to \mu^+\mu^-) < 9 \times 10^{-6}$ (for a review see [78]).

4. Additionally, we also impose a lower limit on the lightest CP even Higgs boson mass. For the Standard Model like Higgs boson this limit is ≈ 114.4 GeV [79], while a limit of 108.2 GeV at 95% CL is set on the production of an invisibly decaying Standard Model like Higgs by OPAL [80]. For the MSSM we take the constraint to be $m_h > 100$ GeV. A relaxation of the light Higgs mass constraint by 8 - 10 GeV affects mainly the analysis of SUGRA models where the stop mass can be light. However, light stops are possible even with the strictest imposition of the LEP bounds on the SM Higgs Boson. We take the other sparticle mass constraints to be $m_{\widetilde{\chi}_1^\pm} > 104.5$ GeV [81] for the lighter chargino, $m_{\widetilde{t}_1} > 101.5$ GeV for the lighter stop, and $m_{\widetilde{\tau}_1} > 98.8$ GeV for the lighter stau.

In addition to the above one may also consider the constraints from the anomalous magnetic moment of the muon. It is known that the supersymmetric electroweak corrections to $g_\mu - 2$ can be as large or larger than the Standard Model electroweak corrections [82]. The implications of recent experimental data has been discussed in several works (see, e.g.[83]). As in [33], here we use a rather conservative bound $-11.4 \times 10^{-10} < g_\mu - 2 < 9.4 \times 10^{-9}$.

Chapter 6

The SUGRA Sparticle Patterns

In this chapter, we discuss the possible sparticle mass hierarchical patterns arising from SUGRA models utilizing the Monte Carlo simulations. We also discuss the correlation between the sparticle patterns and the nature of the soft parameter space. Finally we give a collection of benchmarks for each of the sparticle patterns analyzed here.

6.1 The Sparticle Landscape

The analysis proceeds by specifying the model input parameters at the GUT scale, $M_G \sim 2\times10^{16}$ GeV, (for our analysis, no flavor mixing is considered at the GUT scale) and using the renormalization group equations (RGEs) to predict the sparticle masses and mixing angles at the electroweak scale. The RGE code used to obtain the mass spectrum is SuSpect 2.34 [84], which is the default RGE calculator in MicrOMEGAs version 2.0.7 [63]. We have also investigated other RGE programs including ISASUGRA/ISAJET [85], SPheno [86] and SOFTSUSY [87]. We have cross checked our analysis using different codes and find no significant disagreement in most regions of

the parameter space. The largest sensitivity appears to arise for the case of large $\tan\beta$ and the analysis is also quite sensitive to the running bottom mass and to the top pole mass (we take $m_b^{\overline{\rm MS}}(m_b) = 4.23$ GeV and $m_t(\text{pole}) = 170.9$ GeV in this analysis). Such sensitivities and their implications for the analysis of relic density calculations

mSP	Mass Pattern	$\mu > 0$	$\mu < 0$
mSP1	$\widetilde{\chi}_1^0 < \widetilde{\chi}_1^\pm < \widetilde{\chi}_2^0 < \widetilde{\chi}_3^0$	Y	Y
mSP2	$\widetilde{\chi}_1^0 < \widetilde{\chi}_1^\pm < \widetilde{\chi}_2^0 < A/H$	Y	Y
mSP3	$\widetilde{\chi}_1^0 < \widetilde{\chi}_1^\pm < \widetilde{\chi}_2^0 < \widetilde{\tau}_1$	Y	Y
mSP4	$\widetilde{\chi}_1^0 < \widetilde{\chi}_1^\pm < \widetilde{\chi}_2^0 < \widetilde{g}$	Y	Y
mSP5	$\widetilde{\chi}_1^0 < \widetilde{\tau}_1 < \widetilde{l}_R < \widetilde{\nu}_\tau$	Y	Y
mSP6	$\widetilde{\chi}_1^0 < \widetilde{\tau}_1 < \widetilde{\chi}_1^\pm < \widetilde{\chi}_2^0$	Y	Y
mSP7	$\widetilde{\chi}_1^0 < \widetilde{\tau}_1 < \widetilde{l}_R < \widetilde{\chi}_1^\pm$	Y	Y
mSP8	$\widetilde{\chi}_1^0 < \widetilde{\tau}_1 < A \sim H$	Y	Y
mSP9	$\widetilde{\chi}_1^0 < \widetilde{\tau}_1 < \widetilde{l}_R < A/H$	Y	Y
mSP10	$\widetilde{\chi}_1^0 < \widetilde{\tau}_1 < \widetilde{t}_1 < \widetilde{l}_R$	Y	
mSP11	$\widetilde{\chi}_1^0 < \widetilde{t}_1 < \widetilde{\chi}_1^\pm < \widetilde{\chi}_2^0$	Y	Y
mSP12	$\widetilde{\chi}_1^0 < \widetilde{t}_1 < \widetilde{\tau}_1 < \widetilde{\chi}_1^\pm$	Y	Y
mSP13	$\widetilde{\chi}_1^0 < \widetilde{t}_1 < \widetilde{\tau}_1 < \widetilde{l}_R$	Y	Y
mSP14	$\widetilde{\chi}_1^0 < A \sim H < H^\pm$	Y	
mSP15	$\widetilde{\chi}_1^0 < A \sim H < \widetilde{\chi}_1^\pm$	Y	
mSP16	$\widetilde{\chi}_1^0 < A \sim H < \widetilde{\tau}_1$	Y	
mSP17	$\widetilde{\chi}_1^0 < \widetilde{\tau}_1 < \widetilde{\chi}_2^0 < \widetilde{\chi}_1^\pm$		Y
mSP18	$\widetilde{\chi}_1^0 < \widetilde{\tau}_1 < \widetilde{l}_R < \widetilde{t}_1$		Y
mSP19	$\widetilde{\chi}_1^0 < \widetilde{\tau}_1 < \widetilde{t}_1 < \widetilde{\chi}_1^\pm$		Y
mSP20	$\widetilde{\chi}_1^0 < \widetilde{t}_1 < \widetilde{\chi}_2^0 < \widetilde{\chi}_1^\pm$		Y
mSP21	$\widetilde{\chi}_1^0 < \widetilde{t}_1 < \widetilde{\tau}_1 < \widetilde{\chi}_2^0$		Y
mSP22	$\widetilde{\chi}_1^0 < \widetilde{\chi}_2^0 < \widetilde{\chi}_1^\pm < \widetilde{g}$		Y

Table 6.1: Hierarchical mass patterns for the four lightest sparticles in mSUGRA when $\mu < 0$ and $\mu > 0$. The patterns can be classified according to the next to the lightest sparticle. For the mSUGRA analysis the next to the lightest sparticle is found to be either a chargino, a stau, a stop, a CP even/odd Higgs, or the next lightest neutralino $\widetilde{\chi}_2^0$. The notation A/H stands for either A or H. In mSP14-mSP16 it is possible that the Higgses become lighter than the LSP. Y stands for appearance of the pattern for the sub case.

are well known in the literature [88] and a detailed comparison for various codes can

be found in Refs. ([89], [90], [91], [92]).

6.1.1 The mSUGRA landscape for the 4 lightest sparticles

As discussed in chapter (4), one mSUGRA model is a point in a 4 dimensional parameter space spanned by the soft parameters m_0, $m_{1/2}$, A_0, $\tan\beta$, and the sign of μ. Typically scans of the parameter space are done by taking a vanishing trilinear coupling, and/or by looking at fixed values of $\tan\beta$ while varying (m_0, $m_{1/2}$). In this work we carry out a random scan in the 4-D input parameter space for both signs of μ with Monte Carlo simulations using flat priors under the following ranges of the input parameters

$$0 < m_0 < 4 \text{ TeV}, \quad 0 < m_{1/2} < 2 \text{ TeV} \quad |A_0/m_0| < 10, \quad 1 < \tan\beta < 60. \tag{6.1}$$

Since SUGRA models with $\mu > 0$ are favored by the experimental constraints much of the analysis presented here focuses on this case. Specifically for the $\mu > 0$ mSUGRA case, we perform a scan of the parameter space with a total of 2×10^6 trial parameter points. We delineate the patterns that emerge for the first four lightest sparticles. Here we find that at least sixteen hierarchical mass patterns emerge which are labeled as mSPs (minimal SUGRA Pattern). These mSPs can be generally classified according to the type of particle which is next heavier than the LSP, and we find four classes of patterns in mSUGRA: the chargino patterns (CP), the stau patterns (SUP), the stop patterns (SOP), and the Higgs patterns (HP), as exhibited below

1. Chargino patterns (CP) : mSP1, mSP2, mSP3, mSP4;

2. Stau patterns (SUP) : mSP5, mSP6, mSP7, mSP8, mSP9, mSP10;

3. Stop patterns (SOP) : mSP11, mSP12, mSP13;

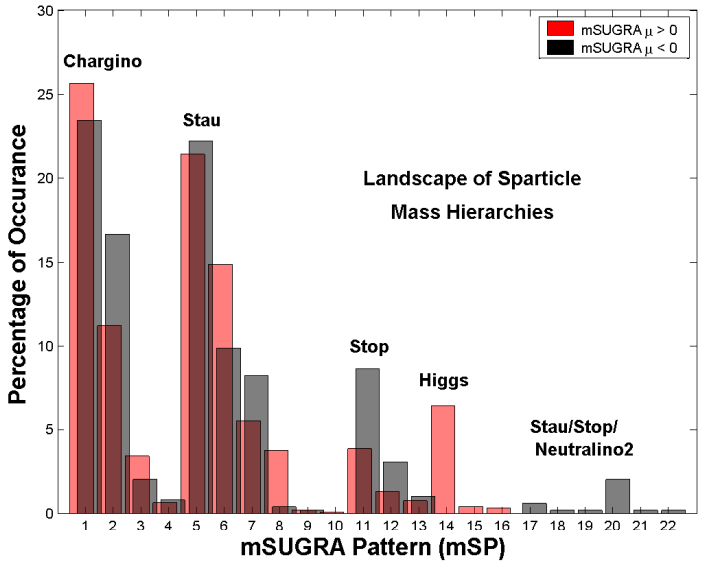

Figure 6.1: Distribution of the surviving hierarchical mass patterns in the landscape for the mSUGRA model with $\mu > 0$ (light) and $\mu < 0$ (dark), under various constraints as discussed in the text.

4. Higgs patterns (HP) : mSP14, mSP15, mSP16.

The hierarchical mass patterns mSP1-mSP16 are defined in Table (6.1). We note that the pattern mSP7 appears in the analyses of [93, 94, 95]. We also performed a similar scan for the mSUGRA with $\mu < 0$ case using the Monte Carlo simulation with flat priors and the same parameter ranges as specified in Eq. (6.1). Most of the mSP patterns that appear in the $\mu > 0$ case also appear in the $\mu < 0$ case (see Table (6.1)). However, in addition one finds new patterns shown below

1. Stau patterns (SUP) : mSP17, mSP18, mSP19;

2. Stop patterns (SOP) : mSP20, mSP21;

3. Neutralino patterns (NP) : mSP22.

We note that the analysis of Ref. [96] has a sparticle spectrum which corresponds to mSP11 and contains light stops. Light stops have also been discussed recently in

Snowmass	mSP
SPS1a, SPS1b, SPS5	mSP7
SPS2	mSP1
SPS3	mSP5
SPS4, SPS6	mSP3

Post-WMAP3	mSP
$A', B', C', D', G', H', J', M'$	mSP5
I', L'	mSP7
E'	mSP1
K'	mSP6

CMS LM/HM	mSP
LM1, LM6, HM1	mSP5
LM2, LM5, HM2	mSP7
LM3, LM7, LM8, LM9, LM10, HM4	mSP1
LM4, HM3	mSP3

Table 6.2: Mapping between the mSPs and the Snowmass, Post-WMAP3, and CMS benchmark points. The points $B' = \text{LM1}$, $I' = \text{LM2}$, $C' = \text{LM6}$. HM1 in SuSpect has $m_{\widetilde{\chi}_1^0} > m_{\widetilde{\tau}_1}$, but this is not the case for ISAJET, SPheno, and SOFTSUSY. Among the CMS benchmarks, only LM1, LM2, LM6, and HM1, HM2 are capable of giving the correct relic density. Thus the mapping above applies only to the mass pattern, while all of our mSP and NUSP benchmark points satisfy the relic density constraints from MicrOMEGAs with SuSpect. The CMS test points do a better job of representing mSP1 which is the dominant pattern found in our analysis. There are no HP test points or SOP test points in any of the previous works.

[97, 35].

While the earlier works which advocated benchmark points and slopes made good progress in systematizing the search for supersymmetry, we find that they do not cover the more broad set of possible mass hierarchies we discuss here. That is, many of the mSP patterns do not appear in the earlier works that advocated benchmark points for SUSY searches. For example, the Snowmass mSUGRA points (labeled SPS) [98] and the Post-WMAP benchmark points of [99], make up only a small fraction of the possible mass hierarchies listed in Table (6.1). The CMS benchmarks classified as Low Mass (LM) and High Mass (HM) [100] (for a recent review see [101, 102]) does a good job covering the mSP1 pattern which appears as the most dominant pattern in our analysis, but there are no Higgs patterns or stop patterns discussed in the CMS benchmarks as well as in SPS or in Post-WMAP benchmarks. We exhibit the

mapping of mSPs with other benchmarks points in a tabular form in Table (6.2).

In Fig. (6.1) we give the relative distribution of these hierarchies found in our Monte Carlo scan. Because the scan is done randomly within the soft parameter space, the distribution of sparticle patterns in Fig. (6.1) represents the probability of finding these patterns in the parameter space. The most common patterns found here are CPs and SUPs, especially mSP1 and mSP5. However there exists a significant region of the parameter space where SOPs and HPs can be realized. The percentages of occurrence of the various patterns in the mSUGRA landscape for both μ positive and μ negative are exhibited in Fig. (6.1). The analysis of Fig. (6.1) shows that the chargino patterns (CP) are the most dominant patterns, followed by the stau patterns (SUP), the stop patterns (SOP), and the Higgs patterns (HP). In contrast, most emphasis in the literature, specifically in the context of relic density analysis, has focused on the stau patterns, with much less attention on other patterns. Specifically the Higgs patterns have hardly been investigated or discussed. The exceptions to this, in the context of the Higgs patterns, are the more recent works of Refs. [22, 23], and similar mass ranges for the Higgs bosons have been studied in [103] (see also [104]).

6.1.2 The landscape of the 4 lightest sparticles in NUSUGRA

Next we discuss the landscape of the 4 lightest sparticles for the case of nonuniversal supergravity models. Here we consider nonuniversalities in the Higgs sector (NUH), in the third generation sector (NU3), and in the gaugino sector (NUG). Such nonuniversalities appear quite naturally in supergravity models with a non-minimal Kähler potential, and in string and D-Brane models. The parametrization of the

nonuniversalities is given by

$$\begin{aligned} \text{NUH} &: M_{H_u} = m_0(1+\delta_{H_u}), \quad M_{H_d} = m_0(1+\delta_{H_d}), \\ \text{NU3} &: M_{q3} = m_0(1+\delta_{q3}), \quad M_{u3,d3} = m_0(1+\delta_{tbR}), \\ \text{NUG} &: M_1 = m_{1/2}, \quad M_{2,3} = m_{1/2}(1+\delta_{M_{2,3}}). \end{aligned} \tag{6.2}$$

In the above δ_{H_u} and δ_{H_d} define the nonuniversalities for the up and down Higgs mass parameters, M_{q3} is the left-handed squark mass for the 3rd generation, and M_{u3} (M_{d3}) are the right-handed u-squark (d-squark) masses for the 3rd generation. The nonuniversalities in the gaugino sector are parameterized here by δ_{M_2} and δ_{M_3}. We have carried out a Monte Carlo scan with flat priors using 10^6 model points in each of the three types of NUSUGRA models, taking the same input parameter ranges as specified in Eq. (6.1) and $-0.9 \leqslant \delta \leqslant 1$. Almost all of the mSP patterns seen for the mSUGRA cases were found in supergravity models with nonuniversal soft breaking, as the mSUGRA model is contained within the nonuniversal supergravity models. In addition we find many new patterns labeled NUSPs (nonuniversal SUGRA pattern), and they are exhibited in Table (6.3). As in the mSUGRA case one finds several pattern classes, CPs, SUPs, SOPs, and HPs as exhibited below. In addition, we find several Gluino patterns (GP) where the gluino is the NLSP.

1. Chargino patterns (CP) : NUSP1, NUSP2, NUSP3, NUSP4;

2. Stau patterns (SUP) : NUSP5, NUSP6, NUSP7, NUSP8, NUSP9;

3. Stop patterns (SOP) : NUSP10, NUSP11;

4. Higgs patterns (HP) : NUSP12;

5. Gluino patterns (GP) : NUSP13, NUSP14, NUSP15.

It is interesting to note that for the 4 sparticle landscape we find saturation in the number of mass hierarchies that are present. For example, for the case $\mu > 0$ in mSUGRA , increasing the soft parameter scan from 1×10^6 parameter model points to 2×10^6 model points does not increase the number of 4 sparticle patterns. In this context it becomes relevant to examine as to what degree the relic density and other experimental constraints play a role in constraining the parameter space and thus reducing the number of patterns. This is exhibited in Table (6.4) where we

NUSP	Mass Pattern	NU3	NUG
NUSP1	$\widetilde{\chi}_1^0 < \widetilde{\chi}_1^\pm < \widetilde{\chi}_2^0 < \widetilde{t}_1$	Y	Y
NUSP2	$\widetilde{\chi}_1^0 < \widetilde{\chi}_1^\pm < A \sim H$	Y	
NUSP3	$\widetilde{\chi}_1^0 < \widetilde{\chi}_1^\pm < \widetilde{\tau}_1 < \widetilde{\chi}_2^0$		Y
NUSP4	$\widetilde{\chi}_1^0 < \widetilde{\chi}_1^\pm < \widetilde{\tau}_1 < \widetilde{l}_R$		Y
NUSP5	$\widetilde{\chi}_1^0 < \widetilde{\tau}_1 < \widetilde{\nu}_\tau < \widetilde{\tau}_2$	Y	
NUSP6	$\widetilde{\chi}_1^0 < \widetilde{\tau}_1 < \widetilde{\nu}_\tau < \widetilde{\chi}_1^\pm$	Y	
NUSP7	$\widetilde{\chi}_1^0 < \widetilde{\tau}_1 < \widetilde{t}_1 < A/H$		Y
NUSP8	$\widetilde{\chi}_1^0 < \widetilde{\tau}_1 < \widetilde{l}_R < \widetilde{\nu}_\mu$		Y
NUSP9	$\widetilde{\chi}_1^0 < \widetilde{\tau}_1 < \widetilde{\chi}_1^\pm < \widetilde{l}_R$		Y
NUSP10	$\widetilde{\chi}_1^0 < \widetilde{t}_1 < \widetilde{g} < \widetilde{\chi}_1^\pm$		Y
NUSP11	$\widetilde{\chi}_1^0 < \widetilde{t}_1 < A \sim H$		Y
NUSP12	$\widetilde{\chi}_1^0 < A \sim H < \widetilde{g}$		Y
NUSP13	$\widetilde{\chi}_1^0 < \widetilde{g} < \widetilde{\chi}_1^\pm < \widetilde{\chi}_2^0$		Y
NUSP14	$\widetilde{\chi}_1^0 < \widetilde{g} < \widetilde{t}_1 < \widetilde{\chi}_1^\pm$		Y
NUSP15	$\widetilde{\chi}_1^0 < \widetilde{g} < A \sim H$		Y

Table 6.3: New 4 sparticle mass patterns that arise in NUSUGRA over and above the mSP patterns of Table (6.1). These are labeled nonuniversal SUGRA patterns (NUSP) and at least 15 new patterns are seen to emerge which are denoted by NUSP1-NUSP15.

demonstrate how the relic density and the other experimental constraints decrease the number of admissible model points in the allowed parameter space for the mSUGRA models with both $\mu > 0$ and $\mu < 0$, and also for the cases with nonuniversalities in the Higgs sector, nonuniversalities in the third generation sector, and with nonuniver-

salities in the gaugino sector. In each case we start with 10^6 model points at the GUT scale, and find that the electroweak symmetry breaking constraints reduce the number of viable models to about 1/4 of what we started with. We find that the allowed number of models translates into SUGRA mass patterns which are typically less than 100. The admissible set of parameter points reduces drastically when the relic density constraints are imposed and are then found to typically reduce the number of models by a factor of about 200 or more, with a reduction in the number of allowed patterns by a factor of 2 or more. Inclusion of all other experimental constraints further reduces the number of admissible points by a factor between 30% and 50%, with a corresponding reduction in the number of patterns by up to 40%. The above analysis shows that there is an enormous reduction in the number of admissible models and the corresponding number of hierarchical mass patterns after the constraints of radiative breaking of the electroweak symmetry, relic density constraints, and other experimental constraints are imposed.

Model Type	Trial Models	Output Models	No. of Patterns	Relic Density Constraints	No. of Patterns	All Constraints	No. of Patterns
mSUGRA($\mu > 0$)	10^6	265,875	55	1,360	22	902	16
mSUGRA($\mu < 0$)	10^6	226,991	63	1,000	31	487	18
NUH($\mu > 0$)	10^6	222,023	59	1,024	24	724	15
NU3($\mu > 0$)	10^6	229,928	73	970	28	650	20
NUG($\mu > 0$)	10^6	273,846	103	1,788	36	1,294	28

Table 6.4: An analysis of mass patterns for the four lightest sparticles. Exhibited here are the model type, the number of trial input points for each model, the number surviving the radiative electroweak symmetry breaking scheme as given by SuSpect (column 3), the number surviving when the relic density constraints are applied with MicrOMEGAs (column 5), the number surviving with inclusion of all experimental collider constraints (column 7), along with the corresponding number of hierarchical mass patterns in each case (column 8).

6.1.3 Hierarchical patterns for the full sparticle spectrum

We discuss now the number of hierarchical mass patterns for the full set of 32 sparticles in SUGRA models when the constraints of electroweak symmetry, relic density, and other experimental constraints are imposed. The result of the analysis is given in Fig. (6.2) and Table (6.5). The left panel of Fig. (6.2) shows the number of hierarchical mass patterns for 32 sparticles vs the number of trial points for mSUGRA models which survive the electroweak symmetry breaking constraints, the relic density and all other experimental constraints. The number of hierarchical mass patterns show a trend towards saturation. In the right panel, a similar phenomenon is seen in the ratio between the number of patterns over the number of surviving trial points

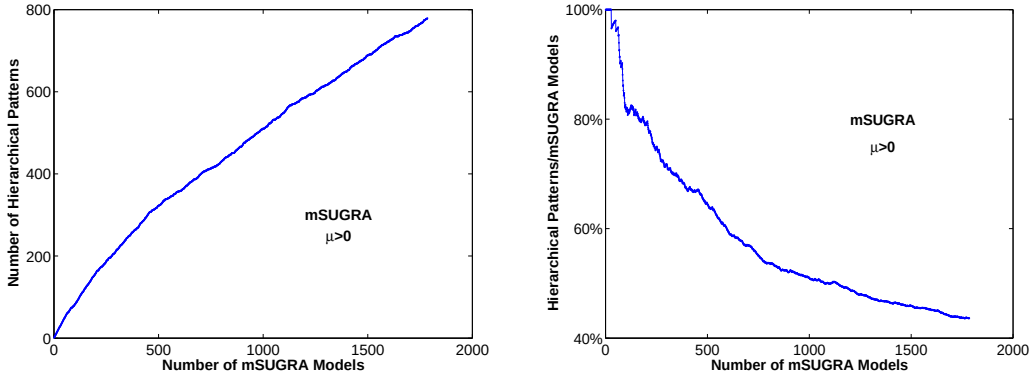

Figure 6.2: Saturation of Sparticle patterns.

Models [No.]	No. after constraints	No. of patterns
mSUGRA($\mu > 0$) [10^6]	902	505
mSUGRA($\mu < 0$) [10^6]	487	268
NUH($\mu > 0$) [10^6]	724	517
NU3($\mu > 0$) [10^6]	650	528
NUG($\mu > 0$) [10^6]	1294	1092
All Above[5×10^6]	4057	2557

Table 6.5: Exhibition of mass patterns and models with various constraints. Column 1 shows one million input parameter points for each of the models investigated, and the number surviving all the constraints are exhibited in column 2, while column 3 gives the number of hierarchical patterns.

erarchical mass patterns for 32 sparticles vs the number of trial points for mSUGRA models which survive the electroweak symmetry breaking constraints, the relic density and all other experimental constraints. The number of hierarchical mass patterns show a trend towards saturation. In the right panel, a similar phenomenon is seen in the ratio between the number of patterns over the number of surviving trial points

in mSUGRA models. Here one finds that increasing the number of model points in the scan does increase the number of patterns. However, the ratio of the number of patterns to the total number of models that survive all the constraints from the scan decreases sharply as shown in the right panel of Fig. (6.2). This means that although saturation is not yet achieved one is moving fast towards achieving saturation with a relatively small number of allowed patterns for all the 32 sparticles within SUGRA models consistent with the various experimental constraints. The analysis of Table (6.5) shows that the number of allowed patterns for the 32 sparticles, which in the MSSM without the SUGRA framework can be as large as $O(10^{25})$ or larger, reduces rather drastically when various constraints are applied in supergravity models.

The Table (6.5) exhibits a dramatic reduction of the landscape from upward of $\sim O(10^{25})$ hierarchical mass patterns for the 32 sparticle masses to a much smaller number when the electroweak symmetry breaking constraints, the relic density constraints, and other experimental constraints are applied. We note that some patterns are repeated as we move across different model types listed in the first column of Table (6.5). Thus the total number of patterns listed at the bottom of the last column of this table is smaller than the sum of patterns listed above in that column. We note that the precise number and nature of the patterns are dependent on the input parameters such as the top mass and a significant shift in the input values could modify the pattern structure.

6.2 Sparticle Patterns & Nature of Soft Breaking

It is interesting to ask if the patterns can be traced back to some specific regions of the parameter of soft breaking from where they originate. This indeed is the case, at least, for some of the patterns. The analysis illustrating the origin of the patterns

in the parameter space is given in Fig. (6.3). The dispersion of mSPs arising in mSUGRA in the $\tan\beta$ vs A_0/m_0 plane (left panels), and in the m_0 vs $m_{1/2}$ plane (right panels) for the $\mu > 0$ case (upper panels) and $\mu < 0$ case (lower panels). The analysis is based on a scan of 10^6 trial model points with flat priors in the ranges $m_0 < 4$ TeV, $m_{1/2} < 2$ TeV, $1 < \tan\beta < 60$, and $|A_0/m_0| < 10$. mSP1 is confined to the region where $|A_0/m_0| < 2$. For the case $\mu < 0$, no HPs are seen, and also, no model points survive in the region where $\tan\beta > 50$ in contrast to the $\mu > 0$ case where there is a significant number for $\tan\beta \gtrsim 45$. Many interesting observations can be made from these spectral decompositions. For example, a significant set of the mSP1 (CP) models lie in the region $|A_0/m_0| < 2$ and correspond to the Hyperbolic branch/Focus Point (HB/FP) [45] regions, while most of the SOPs have a rather large ratio of A_0/m_0 with the satisfaction of REWSB. In this analysis we require that there be no charge or color breaking (CCB) [105, 106] at the electroweak scale. We note in passing that it has been argued that even if the true minimum is not color or charge preserving, the early universe is likely to occupy the CCB preserving minimum and such minima may still be acceptable if the tunneling lifetime from the false to the true vacuum is much greater than the present age of the universe [107]. Next, we note that for the mSUGRA $\mu > 0$ case, the region around $\tan\beta = 50$ has a large number of models that can be realized, while the region around $\tan\beta = 30$ has far less model points. We also note that most of the HPs reside only in the very high $\tan\beta$ region in mSUGRA, but this situation can be changed significantly in the NUH case where HP points can be realized in the $\tan\beta$ region as low as $\tan\beta \sim 20$. In the m_0 vs $m_{1/2}$ plane, one finds that most of CPs and HPs have a larger universal scalar mass than most of the SUPs and SOPs.

Often in the literature one limits the analysis by fixing specific values of A_0 and $\tan\beta$. For A_0 the value most investigated is $A_0 = 0$. However, constraining the

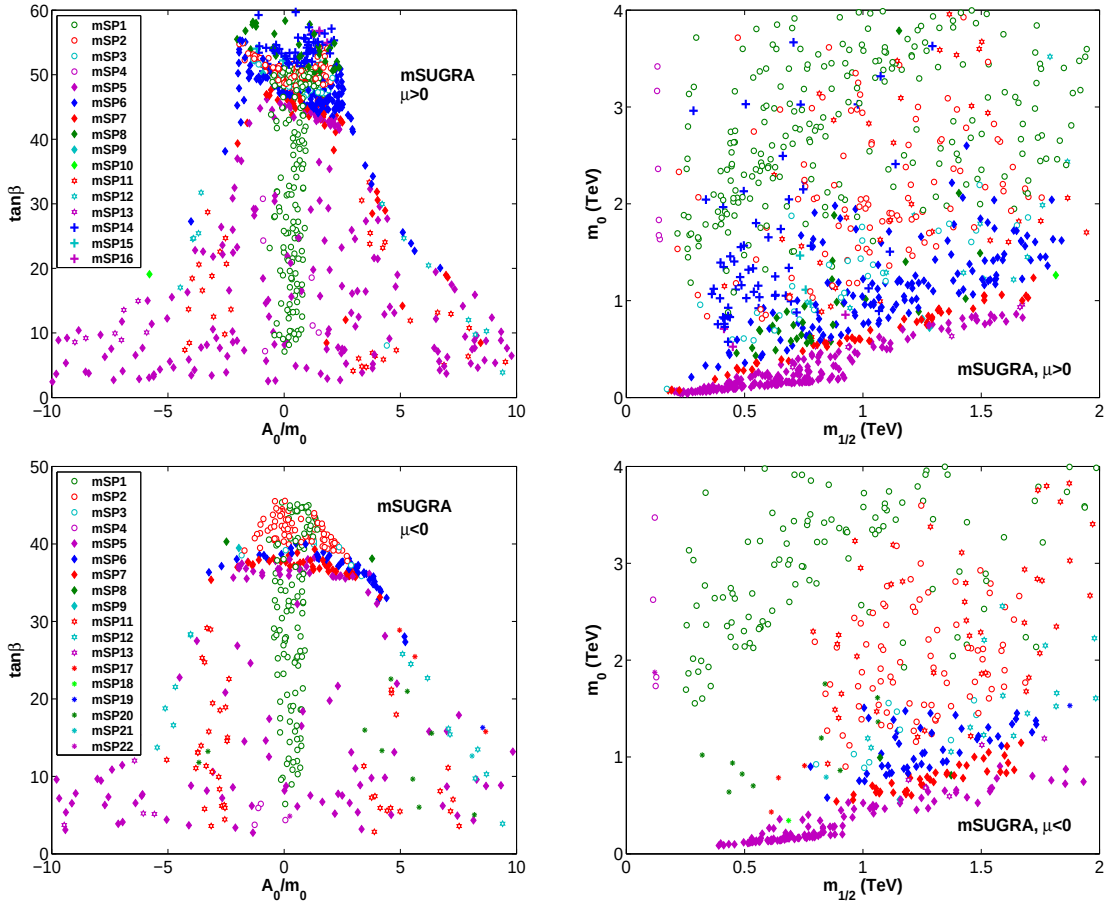

Figure 6.3: Spectrum decomposition of soft parameter space. Exhibited are the landscape of sparticle mass spectra in the planes (I) $\tan\beta$ vs A_0/m_0 and (II) m_0 vs $m_{1/2}$, when the soft parameters are allowed to vary in the ranges given in Eq. (6.1).

values of A_0 or of $\tan\beta$ artificially eliminates a very significant part of the allowed parameter space where all the relevant constraints (the REWSB constraint as well as the relic density and the experimental constraints) can be satisfied as seen in Fig. (6.3). One can extract the familiar plots one finds in the literature where A_0 and $\tan\beta$ are constrained from a reduction of the top-right panel of Fig. (6.3). The results of this reduction are shown in Fig. (6.4) with a focused scan in specific regions of the soft parameter space. Fig. (6.4) shows a dispersion of patterns in the m_0 vs $m_{1/2}$ plane for fixed values of $\tan\beta$ and A_0/m_0. The region scanned is in the range

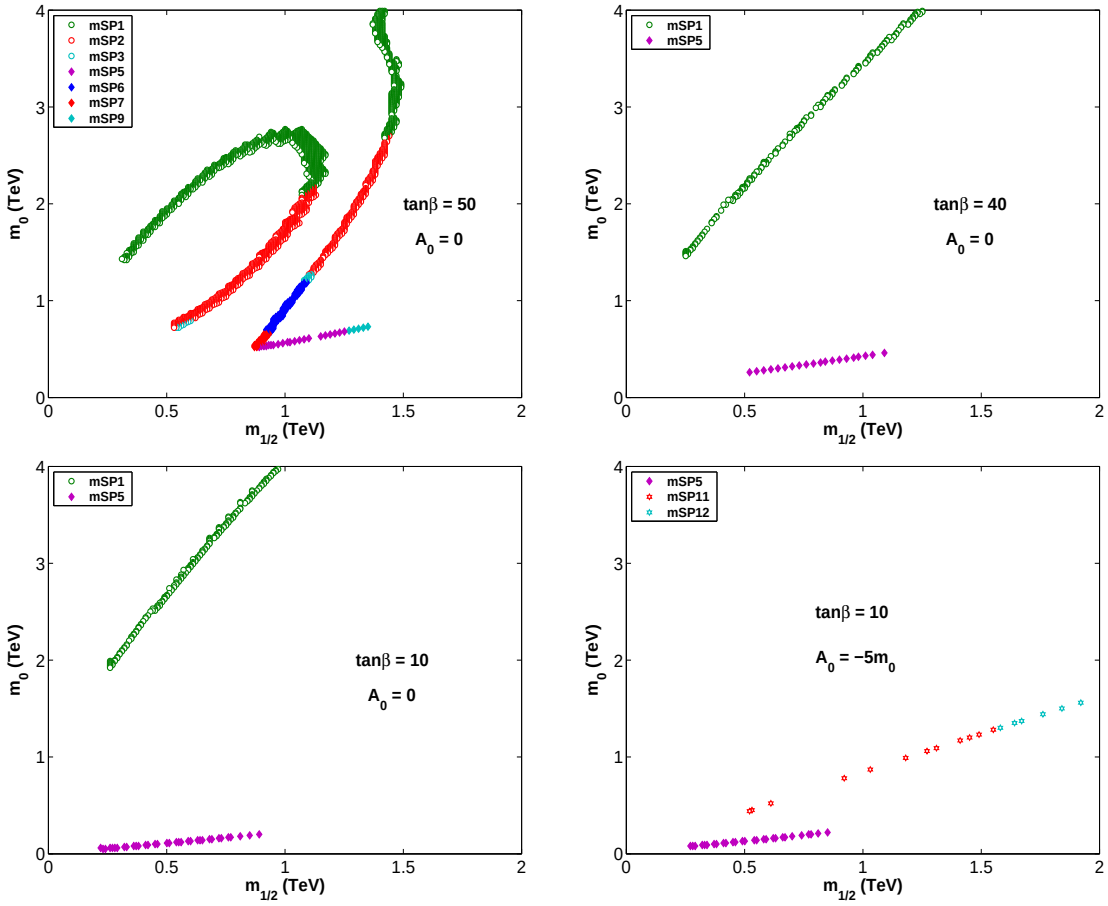

Figure 6.4: Dispersion of patterns in some special 2D surface of mSUGRA space.

$m_0 < 4$ TeV and $m_{1/2} < 2$ TeV with a 10 GeV increment for each mass. Only a subset of the allowed parameter points relative to Fig. (6.3) remain, since the scans are on constrained surfaces in the mSUGRA parameter space. Specifically the bottom-left and top-right panels of Fig. (6.4) show the familiar stau coannihilation [108, 109, 93] regions and the HB/FP branch, the bottom-right panel gives the stau coannihilation region and the stop coannihilation region because of the relatively large A_0 value, and the top-left panel is of the form seen in the works of Djouadi et al. [33] where the Higgs funnel plays an important role in the satisfaction of the relic density.

A similar analysis for the nonuniversal case is given in Fig. (6.5) which exhibits the NUSPs and mSPs for the NUH, NU3, and NUG models in the $\tan\beta$ vs A_0/m_0

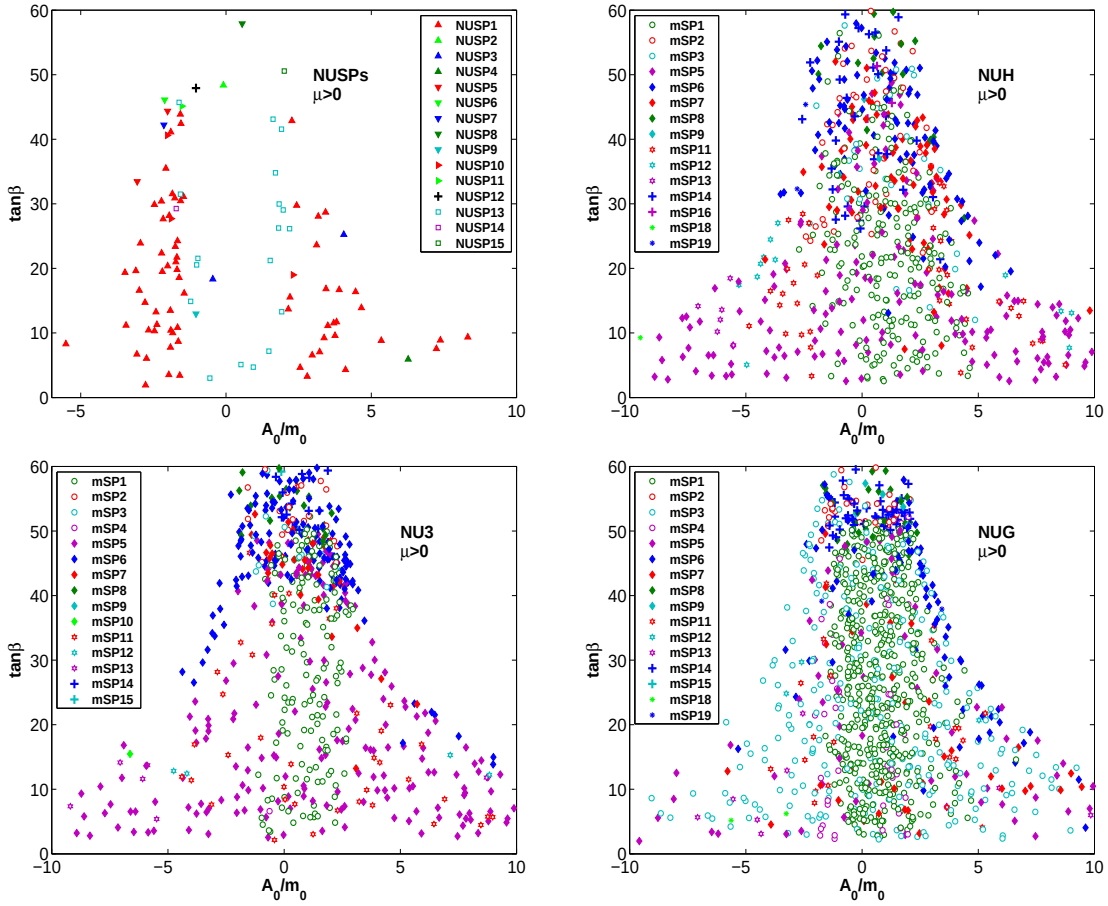

Figure 6.5: Exhibition of NUSPs and mSPs arising from NUSUGRA models.

plane. The range of SUGRA parameters are the same as the case mSUGRA ($\mu > 0$). One may notice that the mSP1 points arising from NU models lie in a relatively larger A_0/m_0 region. Most of the models in NU cases are still mSPs, and among the NUSPs, only two patterns have a relatively large population, these being NUSP1 and NUSP13. One may also notice that in NUH case, the HPs can exist in a low $\tan\beta$ region as opposed to the mSUGRA case where HPs can either exist in the large $\tan\beta$ region ($\mu > 0$) or are totally eliminated ($\mu < 0$). Among the NUSPs the dominant patterns are NUSP1 (CP) and NUSP13 (GP), which are seen to arise from the model with nonuniversalities in the gaugino sector, i.e., the NUG model.

6.3 Benchmarks for Sparticle Patterns

As discussed already, many of the sparticle mass patterns discussed in this analysis do not appear in the Snowmass, Post-WMAP, and CMS benchmark points. With some of these mSP and NUSP having a significant probability of occurrence, we therefore provide a larger set of benchmark points for the various patterns in different SUGRA scenarios. In Table (6.6), we give one benchmark point for each mSP pattern that are discovered in mSUGRA with $\mu > 0$.

mSUGRA Pattern	m_0 (GeV)	$m_{1/2}$ (GeV)	A_0 (GeV)	$\tan\beta$ v_u/v_d	$\mu(Q)$ (GeV)	LSP | LCP (GeV)
mSP1:	2001	411	0	30	216	156.1 | 202.6
mSP2:	1125	614	2000	50	673	256.7 | 483.1
mSP3:	741	551	0	50	632	230.5 | 434.7
mSP4:	1674	137	1985	18.6	533	54.3 | 106.9
mSP5:	111	531	0	5	679	217.9 | 226.3
mSP6:	245	370	945	31	427	148.6 | 156.8
mSP7:	75	201	230	14	246	74.8 | 100.2
mSP8:	1880	877	4075	54.8	1141	373.1 | 379.6
mSP9:	667	1154	-125	51	1257	499.2 | 501.8
mSP10:	336	772	-3074	10.8	1695	329.2 | 331.7
mSP11:	871	1031	-4355	10	2306	447.1 | 491.5
mSP12:	1371	1671	-6855	10	3593	741.2 | 791.8
mSP13:	524	800	-3315	15	1782	342.7 | 383.8
mSP14:	1036	562	500	53.5	560	236.2 | 399.1
mSP15:	1113	758	1097	51.6	724	321.1 | 595.9
mSP16:	525	450	641	56	484	184.6 | 257.9

Table 6.6: Benchmarks using SUSPECT 2.3 with one point for each mass pattern mSP1-mSP16. Also given are the neutralino LSP (Lightest SUSY (R parity odd) Particle), and the Lightest Charged Particle (LCP) masses. We take $\mu > 0$, ${m_b}^{\overline{\rm MS}}(m_b) = 4.23$ GeV, ${\alpha_s}^{\overline{\rm MS}}(M_Z) = .1172$, and $m_t(\text{pole}) = 170.9$ GeV. At least five LCP from these benchmarks will be accessible at the International Linear Collider (ILC).

We also provide a large collection of benchmark points which are exhibited in Tables (15.1, 15.2, 15.3, 15.4, 15.5) in the Appendix. Each of these benchmarks

satisfies the relic density and other experimental constraints with SuSpect linked to MicrOMEGAs. We have explicitly checked that the first mSP benchmark point in each of the tables can be reproduced by using SPheno, and SOFTSUSY by allowing minor variations on the input parameters. The benchmarks are chosen to cover wide parts of the SUGRA parameter space. We give these benchmarks, several for each mass pattern, as the search for SUSY from the point of view of mass patterns has important consequences for LHC experimental searches. Some of the patterns are correlated with certain well investigated phenomena such as the HB/FP branches of REWSB and the stau-neutralino co-annihilation regions. However, many of the patterns arise from multiple annihilation processes.

Chapter 7

Sparticle Signatures at the Large Hadron Collider

In this chapter, first we will give the detailed description of our LHC simulations. And then we will give our post trigger cuts and all the signatures investigated.

7.1 LHC Simulations

After the imposition of all the constraints mentioned in the previous sections, such as the relic density constraints from WMAP data, the constraints on the FCNCs, as well as mass limits on the sparticle spectrum, we are left with the candidate model points for the signature analysis. For each of these model points, a SUSY Les Houches Accord (SLHA) file [110] is interfaced to PYTHIA 6.4.11 [111] through PGS4 [112] for the computation of SUSY production cross sections and branching fractions. In this analysis, for signals, we have generated all of PYTHIA's $2 \rightarrow 2$ SUSY production modes using MSEL = 39. More specifically this choice generates 91 SUSY production modes including gaugino, squark, slepton, and SUSY Higgs pair production but leaves

out singly produced Higgs production. For further details, see [111]. A treatment of singly produced Higgs production in the context of sparticle mass hierarchies was included in the analysis of Ref. [23]. Leading order cross sections from PYTHIA and leading order cross sections from PROSPINO 2.0 [113] were cross checked against one another for consistency over several regions of the soft parameter space. TAUOLA [114] is called by PGS4 for the calculation of tau branching fractions as controlled in the PYTHIA parameter card (.pyt) file.

With PGS4 we use the Level 1 (L1) triggers based on the Compact Muon Solenoid detector (CMS) specifications [115, 100] and the LHC detector card. Muon isolation is controlled by employing the cleaning script in PGS4. We take the experimental nomenclature of lepton being defined only as electron or muon and thus distinguish electrons and muons from tau leptons. SM backgrounds have been generated with QCD multi-jet production due to light quark flavors, heavy flavor jets ($b\bar{b}$, $t\bar{t}$), Drell-Yan, single Z/W production in association with quarks and gluons ($Z/W+$ jets), and ZZ, WZ, WW pair production resulting in multi-leptonic backgrounds. Extraction of final state particles from the PGS4 event record is accomplished with a code SMART (= SUSY Matrix Routine) written by us [22] which provides an optimized processing of PGS4 event data files. The standard criteria for the discovery limit of new signals is that the SUSY signals should exceed either $5\sqrt{N_{\rm SM}}$ or 10 whichever is larger, i.e., $\mathrm{N_{SUSY}} > \mathrm{Max}\left\{5\sqrt{N_{\rm SM}}, 10\right\}$ and such a criteria is imposed where relevant. We have also cross checked various results of our analysis with three CMS notes [116, 117, 118] and we have found agreement with these works using SMART and PGS4 for signal and backgrounds.

We note that several works where sparticle signatures are discussed have appeared recently [119, 120, 121, 122, 123, 124]. However, the issue of hierarchical mass patterns and the correlation of signatures with such patterns has not been discussed which is

what the analysis of this work investigates.

Signature	Description	Signature	Description
0L	0 Lepton	0T	0 τ
1L	1 Lepton	1T	1 τ
2L	2 Leptons	2T	2 τ
3L	3 Leptons	3T	3 τ
4L	4 Leptons and more	4T	4 τ and more
0L1b	0 Lepton + 1 b-jet	0T1b	0 τ + 1 b-jet
1L1b	1 Lepton + 1 b-jet	1T1b	1 τ + 1 b-jet
2L1b	2 Leptons + 1 b-jet	2T1b	2 τ + 1 b-jet
0L2b	0 Lepton + 2 b-jets	0T2b	0 τ + 2 b-jets
1L2b	1 Lepton + 2 b-jets	1T2b	1 τ + 2 b-jets
2L2b	2 Leptons + 2 b-jets	2T2b	2 τ + 2 b-jets
ep	e^+ in 1L	em	e^- in 1L
mp	μ^+ in 1L	mm	μ^- in 1L
tp	τ^+ in 1T	tm	τ^- in 1T
OS	Opposite Sign Di-Leptons	0b	0 b-jet
SS	Same Sign Di-Leptons	1b	1 b-jet
OSSF	Opposite Sign Same Flavor Di-Leptons	2b	2 b-jets
SSSF	Same Sign Same Flavor Di-Leptons	3b	3 b-jets
OST	Opposite Sign Di-τ	4b	4 b-jets and more
SST	Same Sign Di-τ	TL	1 τ plus 1 Lepton

Table 7.1: The table gives a list of 40 counting signatures for each point in the SUGRA model parameter space. $L = e, \mu$ signifies only electrons and muons.

7.2 Post Trigger Level Cuts and LHC Signatures

Generally speaking, there are two kinds of LHC signatures: (i) event counting signatures, and (ii) kinematical signatures. We have investigated both of these for the purpose of discriminating the sparticle mass patterns. We list our event counting signatures in Table (7.1), where we have carried out analyses of a large set of lepton + jet signals. In our counting procedure, only electron and muon are counted as leptons, while tau jets are counted independently. For clarity, from here on, our use of 'jet(s)' will exclude tau jets. Thus, for jet identification, we divide jets into two

Kinematical signatures
1. P_T^{miss}
2. Effective Mass = $P_T^{miss} + \sum_j P_T^j$
3. Invariant Mass of all jets
4. Invariant Mass of e^+e^- pair
5. Invariant Mass of $\mu^+\mu^-$ pair
6. Invariant Mass of $\tau^+\tau^-$ pair

Table 7.2: The table give a list kinematical signatures analyzed.

categories: b-tagged jets and jets without b-tagging, which we simply label as b-jets and non-b-jets (see also [119]). There are some counting signatures that only concern one class of measurable events, for example, the number of events containing one tagged b-jet and any other final state particles. There are also types of signatures of final state particles with combinations of two or three different species. For instance, one such example would be the number of events in which there is a single lepton and a single tau.

When performing the analysis of event counting, for each SUGRA model point, we impose global post trigger cuts to analyze most of our PGS4 data. Below we give our default post trigger cuts which are used throughout this thesis unless stated otherwise.

1. In an event, we only select photons, electrons, and muons that have transverse momentum $P_T^p > 10$ GeV and $|\eta^p| < 2.4$, $p = (\gamma, e, \mu)$.

2. Taus which satisfy $P_T^\tau > 10$ GeV and $|\eta^\tau| < 2.0$ are selected.

3. For hadronic jets, only those satisfying $P_T^j > 60$ GeV and $|\eta^j| < 3$ are selected.

4. We require a large amount of missing transverse momentum, $P_T^{miss} > 200$ GeV.

5. There are at least two jets that satisfy the P_T and η cuts.

Our default post trigger level cuts are standard and are designed to suppress the Standard Model background, and highlight the SUSY events over a broad class of models.

The different kinematical signatures we investigated for the purpose of discriminating among sparticle mass patterns are exhibited in Table (7.2). One may further divide the kinematical signatures into two classes: namely those involving transverse momentum P_T and those which involve invariant mass. For those involving P_T, we have investigated missing P_T distributions and the effective mass, the latter being the sum of missing P_T and P_T of all jets contained within an event. For the kinematical variables using invariant mass, we reconstruct such quantities for four different cases, i.e., the invariant mass for all jets, for e^+e^- pair, for $\mu^+\mu^-$ pair, and for $\tau^+\tau^-$ pair. The reconstruction of the invariant mass of $\tau^+\tau^-$ pair is based on hadronically decaying taus (for recent analyses see [93]).

Chapter 8

Event Counting Signatures for Sparticles at the LHC

8.1 Discrimination among mSPs in mSUGRA

We turn now to a discussion of how one may distinguish among different patterns. The analysis begins by considering the 902 model points that survive our mSUGRA scan with 10^6 trial points, and simulating their LHC signals with PGS4 using, for illustration, 10 fb^{-1} of integrated luminosity at the LHC. In our analysis we will focus mostly on the counting signatures. Here the most useful counting signature is the total number of SUSY events after trigger level cuts and post trigger level cuts are imposed. All other counting signatures are normalized with respect to the total number of SUSY events passing the cuts and thus appear as fractions lying between (0,1) in our figures. To keep the analysis statistically significant, we admit only those points in the parameter space that generate at least 500 total SUSY events.

We give now the details of the analysis. In Fig.(8.1), we investigate the signature space spanned by a variety of signature channels. Top Left: An exhibition of the

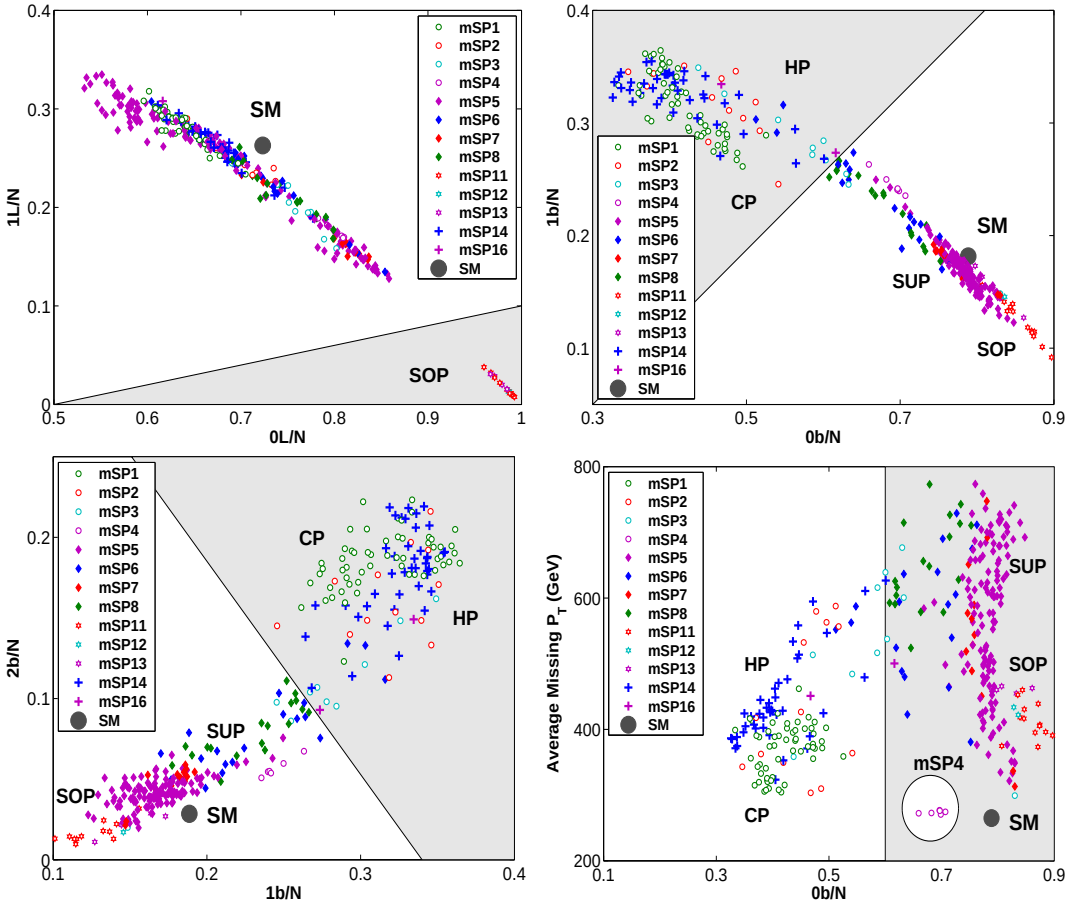

Figure 8.1: Exhibitions of the mSPs in mSUGRA with $\mu > 0$ in various signature channels.

mSPs in the 1L vs 0L where the fraction of events to the total number of events in each case is plotted. The analysis shows that the Stop Patterns (SOP) appearing on the right-bottom corner are easily distinguished from other patterns. The analysis shows that SOP has few lepton signals. Top Right and Bottom Left: Plots in the signature space with fraction of events with 1b vs 0b and 2b vs 1b exhibiting the separation of CPs and HPs from SOPs and SUPs, with CPs and HPs occupying one region, and SOPs and SUPs occupy another in this signature space except for a very small overlap. Bottom Right: An exhibition of the mSPs in the signature space with the average missing P_T for each parameter point in the mSUGRA parameter space

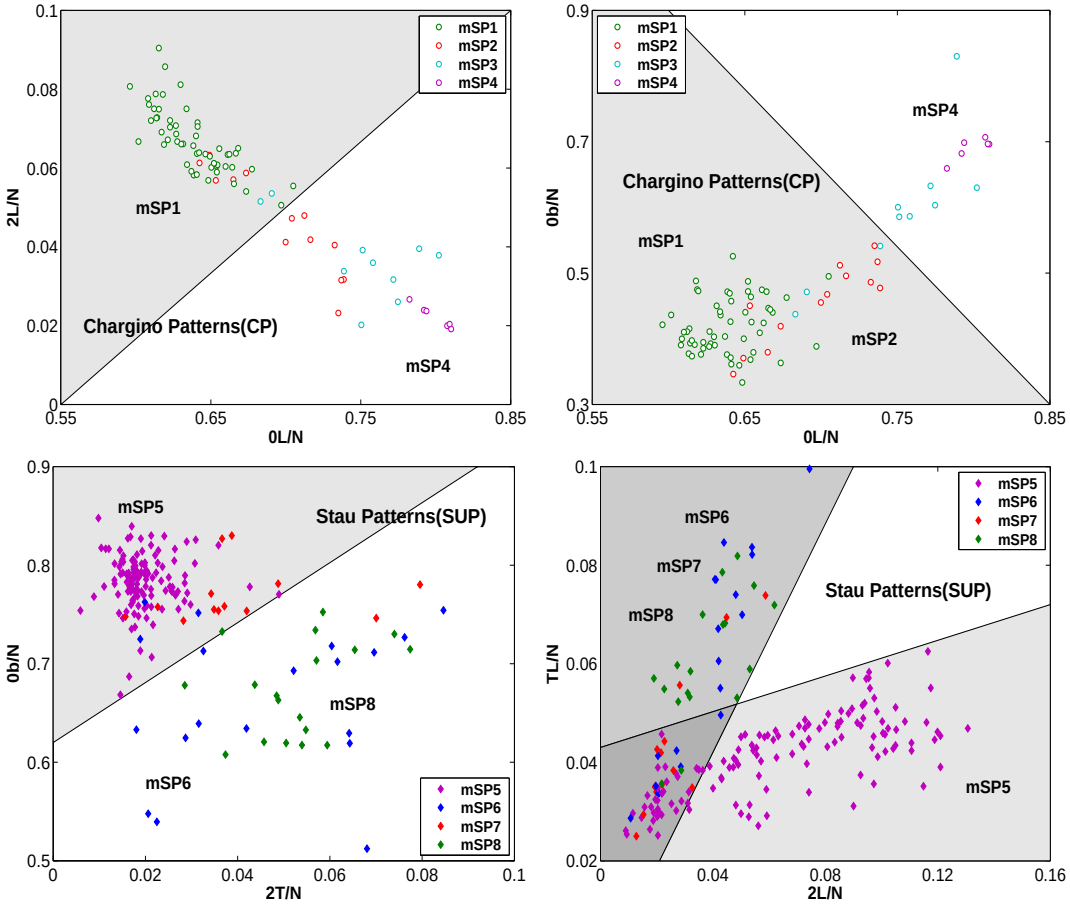

Figure 8.2: An exhibition of how the mSPs can be discriminated within CPs, SUPs.

along the y-axis and the fraction of events with $0b$ along the x-axis. The plot shows a separation of the CPs and HPs from SOPs and SUPs. Further, mSP4 appears isolated in this plot. Most of the CPs and HPs have less than 60% events without b-jet content. The ratios for the SUSY models refer to the SUSY signal only. The SM point is purely background. The top left panel gives a plot with one signature consisting of events with one lepton and the second signature consisting of event with no leptons. It is seen that the stop patterns (SOPs) that survive the cuts are confined in a small region at the right-bottom corner and have a significant separation from all other mSPs. The panel illustrates the negligible leptonic content in stop decays. The top-right panel is a plot between two signatures where one signature contains a

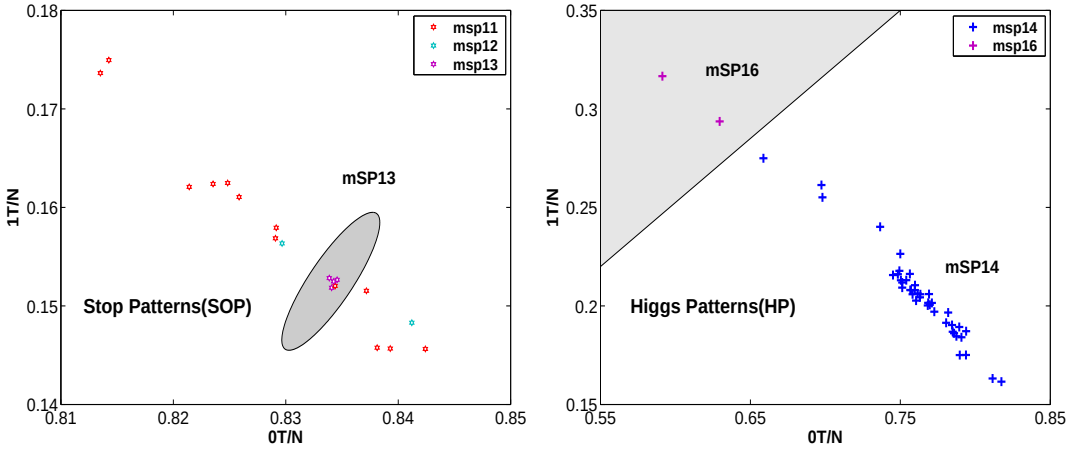

Figure 8.3: An exhibition of how the mSPs can be discriminated within SOPs and HPs.

tagged b-jet while the other signature has no tagged b-jets. In this case one finds a significant separation of the CPs and HPs from SUPs and SOPs. The lower-left panel gives a plot where one signature has two tagged b-jets and the other signature has only one tagged b-jet. One again finds that the CPs and HPs are well separated from the SOPs and the SUPs for much the same reason as in upper-right panel. Finally, a plot is given in the lower-right panel where one signature is the average missing P_T while the other signature involves events with no tagged b-jets. Again in this plot the CPs (which include mSP4) and HPs are well separated from the SOPs and SUPs.

The analysis of Fig.(8.1) exhibits that for some cases, e.g., for the patterns CP and HP in the upper right hand corner of Fig.(8.1), the separation between the SUGRA prediction and the Standard Model background is strikingly clear, allowing for the identification not only of new physics but also of the nature of the pattern that leads to such a signature.

We discuss now the possibility of discriminating sub-patterns within a given pattern class. An analysis illustrating this possibility is given in Fig. (8.2). Here the top two panels illustrate how the sub-patterns mSP1, mSP2, mSP4 within the chargino

class (CP) are distinguishable with appropriate choice of the signatures. A similar analysis regarding the discrimination for the sub-patterns in the stau class (SUP) is given in the two bottom panels. The left panel in Fig. (8.3) gives an analysis of how one may discriminate the stop sub-patterns mSP11, mSP12, mSP13 in the stop class (SOP), and finally the right panel shows the plots that allows one to discriminate the Higgs patterns mSP14 and mSP16 from each other. There are a variety of other plots which allow one to discriminate among patterns. With 40 counting signatures one can have 780 such plots and it is not possible to display all of them. A global analysis where the signatures are simultaneously considered for a large collection of mSPs and NUSPs.

As mentioned in the above analysis we have included models which can produce at least 500 SUSY events with 10 fb^{-1} which is lower than our estimated discovery limits for total SUSY events which are about 2200 in this case. The reason for inclusion of points below the discovery limit in the total SUSY events is that some of them can be detected in other channels such as in the trileptonic channel while others will be detectable as the luminosity goes higher. We note in passing that reduction of admissible points makes separation of patterns easier.

8.2 Sparticle Signatures including Nonuniversalities

In this section, we give an analysis including nonuniversalities in three different sectors: NUH, NU3, and NUG. In our analysis we simulate various models with the same constant number of events N which we take, as an example to be N= 10^4. To discriminate among the patterns in the signature space, we introduce another set of post trigger cuts, which we denote as 'b jet cuts', in addition to the default post trigger

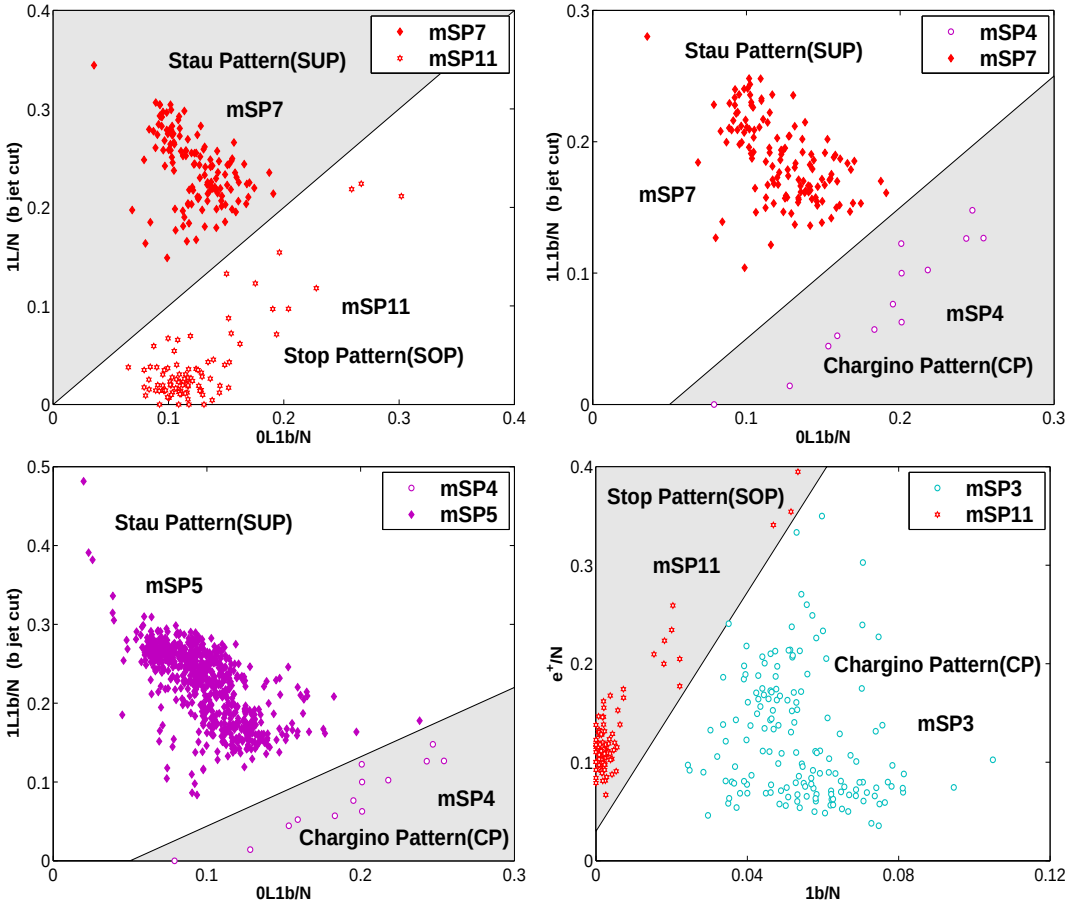

Figure 8.4: Discrimination among mSPs within both mSUGRA and NUSUGRA models.

cuts specified in previous chapter. The criteria in the b-jet cuts are the same as the default post trigger cuts, except that we change the condition 'at least two hadronic jets in the event' to 'specifically at least one b-tagged jet in the event'. We exhibit our analysis utilizing both the default cuts and the b jet cuts in Fig.(8.4). Two mSPs are presented in each figure in different signature spaces to show the separation for each case. Signals are simulated with constant number of events in PGS4 for each pattern. One can see that even with inclusion of a variety of soft breaking scenarios, some mSPs still have very distinct signatures in some specific channels.

Thus in the top-left panel of Fig. (8.4) we give a plot of mSP7 (SUP) and mSP11

(SOP) in the signature space 1L/N (b jet cuts) vs 0L1b/N, where 0L1b/N is obtained with the default post trigger cuts. Here we find that these two model types are clearly distinguishable as highlighted by shaded and unshaded regions. A similar analysis with signatures consisting of 1L1b/N (b jet cuts) vs 0L1b/N for mSP4 (CP) and mSP7 (SUP) is given in the top-right panel. The lower-left panel gives an analysis of mSP4 (CP) and mSP5 (SUP) also in the signature space consisting of 1L1b/N (b jet cuts) vs 0L1b/N. Finally, in the lower-right panel we give an analysis of mSP3 (CP) and mSP11 (SOP) in the signature plane e^+/N vs 1b/N. These analyses illustrate that the patterns and often even the sub-patterns can be discriminated with the appropriate choice of signatures for a general class of SUGRA models including nonuniversalities .

8.3 The Trileptonic Signal as a Pattern Discriminant

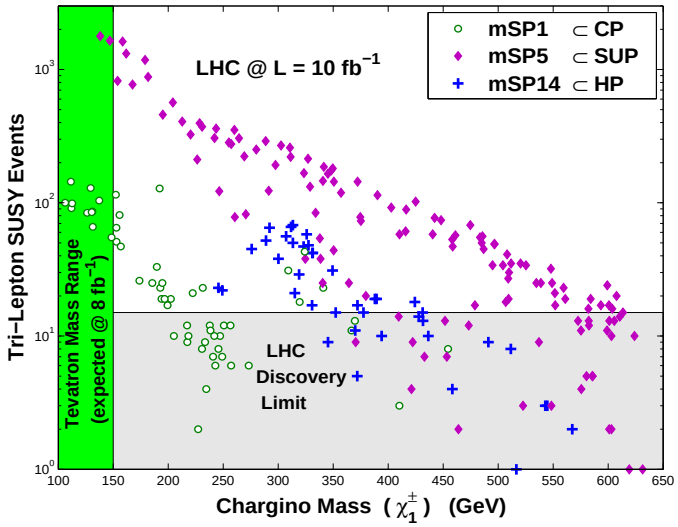

Figure 8.5: A plot of the number of trilepton events versus the light chargino mass for three patterns, one from each class, CP, SUP and HP. The SUP pattern gives the largest trileptonic signal followed by the HP and CP patterns.

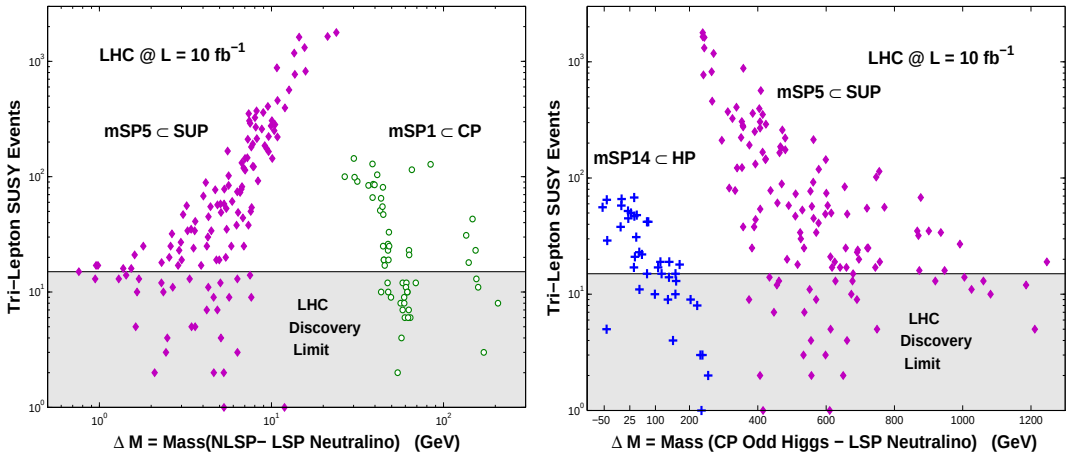

Figure 8.6: The number of tri-lepton events versus the sparticle mass splittings.

The trileptonic signal is an important signal for the discovery of supersymmetry. For on-shell decays the trileptonic signal was discussed in the early days in [18, 125] and for off-shell decays in [126]. (For a recent application see [118]). Here we discuss the trileptonic signal in the context of discrimination of hierarchical patterns. In Fig. (8.5) we exhibit the dependency of the trilepton signal on the chargino mass. It is seen that mSP5 gives the largest number of events in this channel while the CP pattern (mSP1) and the HP pattern (mSP14) can also produce a large number of trilepton events above the discovery limit, while the chargino mass reach is extended for the mSP5 as opposed to the mSP1 and mSP14. The above observations hold for some of the other SUP patterns as well. Thus the trileptonic signal is strong enough to be probed up to chargino masses of about 500 GeV in the SUP pattern. Another interesting display of the trileptonic signal is when this signal is plotted against some relevant mass splittings. The left panel of Fig. (8.6) shows clear separations for hierarchical mass patterns in the number of trilepton events produced with 10 fb^{-1} as a function of the NLSP and the LSP mass splitting for the chargino (CP) pattern mSP1 and Stau (SUP) mSP5. The plot on the right shows a similar effect for the

case where the mass splitting is taken to be the difference of the CP odd Higgs boson mass and the LSP for both the Higgs pattern mSP14 and the stau pattern mSP5. The Standard Model background is highly suppressed in this channel. Thus the left-panel of Fig. (8.6) gives an analysis for the trileptonic signal for two patterns: the Chargino pattern mSP1 and the Stau pattern mSP5 plotted against the NLSP-LSP mass splitting with 10 fb^{-1} of data.

The analysis of the left-panel of Fig. (8.6) shows that the SUP pattern presents an excellent opportunity for discovering SUSY through the 3 lepton mode. The analysis also shows a clear separation among mass patterns and further a majority of the model points stand above the discovery limit which in this channel is ≈ 15 events under the post trigger level cuts discussed previously. The right-panel of Fig. (8.6) gives an analysis of the trileptonic signal vs the mass splitting of the CP odd Higgs and the lightest neutralino LSP for patterns mSP5 and mSP14. Again, we see a clear separation of model points. We note that CP odd Higgs can sometimes be even lighter than the LSP, and thus the quantity $\Delta M = M_A - M_{\tilde{\chi}_1^0}$ plotted on the x-axis can sometimes become negative.

Chapter 9

Kinematic Signatures of Sparticles at the LHC

In this chapter, we discuss various kinematical variables that are useful for pattern discrimination. Usually, the kinematic distributions require much higher luminosity than the counting signatures, so it is unlikely that SUSY is first discovered with kinematical distributions. But the kinematic distributions carry more precise information which is essential for determining the detailed structure of SUSY models.

Typically, there are two types of kinematic distributions, P_T distributions and invariant mass distributions. The P_T distributions we investigate include missing P_T distribution and the effective mass distributions. The invariant mass distribution analyzed here is the opposite sign same flavor dilepton invariant mass distribution.

9.1 Transverse Momentum Distributions

The kinematical signatures are important for pattern discrimination in addition to the event counting signatures discussed previously. We illustrate this using the kine-

matical variables consisting of missing P_T and the effective mass (see Table (7.1) for their definitions) and an illustration is given in Fig.(9.1). Specifically the analysis of

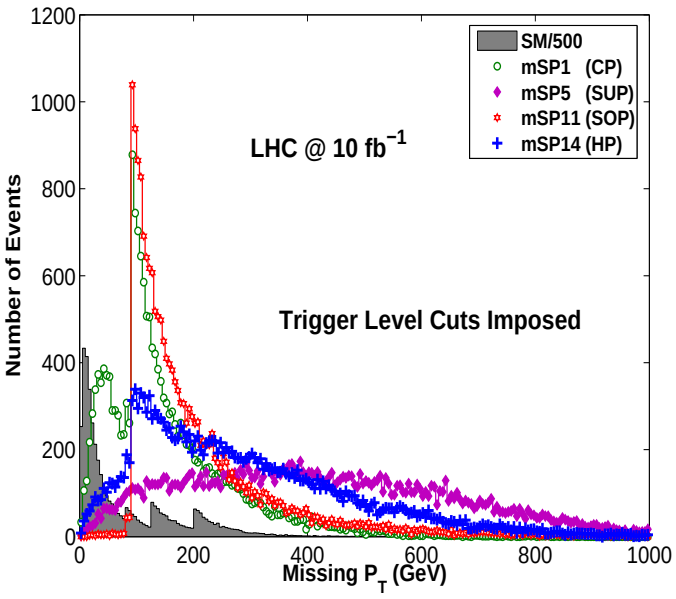

Figure 9.1: An exhibition of the missing P_T distributions for 4 different mSUGRA models with each corresponding to one class of mSPs, and for the Standard Model. Only trigger level cuts are employed here.

Fig.(9.1) uses four mSUGRA points one each in the patterns CP, SUP, SOP and HP. We exhibit the mSUGRA points used here in the order (m_0, $m_{1/2}$, A_0, $\tan\beta$, signμ):

$$\begin{aligned}
&\text{CP} \quad \text{Point} \quad (3206.9,\ \ 285.3,\ \ -1319.8,\ \ 9.7,\ \ +1),\\
&\text{SUP} \quad \text{Point} \quad (92.6,\ \ 462.1,\ \ 352.2,\ \ 4.5,\ \ +1),\\
&\text{SOP} \quad \text{Point} \quad (2296.9,\ \ 625.0,\ \ -5254.9,\ \ 13.6,\ \ +1),\\
&\text{HP} \quad \text{Point} \quad (756.8,\ \ 387.0,\ \ 1144.9,\ \ 56.5,\ \ +1).
\end{aligned} \tag{9.1}$$

In the missing P_T distribution the Standard Model tends to produce events with a lower missing P_T relative to the mSUGRA case which generates events at relatively higher missing P_T. Further, there is a large variation between different mSUGRA

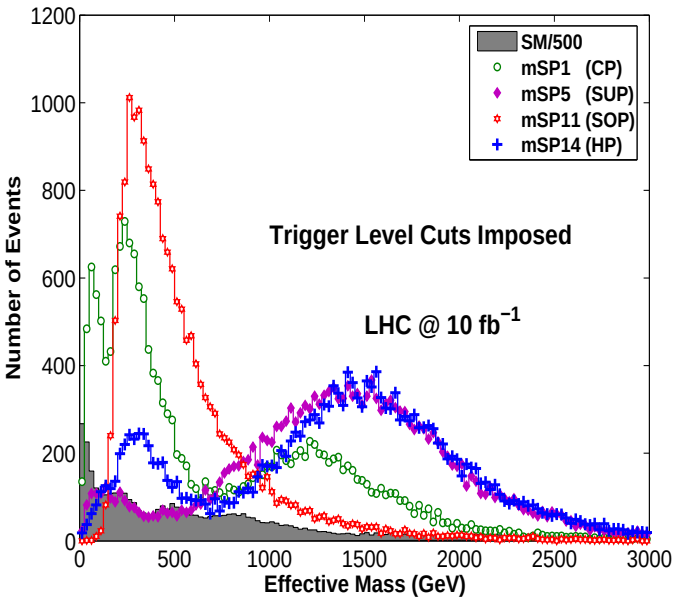

Figure 9.2: An exhibition of the effective mass distributions for the same mSUGRA models as shown in Fig. (9.1). Only trigger level cuts are employed here.

models, as can be seen in Fig. (9.1). Thus, for example mSP5 (a stau pattern) and mSP14 (a Higgs pattern) have peaks at larger values of missing P_T relative to mSP1 (a chargino pattern) and mSP11 (a stop pattern). Additionally, the shapes of the distributions are also different.

The analysis of effective mass distribution in Fig. (9.2) is carried out with the same mSUGRA model points as in Fig. (9.1). And it is found that in the effective mass distribution, the Standard Model tends to produce events with a lower effective mass relative to the mSUGRA models, and the variation between mSUGRA models remain similar to the case as in Fig. (9.1).

The analysis of Fig. (9.1) and Fig. (9.2) shows that the distributions for the CP, HP, SOP and SUP are substantially different. It is interesting to note that in the missing P_T distribution, the HP and SUP model points have a relatively flat distribution compared to the CP and SOP model points. The missing P_T distribution

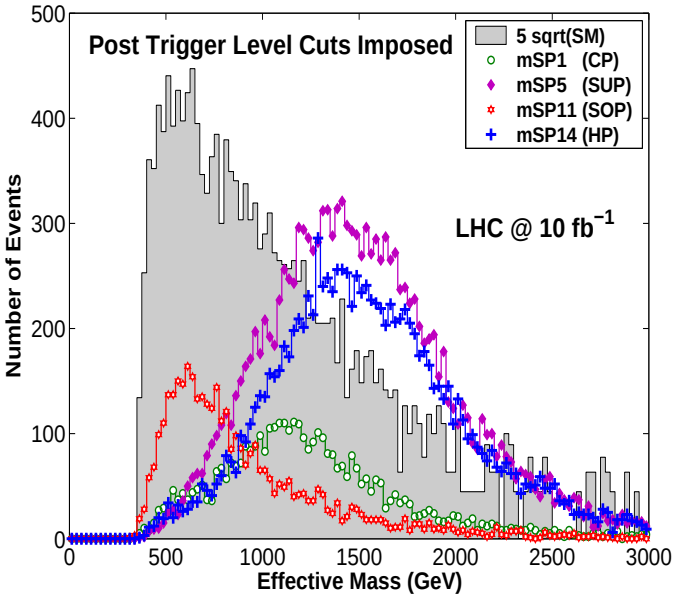

Figure 9.3: The effective mass distributions for 4 different mSUGRA models with each corresponding to one class of mSPs, and for the Standard Model. Post trigger level cuts are imposed here. The bin size used here is 25 GeV.

and the effective mass distribution are useful when designing post trigger level cuts to optimize the signal over the background. For instance, one can take a 1 TeV effective mass cut to analyze the SUP and HP signals shown in Fig.(9.2), but this method will not work well when it comes to the CP and SOP points since most of their events have a rather small effective mass. To illustrate that different models have different effective mass distributions, and consequently different effective mass cuts are needed for different patterns, an analysis is given in Fig.(9.3) for the same set of points in Fig.(9.2) with post trigger level cuts imposed.

9.2 Invariant Mass Distributions

We also investigate the invariant mass distribution for the opposite sign same flavor (OSSF) di-leptons ($e^+e^-, \mu^+\mu^-$) in Fig.(9.4). We applied the default post trigger

cuts as discussed previously to suppress the SM background. As a comparison the dominant Standard Model $t\bar{t}$ background is also exhibited. We have cross checked our work with the CMS Note [116], and found good agreement regarding the SUSY signals and the Standard Model background. It is seen that the two mSP points,

$$\begin{aligned} &\text{mSP4 Point} \quad (1674.9,\ 137.6,\ 1986.5,\ 18.6,\ +1), \\ &\text{mSP5 Point} \quad (84.4,\ 429.3,\ -263,\ 3.4,\ +1), \end{aligned} \tag{9.2}$$

plotted in Fig. (9.4) are clearly distinguishable from each other in the distribution. An analysis of invariant mass distribution is given in the Appendix. Here, we apply

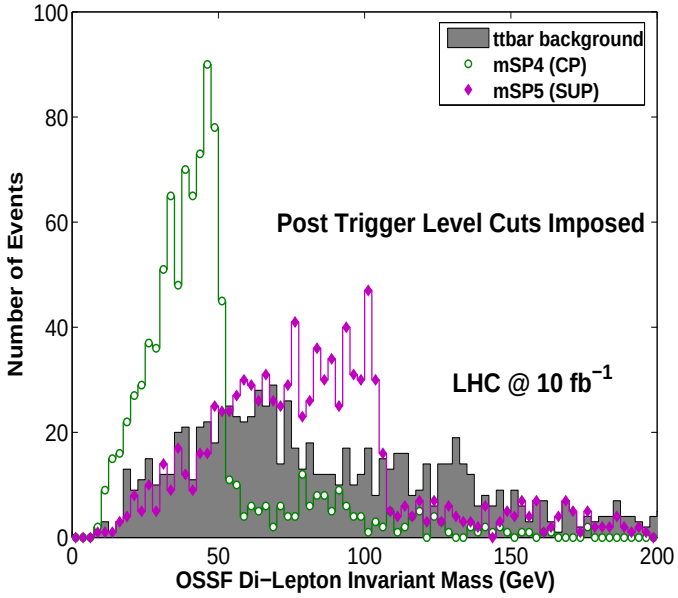

Figure 9.4: A plot of the opposite sign same flavor (OSSF) di-lepton invariant mass distribution at LHC with 10 fb^{-1} with the default post trigger cuts imposed for two different mSP points on top of the SM $t\bar{t}$ background.

the general formula given in the Appendix to one specific interesting SUSY decay

chains $\widetilde{\chi}_2^0 \to \ell^{\pm}\widetilde{\ell}^{\pm} \to \ell^{\pm}\ell^{\mp}\widetilde{\chi}_1^0$

$$M_{\ell\ell}^{\max} = M_{\widetilde{\chi}_2^0}\sqrt{1-\frac{M_{\widetilde{\ell}}^2}{M_{\widetilde{\chi}_2^0}^2}}\sqrt{1-\frac{M_{\widetilde{\chi}_1^0}^2}{M_{\widetilde{\ell}}^2}}. \tag{9.3}$$

For mSP5 model point plotted here, the relevant branching ratios are

$$BR(\widetilde{\chi}_2^0 \to \widetilde{\ell} + \ell) \simeq 23.5\% \quad \text{and} \quad BR(\widetilde{\ell} \to \widetilde{\chi}_1^0 + \ell) \simeq 100\% \tag{9.4}$$

where $\widetilde{\ell}$ are $\widetilde{e}_L$ and $\widetilde{\mu}_L$, and ℓ are electron and muon. The relevant sparticle masses are $M_{\widetilde{\ell}} = 300.9$ GeV, $M_{\widetilde{\chi}_2^0} = 327.4$ GeV, and $M_{\widetilde{\chi}_1^0} = 181.9$ GeV. Therefore, the maximum value of the invariant mass of dilepton is

$$M_{\ell\ell}^{\max} = 327.4\sqrt{1-\frac{300.9^2}{327.4^2}}\sqrt{1-\frac{181.9^2}{300.9^2}} = 102.8 \quad \text{GeV} \tag{9.5}$$

which is consistent with the result of Fig. (9.4).

For the mSP4 model point plotted here, since the sfermion masses are quite large, the SUSY production is dominated by the Ino-production, especially $\widetilde{g}$, $\widetilde{\chi}_2^0$, and $\widetilde{\chi}_1^{\pm}$. The decay mode which is responsible for most of the production of the dilepton events is

$$BR(\widetilde{\chi}_2^0 \to \widetilde{\chi}_1^0 + \ell^+ + \ell^-) = 5.66\%. \tag{9.6}$$

For this model point, the lightest neutralino masses are $M_{\widetilde{\chi}_1^0} = 54.6$ GeV and $M_{\widetilde{\chi}_2^0} = 107.4$ GeV. Here the decay process is realized through the off-shell slepton decay, since the on-shell slepton masses are above TeV. When the off-shell mass of the corresponding slepton is $m_{\text{offshell}} = \sqrt{M_{\widetilde{\chi}_2^0} M_{\widetilde{\chi}_1^0}}$, the invariant mass edge value achieves

its maximum value

$$(M_{\ell\ell}^{\max})^{\max} = M_{\widetilde{\chi}_2^0} - M_{\widetilde{\chi}_1^0} = 107.4 - 54.6 = 52.8 \quad \text{GeV} \tag{9.7}$$

which is again consistent with the result of Fig. (9.4). The off-shell mass of the

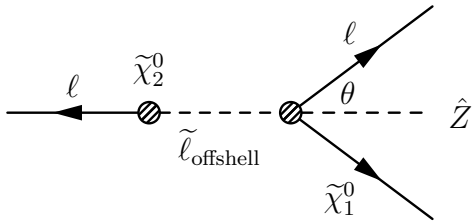

Figure 9.5: Decay process via off-shell slepton.

slepton $m = \sqrt{M_{\widetilde{\chi}_2^0} M_{\widetilde{\chi}_1^0}} = \sqrt{107.4 * 54.6} = 76.6$ GeV gives rise to the edge of the OSSF dilepton invariant mass distribution. When the off-shell slepton has an off-shell mass roughly the half way between the $\widetilde{\chi}_1^0$ and $\widetilde{\chi}_2^0$, both leptons are likely to gain enough transverse momentum in order to pass the detector cuts on lepton P_T.

The mSP4 model point shown here has recently been investigated [127] in the context of helicity amplitudes as a discovery mechanism for supersymmetry.

Chapter 10

Global Analysis of Sparticle Patterns: Fuzzy Signature Vectors

In this chapter, we discuss how one may distinguish sparticle patterns utilizing all signature channels that are available. We have given specific examples of how patterns can be differentiated from each other. In the previous analysis we used only a few of the 40 signatures exhibited in Table (7.1). Here we want to examined all of them.

Thus for each parameter point we have analyzed 40 signatures. We now define correlations among these signatures. Thus consider an ordered set where the signatures are labeled $S_1, S_2, .., S_{40}$ and let the number of events in each signature be $N_1, N_2, .., N_{40}$. Define a signature vector for a given point x_α ($\alpha = 1, 2, .., p$) in the parameter space

$$\xi^a = (\xi^a_1, \xi^a_2, .., \xi^a_{40}) \tag{10.1}$$

where $\xi_i = N^a_i/N$ and N is the total number of SUSY events. As the parameter point x_α varies over the allowed range within a given pattern it generates a signature vector where the elements trace out a given range. Thus for a pattern X one generates a

fuzzy pattern vector $\Delta\xi^X$ so that

$$\Delta\xi^X = (\Delta\xi_1^X, \Delta\xi_2^X, .., \Delta\xi_{40}^X), \tag{10.2}$$

where $\Delta\xi_i^X$ is the range traced out by the element ξ_i^X as the parameter point x_α moves in the allowed parameter space of the pattern X. What makes the vector $\Delta\xi^X$ fuzzy is that its elements are not single numbers but a set which cover a range. We define now the inner product of two such fuzzy pattern vectors so that

$$C_{XY} \equiv (\Delta\xi^X | \Delta\xi^Y) = 0(1) \tag{10.3}$$

where the inner product is 0 if the element $\Delta\xi_i^X$ and $\Delta\xi_i^Y$ overlap for all i ($i = 1, ., 40$), and 1 if at least one of the elements of pattern X, $\Delta\xi_j^X$ does not overlap with $\Delta\xi_j^Y$, the element for pattern Y. Therefore, if for two patterns X and Y one finds there is no overlap at least for one signature component $\Delta\xi_j$, then these two patterns can be distinguished in this specific signature and one obtains $C_{XY} = 1$. Otherwise $C_{XY} = 0$ which means that all components of $\Delta\xi^X$ and $\Delta\xi^Y$ have an overlap and cannot be distinguished under this criteria.

We can generalize the above procedure for the signatures

$$\zeta_{i,j} = \frac{N_i}{N_j}, \quad (i, j = 1, ..., 40). \tag{10.4}$$

Repeating the previous analysis, one can construct another fuzzy signature vector for pattern X as

$$\Delta\zeta^X = (\Delta\zeta_{1,2}^X, .., \Delta\zeta_{i,j}^X, .., \Delta\zeta_{39,40}^X) \tag{10.5}$$

where the elements have a range corresponding to the range spanned by the soft

parameters x_α as they move over the parameter space specific to the pattern. Further, the definition of the inner product Eq. (10.3) still holds for this new fuzzy signature vector. We have carried out a full signature analysis of such comparisons, using 40 different signatures, and their combinations as defined in Eq. (10.4) and Eq. (10.5).

	m5	m1	m3	m7	m11	m6	m12	m13	N1	m4	m18
m5	0	0	0	0	1	0	1	1	0	1	0
m1	0	0	0	0	0	0	1	0	0	1	0
m3	0	0	0	0	1	0	1	1	0	0	0
m7	0	0	0	0	1	0	1	1	0	1	0
m11	1	0	1	1	0	0	1	1	1	0	1
m6	0	0	0	0	0	0	1	0	0	0	0
m12	1	1	1	1	1	1	0	0	1	1	1
m13	1	0	1	1	1	0	0	0	1	1	0
N1	0	0	0	0	1	0	1	1	0	1	1
m4	1	1	0	1	0	0	1	1	1	0	1
m18	0	0	0	0	1	0	1	0	1	1	0

Table 10.1: A table exhibiting the discrimination of patterns using the criterion of Eq.(10.3) where various signatures with both the default post trigger cuts and b jet cuts are utilized. If the element of i^{th} row and j^{th} column is 1, i.e., $C_{ij} = 1$, one can distinguish the i^{th} mass pattern from the j^{th} one. Here m stands for mSP, and N for NUSP. Thus shown here is the discrimination table between the patterns: mSP5, mSP1, mSP3, mSP7, mSP11, mSP6, mSP12, mSP13, NUSP1, mSP4, mSP18. The order of the patterns indicates how often these patterns appear in our Monte Carlo scan.

An illustration of the global analysis is given in Tables (10.1, 10.2, 10.3). We carry out this analysis with a large collection of SUGRA model points which belong to 22 different hierarchical mass patterns. The complete set of the LHC signatures are obtained with the default post trigger cuts as well as the b jet cuts as specified in chapter (8). We have roughly divided the 22 sparticle patterns into two equal size sets, and classified the more probable patterns into the first set: mSP5, mSP1, mSP3, mSP7, mSP11, mSP6, mSP12, mSP13, NUSP1, mSP4, mSP18; and the less probable patterns into the second set: NUSP13, mSP20, mSP10, mSP17, NUSP3, mSP19,

NUSP5, NUSP8, NUSP10, NUSP4, NUSP9. The global analysis within these two sets is exhibited in Tables (10.1, 10.2), and the analysis between these two sets is exhibited in Tables (10.3). Altogether, Tables (10.1, 10.2, 10.3) show whether or not one can distinguish any pair of patterns chosen from the 22 different patterns utilizing the signatures investigated here.

	N13	m20	m10	m17	N3	m19	N5	N8	N10	N4	N9
N13	0	1	1	1	1	1	1	1	1	1	1
m20	1	0	1	1	1	1	1	1	1	1	1
m10	1	1	0	1	1	1	1	1	1	1	1
m17	1	1	1	0	1	1	1	1	1	1	1
N3	1	1	1	1	0	1	1	1	1	1	1
m19	1	1	1	1	1	0	1	1	1	1	1
N5	1	1	1	1	1	1	0	1	1	1	1
N8	1	1	1	1	1	1	1	0	1	1	1
N10	1	1	1	1	1	1	1	1	0	1	1
N4	1	1	1	1	1	1	1	1	1	0	1
N9	1	1	1	1	1	1	1	1	1	1	0

Table 10.2: A discrimination table between the patterns: NUSP13, mSP20, mSP10, mSP17, NUSP3, mSP19, NUSP5, NUSP8, NUSP10, NUSP4, NUSP9.

The analysis shows that it is possible to often distinguish patterns using the criterion of Eq.(10.3). We note that the analyses exhibited in Fig.(8.4) are the special cases of the results in Tables (10.1, 10.2, 10.3). For instance, the clear separation between mSP7 and mSP11 in the signature space shown in the top-left panel of Fig.(8.4) gives the elements $C_{45} = C_{54} = 1$ of Table (10.1). As indicated in Table (10.2) all the patterns analyzed here can be discriminated from each other. This is not really surprising, because the probability of finding the sparticle patterns shown in Table (10.2) are not big, and each pattern here is not analyzed with enough model points in order to gain sufficient statistics. As emphasized already the analysis of in Tables (10.1, 10.2, 10.3) is for illustrative purposes as we used a random sample of 22 patterns out of 37. Inclusion of each additional mass pattern brings in a significant set

of model points which need to be simulated, and here one is limited by computing power. The full analysis including all the patterns can be implemented along similar

	N13	m20	m10	m17	N3	m19	N5	N8	N10	N4	N9
m5	1	1	1	0	1	1	1	1	1	0	1
m1	1	1	1	0	0	1	1	1	1	0	1
m3	1	1	1	1	0	1	1	1	1	1	1
m7	1	1	1	1	0	1	1	1	1	0	1
m11	1	1	1	1	1	1	1	1	1	1	1
m6	1	1	1	0	0	1	1	1	1	0	1
m12	1	1	1	1	1	1	1	1	1	1	1
m13	1	1	1	1	1	1	1	1	1	1	1
N1	1	1	1	1	1	1	1	1	1	1	1
m4	1	1	1	1	1	1	1	1	1	1	1
m18	1	1	1	1	1	1	1	1	1	1	1

Table 10.3: A discrimination table between the two sets of patterns exhibited in the previous Tables (10.1, 10.2).

lines with the necessary computing power. Finally we note that the analysis in Tables (10.1, 10.2, 10.3) is done without statistical uncertainties. Inclusion of uncertainties in pattern analysis would certainly be worthwhile in a future work.

Chapter 11

Signature Degeneracies and Resolution of Soft Parameters

11.1 Lifting Signature Degeneracies

It may happen that two distinct points in the soft parameter space may lead to the same set of signatures for a given integrated luminosity within some predefined notion of indistinguishability. Thus consider two parameter points A and B and define the 'pulls' in each of their signatures by

$$\begin{aligned} P_i &= \frac{|n_i^A - n_i^B|}{\sigma_{AB}}, \\ \sigma_{AB} &= \sqrt{(\delta n_i^A)^2 + (\delta n_i^B)^2 + (\delta n_i^{SM})^2}. \end{aligned} \tag{11.1}$$

Here $\delta n_i^A \sim \sqrt{n_i^A}$ is the uncertainty in the signature events n_i^A, and we estimate the SM uncertainty as $\delta n_i^{SM} \sim \sqrt{y}(\delta n_i^A + \delta n_i^B)/2$. Here the parameter y parameterizes the effect of the SM events, and for the analysis in this section, we take $y = 1$. In other words, if the pull in each of the signatures is less than 5, then the two SUGRA

parameter space points are essentially indistinguishable in the signature space. In such a situation one could still distinguish model points either by including more signatures, or by an increase in luminosity. Thus, for example, inclusion of the Higgs production cross sections, $B_s \to \mu^+\mu^-$ constraints, as well as the inclusion of neutralino proton scattering cross section constraints tend to discriminate among the model parameter points as shown in Ref. [23]. Here we point out that in some cases increasing the luminosity can allow one to lift the degeneracies enhancing a subset of signatures in one case relative to the other. For illustration we consider the following two sets of points in the pattern mSP5 in the mSUGRA parameter space in the following order (m_0, $m_{1/2}$, A_0, $\tan\beta$, signμ).

$$\begin{aligned} &\text{Point A} \quad (192.6, 771.3,\ 1791.1, 8.8, +1), \\ &\text{Point B} \quad (163.0, 761.3, -775.8, 4.7, +1); \end{aligned} \tag{11.2}$$

$$\begin{aligned} &\text{Point A}' \quad (159.3, 732.3, -783.1, 5.6, +1), \\ &\text{Point B}' \quad (163.5, 753.3, -918.2, 3.3, +1). \end{aligned} \tag{11.3}$$

In Table(11.1) we compare the pulls for the pairs of points (A, B) and (A', B') at an integrated luminosity of 10 fb^{-1} and 500 fb^{-1}. For points A and B, one finds that the pulls are all less than 2 for an integrated luminosity of 10 fb^{-1}. However, for an integrated luminosity of 500 fb^{-1}, the pulls for signatures $(5, 7, 8, 34, 39)$ increase significantly and the pull for signature number 34 is in excess of 5 allowing one to discriminate between the two parameter points A and B. A very similar analysis is carried out for parameter points A' and B'. Here one finds that the signature $(0, 1, 2, 3, 6, 12, 14, 32, 33, 36)$ receive a big boost as we go from 10 fb^{-1} to 500 fb^{-1}, and the signatures $(0, 1, 2, 6, 36)$ give pulls greater than 5, with the largest pulls being in excess of 12, allowing one to discriminate between the parameter points A' and

B'. We note the analysis ignores systematic errors and also does not consider an ensemble of simulations. Nonetheless it does illustrate the effects of moving from a low to a high LHC luminosity allowing one to discriminate some model pairs, which appear degenerate in the signature space at one luminosity, but can become distinct from each other at a larger luminosity.

11.2 Resolving Soft Parameters using LHC Data

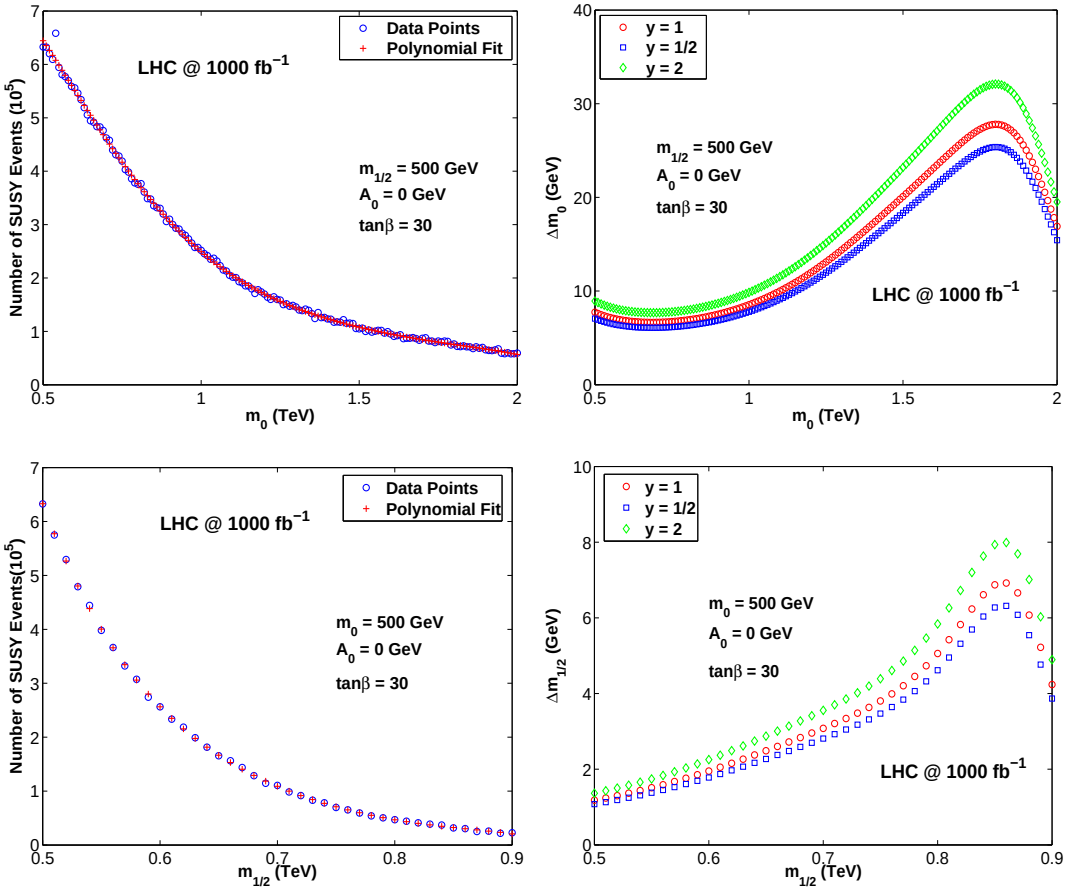

Figure 11.1: An analysis showing the resolutions in m_0 and $m_{1/2}$ that can be reached with 1000 fb^{-1} of integrated luminosity under the REWSB constraints. The two left panels give the number of SUSY events vs m_0 (top left panel) and vs $m_{1/2}$ (lower left panel) for 1000 fb^{-1} of integrated luminosity. The right panels give the resolutions in m_0 (top right panel) and in $m_{1/2}$ (lower right panel) using the left panels.

We discuss now the issue of how well we can resolve the points in the parameter space x_α ($\alpha = 1, .., p$) for a given luminosity. Consider Eq.(11.1) and set $\delta N = \sqrt{N}$, and parameterize the standard model uncertainty by $\delta N^{SM} = \sqrt{y}\delta N$. Next we set the criterion for the resolution of two adjacent points in the SUGRA parameter space separated by Δx_α so that the separation in the signature space satisfies

$$\frac{\Delta N}{\sqrt{2N + yN}} = 5. \tag{11.4}$$

Since $N = \sigma_{\rm susy}(x_\alpha)\mathcal{L}_{\rm LHC}$, where $\sigma_{\rm susy}$ is the cross section for the production of sparticles, and $\mathcal{L}_{\rm LHC}$ is the LHC integrated luminosity, the resolution achievable in the vicinity of SUGRA parameter point x_α at that luminosity is given by

$$\Delta x_\alpha = \frac{5}{2}(2+y)^{1/2}\mathcal{L}_{\rm LHC}^{-1/2}\left(\frac{\partial\sigma_{\rm susy}^{1/2}(x)}{\partial x_\alpha}\right)^{-1}. \tag{11.5}$$

In Fig.(11.1) we give an illustration of the above when m_0 varies between 500 GeV and 2000 GeV while $m_{1/2} = 500$ GeV, $A_0 = 0, \tan\beta = 30$, and $\mu > 0$. From Fig.(11.1) one finds that the resolution in m_0 strongly depends on the point in the parameter space and on the luminosity. Quite interestingly a resolution as small as a few GeV can be achieved for m_0 in the range 500-1000 GeV with 1000 fb^{-1} of integrated luminosity. A similar analysis varying $m_{1/2}$ in the range 500$\sim$900 GeV for the case when $m_0 = 500$ GeV, $A_0 = 0, \tan\beta = 30$ and $\mu > 0$, shows that a resolution in $m_{1/2}$ as low as 1 GeV can be achieved with 1000 fb^{-1} of integrated luminosity.

i	S_i	A	B	P_i	A'	B'	P_i	A	B	P_i	A'	B'	P_i
0	N	743	730	0.3	878	817	1.2	35770	35570	0.6	45479	41135	12.1
1	0L	430	414	0.4	484	437	1.3	20645	20490	0.6	25897	23427	9.1
2	1L	221	230	0.3	294	271	0.8	10565	10410	0.9	13669	12414	6.3
3	2L	78	71	0.5	83	96	0.8	3740	3945	1.9	4904	4369	4.5
4	3L	10	13	0.5	16	11	0.8	725	675	1.1	927	830	1.9
5	4L	4	2	0.6	1	2	0.4	95	50	3.1	82	95	0.8
6	0T	620	610	0.2	731	674	1.2	29325	29860	1.8	38213	34138	12.4
7	1T	112	104	0.4	137	129	0.4	5710	5125	4.6	6528	6296	1.7
8	2T	11	14	0.5	10	14	0.7	685	540	3.4	693	659	0.8
9	3T	0	2	1.1	0	0	0.0	45	40	0.4	43	40	0.3
10	4T	0	0	0.0	0	0	0.0	5	5	0.0	2	2	0.0
11	TL	38	26	1.2	50	45	0.4	1730	1595	1.9	2069	2029	0.5
12	OS	59	57	0.2	66	70	0.3	2785	2910	1.4	3665	3285	3.7
13	SS	19	14	0.7	17	26	1.1	955	1035	1.5	1239	1084	2.6
14	OSSF	40	46	0.5	49	52	0.2	2050	2140	1.1	2710	2389	3.7
15	SSSF	7	9	0.4	10	13	0.5	435	480	1.2	537	481	1.4
16	OST	7	8	0.2	5	9	0.9	420	340	2.4	428	402	0.7
17	SST	4	6	0.5	5	5	0.0	265	200	2.5	265	257	0.3
18	0L1b	50	59	0.7	61	56	0.4	2595	2695	1.1	3527	3387	1.4
19	1L1b	45	39	0.5	48	53	0.4	1905	1800	1.4	2431	2268	1.9
20	2L1b	9	8	0.2	15	21	0.8	585	660	1.7	853	778	1.5
21	0T1b	86	88	0.1	100	110	0.6	4095	4260	1.5	5734	5353	3.0
22	1T1b	21	15	0.8	22	20	0.3	1005	905	1.9	1150	1106	0.8
23	2T1b	3	3	0.0	4	2	0.6	135	95	2.2	111	129	0.9
24	0L2b	20	20	0.0	12	13	0.2	590	660	1.6	890	838	1.0
25	1L2b	11	12	0.2	15	24	1.2	425	505	2.1	625	598	0.6
26	2L2b	3	5	0.6	1	2	0.4	220	165	2.3	251	227	0.9
27	0T2b	30	29	0.1	25	32	0.8	995	1120	2.2	1481	1379	1.6
28	1T2b	4	6	0.5	4	6	0.5	245	205	1.5	300	297	0.1
29	2T2b	0	2	1.1	0	1	0.7	25	35	1.0	28	27	0.1
30	ep	71	71	0.0	93	83	0.6	3060	3010	0.5	4251	3957	2.6
31	em	47	44	0.3	52	51	0.1	2135	1955	2.3	2618	2358	3.0
32	mp	60	70	0.7	103	78	1.5	3360	3415	0.5	4236	3821	3.8
33	mm	43	45	0.2	46	59	1.0	2010	2030	0.3	2564	2278	3.4
34	tp	60	53	0.5	69	80	0.7	3255	2705	5.8	3564	3504	0.6
35	tm	52	51	0.1	68	49	1.4	2455	2420	0.4	2964	2792	1.9
36	0b	597	585	0.3	717	642	1.7	29045	28795	0.8	36432	32602	11.9
37	1b	110	107	0.2	126	132	0.3	5250	5270	0.2	7003	6593	2.9
38	2b	34	37	0.3	29	39	1.0	1265	1360	1.5	1810	1706	1.4
39	3b	1	1	0.0	6	2	1.1	195	120	3.5	215	205	0.4
40	4b	1	0	0.7	0	2	1.1	15	25	1.3	19	29	1.2

Table 11.1: An exhibition of lifting the degeneracy of two points in the mSUGRA parameter space using luminosity. Two pairs of points (A, B) and (A', B') are indistinguishable under the 2 sigma criteria at 10 fb^{-1} luminosity (column 3-8), but can be clearly separated when the luminosity increases to 500 fb^{-1} (column 9-14). The Standard Model uncertainty is estimated as $\delta n_i^{SM} = (\delta n_i^A + \delta n_i^B)/2$.

Chapter 12

Higgs Production at Colliders

In this chapter we investigate the Higgs cross sections at the Tevatron and at the LHC. The lightness of A (and also of H and $H^{\pm}$) in the Higgs Patterns implies that the Higgs production cross sections can be large (for some of the previous analyses where light Higgses appear see [128, 129, 104]).

Quite interestingly the recent Tevatron data is beginning to constrain the Higgs Patterns (HPs). This is exhibited in the left panel of Fig.(12.1) where the leading order (LO) cross section for the sum of neutral Higgs processes $\sigma_{\Phi\tau\tau}(p\bar{p}) = [\sigma(p\bar{p} \rightarrow \Phi)\mathrm{BR}(\Phi \rightarrow 2\tau)]$ (where sum over the neutral Φ fields is implied) vs the CP odd Higgs mass is plotted for CM energy of $\sqrt{s} = 1.96$ TeV at the Tevatron. One finds that the predictions of $\sigma_{\Phi\tau\tau}(p\bar{p})$ from the HPs are the largest and lie in a narrow band followed by those from the Chargino Pattern mSP2. The recent data from the Tevatron is also shown[130]. A comparison of the theory prediction with data shows that the HPs are being constrained by experiment. Exhibited in the right panel of Fig.(12.1) is $\sigma_{\Phi\tau\tau}(pp) = [\sigma(pp \rightarrow \Phi)\mathrm{BR}(\Phi \rightarrow 2\tau)]$ arising from the HPs (and also from other patterns which make a comparable contribution) vs the CP odd Higgs mass with the analysis done at CM energy of $\sqrt{s} = 14$ TeV at the LHC. Again it is

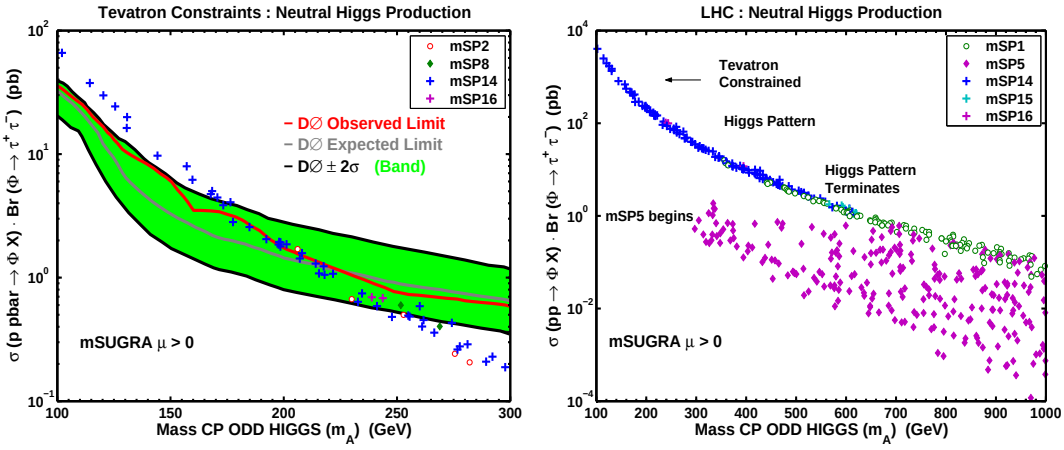

Figure 12.1: Left panel: Predictions for $[\sigma(p\bar{p} \to \Phi)\mathrm{BR}(\Phi \to 2\tau)]$ in mSUGRA as a function of the CP odd Higgs mass m_A for the HPs at the Tevatron with CM energy of $\sqrt{s} = 1.96$ TeV. The limits from DØ are indicated [130]. Right panel: Predictions for $[\sigma(pp \to \Phi)\mathrm{BR}(\Phi \to 2\tau)]$ in mSUGRA as a function of m_A at the LHC with CM energy of $\sqrt{s} = 14$ TeV for the HPs, the chargino pattern mSP1 and the stau pattern mSP5. The HPs are seen to give the largest cross sections.

seen that the predictions of $\sigma_{\Phi\tau\tau}(pp)$ arising from the HPs are the largest and lie in a very narrow band and the next largest predictions for $\sigma_{\Phi\tau\tau}(pp)$ are typically from the Chargino Patterns (CPs). The larger cross sections for the HPs enhance the prospects of their detection.

Since the largest Higgs production cross sections at the LHC arise from the Higgs Patterns and the Chargino Patterns we exhibit the mass of the light Higgs as a function of m_0 for these two patterns in the left panel of Fig.(12.2). We note that many of the Chargino Pattern points in this figure appear to have large m_0 indicating that they originate from the Hyperbolic Branch/Focus Point (HB/FP) region[45].

We discuss now briefly the Higgs to $b\bar{b}$ decay at the Tevatron. From the parameter space of mSUGRA that enters in Fig.(1) we can compute the quantity $[(p\bar{p} \to \Phi)\mathrm{BR}(\Phi \to b\bar{b})]$. Experimentally, however, this quantity is difficult to measure because there is a large background to the production from $q\bar{q}, gg \to b\bar{b}$. For

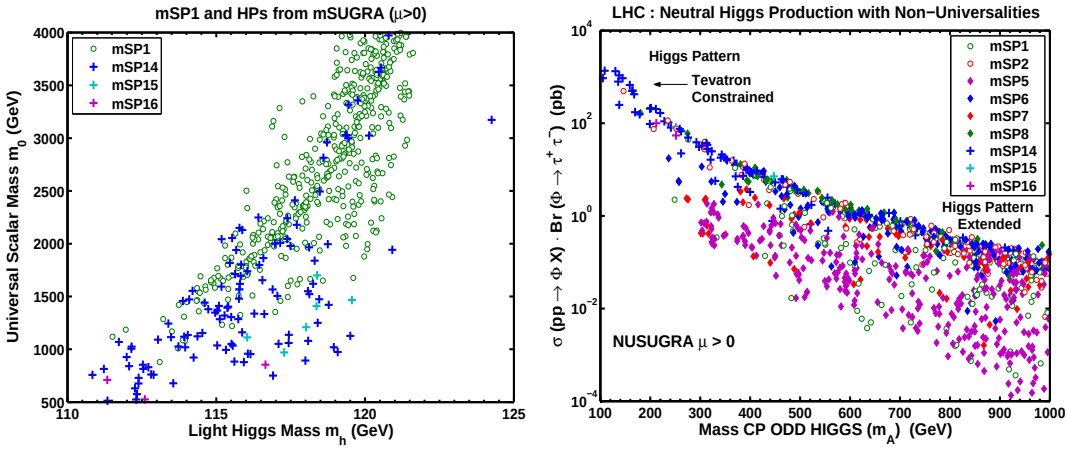

Figure 12.2: Left panel: mSP1 and HPs are plotted in the m_0-m_h plane in mSUGRA $\mu > 0$. Right panel: Predictions for $[\sigma(pp \to \Phi)\mathrm{BR}(\Phi \to 2\tau)]$ in NUSUGRA (NUH,NUG,NU3) as a function of CP odd Higgs mass at the LHC showing that the HPs extend beyond 600 GeV with non-universalities (to be compared with the analysis of Fig.(12.1) under the same naturalness assumptions).

this reason one focuses on the production $[(p\bar{p} \to \Phi b)\mathrm{BR}(\Phi \to b\bar{b})]$[131]. For the parameter space of Fig.(1) one gets $[(p\bar{p} \to \Phi b)\mathrm{BR}(\Phi \to b\bar{b})] \lesssim 1$ pb at ($\tan\beta = 55$,$M_A = 200$ GeV). The preliminary CDF data [132] puts limits at 200 GeV, in the range (5-20) pb over a 2σ band at the tail of the data set. These limits are larger, and thus less stringent, than what one gets from $\Phi \to \tau^+\tau^-$. For the LHC, we find $[(pp \to \Phi b)\mathrm{BR}(\Phi \to b\bar{b})] \sim 200$ pb for the same model point. A more detailed fit requires a full treatment which is outside the scope of the present analysis.

The neutral Higgs production cross section for the NUSUGRA case is given in the right panel of Fig.(12.2). The analysis shows that the Higgs Patterns produce the largest cross sections followed by the Chargino Patterns as in mSUGRA case. One feature which is now different is that the Higgs Patterns survive significantly beyond the CP odd Higgs mass of 600 GeV within our assumed naturalness assumptions. Thus nonuniversalities tend to extend the CP odd Higgs beyond what one has in the mSUGRA case.

Chapter 13

$B_s \to \mu^+\mu^-$ Constraints

In this chapter, we investigate the $B_s \to \mu^+\mu^-$ constraints within the context of the sparticle pattern analysis. The process $B_s \to \mu^+\mu^-$ is dominated by the neutral Higgs exchange [133]. The decay $B^0_{d'} \to \ell^+\ell^-$ (d'=d,s) is governed by the effective Hamiltonian [134]

$$H_{\rm eff} = -\frac{G_F e^2}{4\sqrt{2}\pi^2} V_{tb} V^*_{td'} (C_S O_S + C_P O_P + C'_S O'_S + C'_P O'_P + C_{10} O_{10}) \tag{13.1}$$

where

$$O_S = m_b(\bar{d}'_\alpha P_R b_\alpha)(\bar{\ell}\ell), \tag{13.2}$$

$$O_P = m_b(\bar{d}'_\alpha P_R b_\alpha)(\bar{\ell}\gamma_5\ell), \tag{13.3}$$

$$O'_S = m_{d'}(\bar{d}'_\alpha P_L b_\alpha)(\bar{\ell}\ell), \tag{13.4}$$

$$O'_P = m_{d'}(\bar{d}'_\alpha P_L b_\alpha)(\bar{\ell}\gamma_5\ell), \tag{13.5}$$

$$O_{10} = (\bar{d}'_\alpha \gamma^\mu P_L b_\alpha)(\bar{\ell}\gamma_\mu\gamma_5\ell) \tag{13.6}$$

The branching ratio $B(B^0_{d'} \to \ell^+\ell^-)$ is then given by

$$B(B^0_{d'} \to \ell^+\ell^-) = \frac{G_F^2\alpha^2 M^5_{B_{d'}}\tau_{B_{d'}}}{16\pi^3}|V_{tb}V^*_{td'}|^2\sqrt{1-\frac{4m_\ell^2}{M^2_{B_{d'}}}} \times\left[\left(1-\frac{4m_\ell^2}{M^2_{B_{d'}}}\right)|f_S|^2+|f_P+2m_\ell f_A|^2\right] \tag{13.7}$$

where f_i (i=S,P) and f_A are defined as follows

$$f_i = -\frac{i}{2}f_{B_{d'}}\left(\frac{C_i m_b - C_i' m_{d'}}{m_{d'}+m_b}\right), \tag{13.8}$$

$$f_A = -\frac{if_{B_{d'}}}{2M^2_{B_{d'}}}C_{10}. \tag{13.9}$$

Specifically C_S and C_P have the form

$$C_S = -\frac{m_\ell}{\sqrt{2}m_W^2\cos^3\beta}\sum_{j=1}^{3}\sum_{s=1}^{2} m_{\chi_s^+}\frac{R^2_{j1}}{M^2_{H_j}}\psi_s, \tag{13.10}$$

$$C_P = \frac{m_\ell\tan^2\beta}{\sqrt{2}m_W^2\cos\beta}\sum_{j=1}^{3}\sum_{s=1}^{2} m_{\chi_s^+}\frac{R^2_{j3}}{M^2_{H_j}}\psi_s. \tag{13.11}$$

When $\tan\beta$ becomes large, one finds that the branching ratio is propotional to $\tan^6\beta$.

It is thus reasonable to expect that the Higgs patterns (HPs) will be constrained more severely than other patterns by the $B_s \to \mu^+\mu^-$ experiment, since HP points usually arise from the high $\tan\beta$ region (however, as we noticed already, the nonuniversalities in the Higgs sector (NUH) can also give rise to HPs for moderate values of $\tan\beta$).

In Fig.(13.1) we carry out a detailed analysis where the branching ratio $\mathcal{B}r(B_s \to \mu^+\mu^-)$ is plotted against the CP odd Higgs mass m_A. The upper left (right) hand panel gives the analysis for the case of mSUGRA for $\mu > 0$ ($\mu < 0$) for the Higgs Patterns as well as for several other patterns, and the experimental constraints are

also shown. One finds that the constraints are very effective for $\mu > 0$ (but not for $\mu < 0$) constraining a part of the parameter space of the HPs and also some models within the Chargino and the Stau Patterns are constrained (see upper left and lower left panels of Fig.(13.1)).

From the analysis of Fig.(13.1), it is observed that the strict imposition of the constraint $\mathcal{B}r(B_s \to \mu^+\mu^-) < 1.5 \times 10^{-7}$ still allows for large $\tan\beta$ in the mSUGRA model. Thus all of the HP model points given in Fig.(13.1) that satisfy this constraint for the mSUGRA $\mu > 0$ case correspond to $\tan\beta$ in the range of 50 - 55. A similar limit on $\tan\beta$ is also observed for the nonuniversal models. We remark, however, that the HPs are not restricted to large $\tan\beta$ in particular for the case of the NUH model.

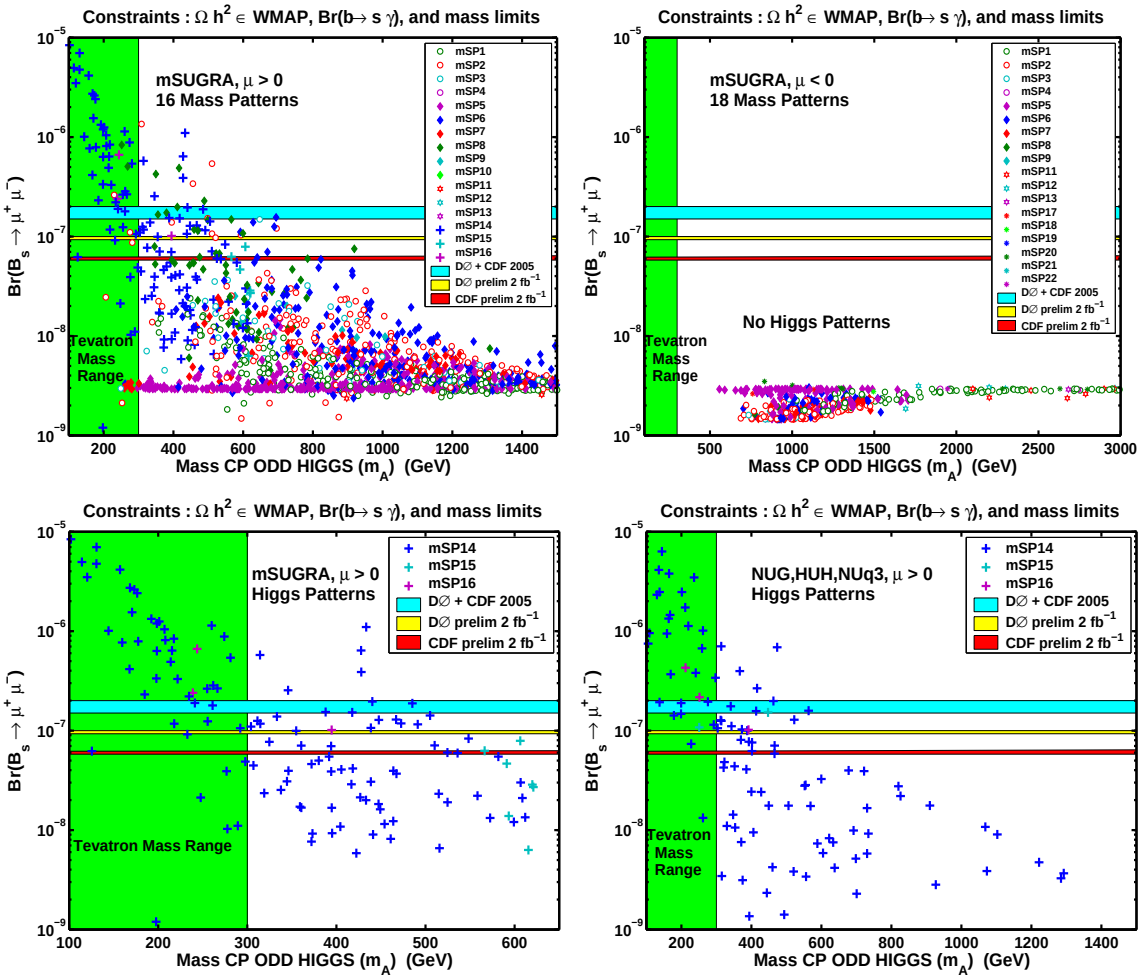

Figure 13.1: Predictions for the branching ratio $B_s \to \mu^+\mu^-$ in various patterns in the SUGRA landscape. Upper left panel: predictions are for the patterns for $\mu > 0$ in mSUGRA; upper right panel: predictions are for the patterns for $\mu < 0$ in mSUGRA; lower left panel: predictions for the Higgs Patterns alone for $\mu > 0$ in mSUGRA; lower right panel: predictions for NUSUGRA models NUH, NUq3, and NUG for $\mu > 0$. The experimental limits are: top band 2005 [135, 136], and the bottom two horizontal lines are preliminary limits from the CDF and DØ data [77]. For convenience we draw the limits extending past the observable mass of the CP odd Higgs at the Tevatron.

Chapter 14

Direct Detection of Dark Matter

14.1 mSUGRA

We discuss now the direct detection of dark matter within the framework of the mSUGRA models. In direct detection experiments one measures the cross section of the WIMP scattering off the heavy nuclei such as germanium. The neutralino interacts with quarks in the target nuclei through a Higgs boson exchange, or a squark exchange. The neutralino-nucleus scattering cross-section typically is dominated by the

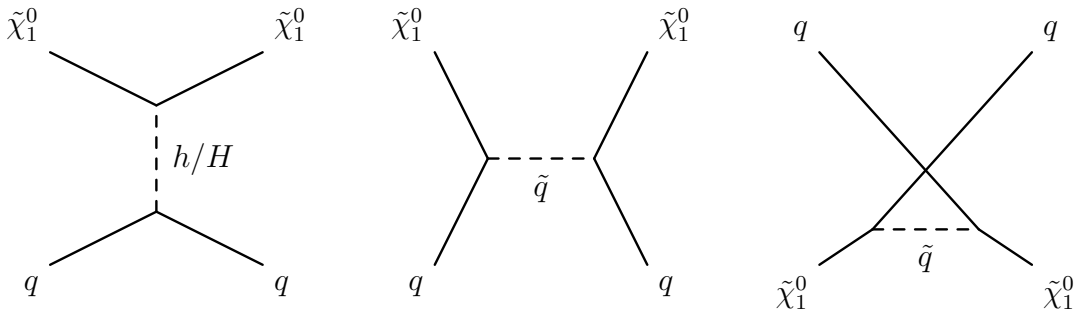

scalar part of the neutralino-quark interaction and thus it is the quantity $\sigma_{\chi p}(scalar)$ that is of interest to us. The basic interaction governing the $\chi - p$ scattering is the

effective four-fermi interaction given by (see e.g. [137])

$$\begin{aligned}\mathcal{L}_{\rm eff} = \; & \bar{\chi}\gamma_\mu\gamma_5\chi\bar{q}\gamma^\mu(AP_L + BP_R)q + C\bar{\chi}\chi m_q\bar{q}q + D\bar{\chi}\gamma_5\chi m_q\bar{q}\gamma_5 q \\ & + E\bar{\chi}i\gamma_5\chi m_q\bar{q}q + F\bar{\chi}\chi m_q\bar{q}i\gamma_5 q. \end{aligned} \tag{14.1}$$

The $\chi - p$ cross-section arising from scalar interactions $C\bar{\chi}\chi m_q\bar{q}q$ is given by

$$\sigma_{\chi p}(\text{scalar}) = \frac{4\mu_r^2}{\pi}\left[\sum_{i=u,d,s} f_i^p C_i + \frac{2}{27}\left(1 - \sum_{i=u,d,s} f_i^p\right)\sum_{a=c,b,t} C_a\right]^2. \tag{14.2}$$

Here μ_r is the reduced mass, f_i^p (i=u,d,s quarks) are defined by

$$m_p f_i^p =< p|m_{qi}\bar{q}_i q_i|p >, \tag{14.3}$$

and C is given by

$$C = C_{h^0} + C_{H^0} + C_{\tilde{f}}, \tag{14.4}$$

where C_{h^0}, C_{H^0} are the contributions from the s-channel h^0 and H^0 exchanges and $C_{\tilde{f}}$ is the contribution from the t-channel sfermion exchange. They are given by [137]

$$C_{h^0}(u,d) = -(+)\frac{g^2}{4M_W M_{h^0}^2}\frac{\cos\alpha(sin\alpha)}{\sin\beta(cos\beta)}Re\sigma, \tag{14.5}$$

$$C_{H^0}(u,d) = \frac{g^2}{4M_W M_{H^0}^2}\frac{\sin\alpha(cos\alpha)}{\sin\beta(cos\beta)}Re\rho, \tag{14.6}$$

$$C_{\tilde{f}}(u,d) = -\frac{1}{4m_q}\frac{1}{M_{\tilde{q}1}^2 - M_\chi^2}Re[C_{qL}C_{qR}^*] - \frac{1}{4m_q}\frac{1}{M_{\tilde{q}2}^2 - M_\chi^2}Re[C'_{qL}C'^*_{qR}] \tag{14.7}$$

Here (u,d) refer to the quark flavor, α is the Higgs mixing angle, and C_{qL}, C'_{qL} etc. are as defined in Ref.[137], and σ and ρ are defined by

$$\sigma = X_{40}^*(X_{20}^* - \tan\theta_W X_{10}^*)\cos\alpha + X_{30}^*(X_{20}^* - \tan\theta_W X_{10}^*)\sin\alpha, \tag{14.8}$$

$$\rho = -X^*_{40}(X^*_{20} - \tan\theta_W X^*_{10})\sin\alpha + X^*_{30}(X^*_{20} - \tan\theta_W X^*_{10})\cos\alpha, \tag{14.9}$$

where X_{n0} are the components of the LSP

$$\chi = X^*_{10}\tilde{B} + X^*_{20}\tilde{W}_3 + X^*_{30}\tilde{H}_1 + X^*_{40}\tilde{H}_2. \tag{14.10}$$

The coefficients f^p_i are associated with some amount of uncertainties [138, 129]

$$f^p_u = 0.020 \pm 0.004, \tag{14.11}$$

$$f^p_d = 0.026 \pm 0.005, \tag{14.12}$$

$$f^p_s = 0.118 \pm 0.062. \tag{14.13}$$

In the absence of CP phases, in Fig.(14.1) [23] we give an analysis of the scalar neutralino-proton cross section $\sigma(\tilde{\chi}^0_1 p)$ as a function of the LSP mass (for a sample of Post-WMAP3 analysis of dark matter see [19, 139], and for more recent analysis see [23, 140, 141, 142]). The upper left panel of Fig.(14.1) gives the scalar $\sigma(\tilde{\chi}^0_1 p)$ for the mSUGRA parameter space for $\mu > 0$. We note that the Higgs patterns typically give the largest dark matter cross sections (see the upper left and lower left panels of Fig.(14.1)) and are the first ones to be constrained by experiment. The second largest cross sections arise from the Chargino Patterns which shows an embankment, or Wall, with a copious number of points with cross sections in the range $10^{-44\pm.5}\text{cm}^2$ (see the upper left panel and lower right panel), followed by Stau Patterns (lower left panel), with the Stop Patterns producing the smallest cross sections (upper left and lower right panels). The upper right panel of Fig.(14.1) gives the scalar cross section $\sigma(\tilde{\chi}^0_1 p)$ for $\mu < 0$ and here one finds that the largest cross sections arise from the CPs which also have a Chargino Wall with cross sections in the range $10^{-44\pm.5}\text{cm}^2$ (upper right panel). The analysis shows that altogether the scalar cross sections lie

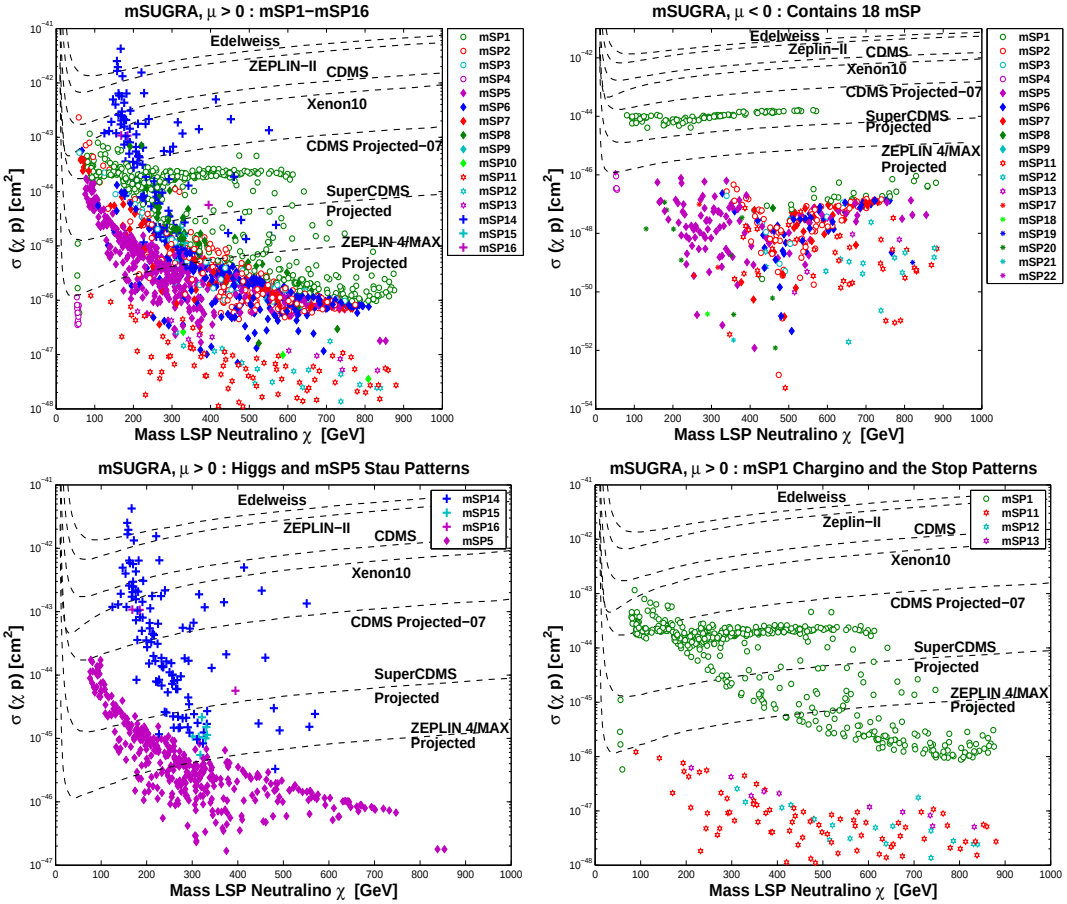

Figure 14.1: Analysis of $\sigma(\chi p)$ for mSUGRA: upper left panel: $\mu > 0$ case including all patterns; upper right panel: $\mu < 0$ allowing all patterns; lower left hand panel: A comparison of $\sigma(\chi p)$ for HPs and a stau NLSP case which is of type mSP5 for $\mu > 0$; lower right panel: a comparison of $\sigma(\chi p)$ for the Chargino Pattern mSP1 vs the Stop Patterns mSP11-mSP13. The analysis shows a Wall consisting of a clustering of points in the Chargino Patterns mSP1-mSP4 with a $\sigma(\chi p)$ in the range $10^{-44\pm.5}$ cm^2 enhancing the prospects for the observation of dark matter by SuperCDMS [143], ZEPLIN-MAX[144] or LUX[145] in this region.

in an interesting region and would be accessible to dark matter experiments currently underway and improved experiments in the future [146, 147, 148, 149, 150, 145]. Indeed the analysis of Fig.(14.1) shows that some of the parameter space of the Higgs Patterns is beginning to be constrained by the CDMS and the Xenon10 data [150].

14.2 Nonuniversalities of Soft Breaking

As already discussed in previous chapters, it is useful to consider other soft breaking scenarios beyond mSUGRA, since the nature of physics at the Planck scale is largely unknown. One such possibility is to consider nonuniveralities in the Kähler potential, which can give rise to nonuniversal soft breaking consistent with flavor changing neutral current constraints. We consider three possibilities which are nonuniversalities in (i) the Higgs sector (NUH), (ii) the third generation squark sector (NU3), and (iii) the gaugino sector (NUG) (for a sample of previous work on dark matter analyses with nonuniversalities see [151]). We parametrize these nonuniversalities as in Eq. (6.2). In each case we carry out a Monte Carlo scan of 1×10^6 models. The above covers a very wide array of models.

The analysis of the direct detection of dark matter in NUSUGRA are presented in Fig.(14.2). As in the mSUGRA case one finds that the largest dark matter cross sections still arise from the Higgs Patterns followed by the Chargino Patterns within the three types of nonuniversality models considered: NUH (upper left panel of Fig.(14.2)), NU3 (upper right panel of Fig.(14.2)), NUG (lower panel of Fig.(14.2)). Again the analysis within NUSUGRA shows the phenomenon of the Chargino Wall, i.e., the existence of a copious number of Chargino Patterns (specifically mSP1) in all cases with cross sections in the range $10^{-44\pm.5}\text{cm}^2$. Most of the parameter points along the Chargino Wall lie on the Hyperbolic Branch/Focus Point (HB/FP) region[45]

where the Higgsino components of the LSP are substantial (for a review see [46]). Thus this Chargino Wall presents an encouraging region of the parameter space where the dark matter may become observable in improved experiments.

It is seen that Higgs Patterns (HPs) arising in a wide range of models: in mSUGRA, and in NUSUGRA models are typically seen to lead to large Higgs production cross sections at the Tevatron and at the LHC. It is also seen that the HPs lead typically

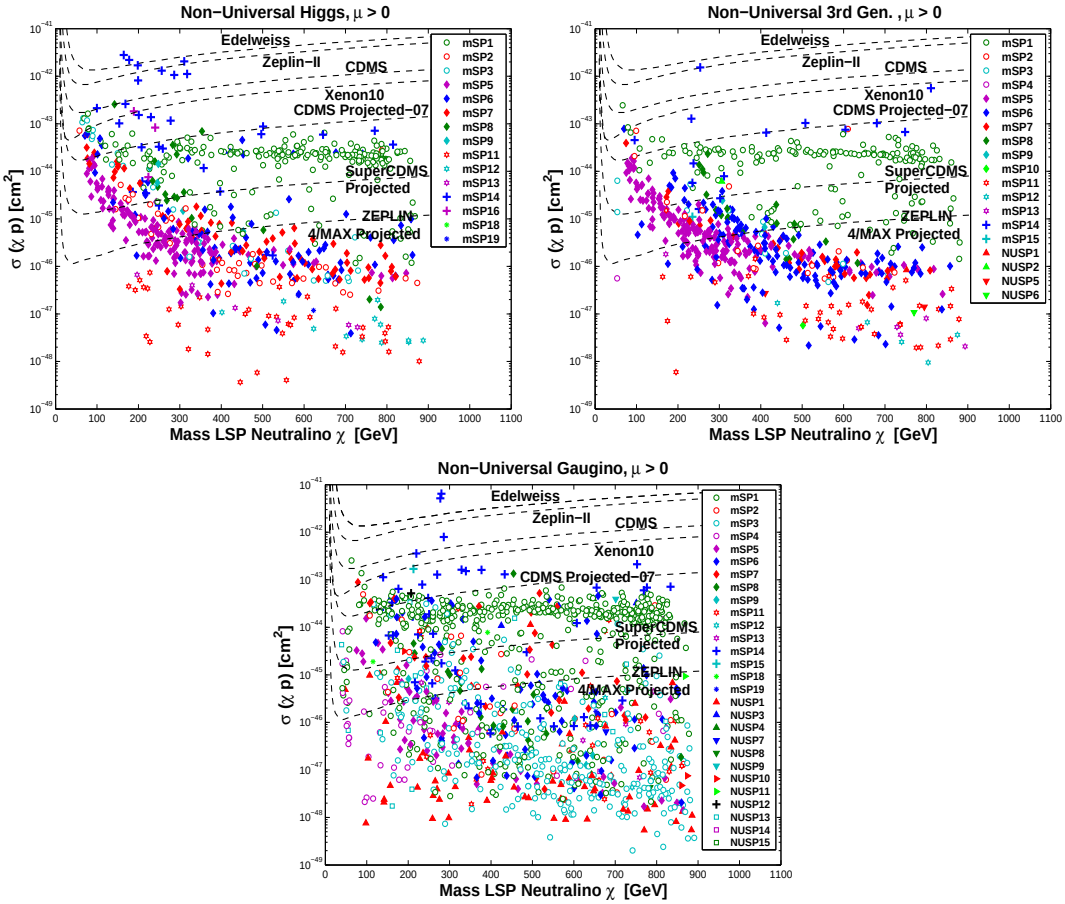

Figure 14.2: Analysis of the scalar cross section $\sigma(\chi p)$ for NUSUGRA models: NUH (upper left panel), NU3 (upper right panel), NUG (lower panel). As in Fig.(14.1) the Wall consisting of a clustering of points in the Chargino Patterns mSP1-mSP4 persists up to an LSP mass of about 900 GeV with a $\sigma(\chi p)$ in the range $10^{-44\pm.5}$ cm^2 enhancing the prospects for the observation of dark matter by SuperCDMS and ZEPLIN-MAX in this region.

to the largest neutralino-proton cross sections and would either be the first to be observed or the first to be constrained by dark matter experiment. The analysis presented here shows the existence of a Chargino Wall consisting of a copious number of parameter points in the Chargino Patterns where the NLSP is a chargino which give a $\sigma(\tilde{\chi}_1^0 p)$ at the level of $10^{-44\pm.5}\text{cm}^2$ in all models considered for the LSP mass extending up to 900 GeV in many cases. These results heighten the possibility for the observation of dark matter in improved dark matter experiments such as SuperCDMS[143], ZEPLIN-MAX[144], and LUX[145] which are expected to reach a sensitivity of 10^{-45} cm^2 or more. Finally, we note that several of the patterns are well separated in the $\sigma(\tilde{\chi}_1^0 p)$- LSP mass plots, providing important signatures along with the signatures from colliders for mapping out the sparticle parameter space.

Chapter 15

Conclusions

The minimal supersymmetric Standard Model has 32 sparticle masses. Since the soft breaking sector MSSM is arbitrary, one is led to a landscape of as many as 10^{25} or more possibilities for the sparticle mass hierarchies. The number of possibilities is drastically reduced in well motivated models such as supergravity models, and one expects similar reductions to occur also in gauge and anomaly mediated models, and in string and brane models. We have analyzed the mass hierarchies for the first four lightest sparticle (aside from the lightest Higgs boson) for supergravity models. Specifically, we analyzed the mass hierarchies for the mSUGRA model and for supergravity models with nonuniversalities in the soft breaking in the Higgs sector, nonuniversalities in the soft breaking in the third generation sector, and nonuniversalities in the soft breaking in the gaugino sector. It is found that in each case only a small number of mass hierarchies or patterns survive the rigorous constraints of radiative breaking of the electroweak symmetry, relic density constraints on cold dark matter from the WMAP data, and other experimental constraints from colliders. These mass hierarchies can be conveniently put into different classes labeled by the sparticle which is next heavier after the LSP. For the SUGRA models we find six different classes:

chargino patterns, stau patterns, stop patterns, Higgs patterns, neutralino patterns, and gluino patterns.

We discussed the techniques for the analysis of the signatures and the technical details on simulations of sparticle events. We also discuss the backgrounds to the SUSY phenomena arising from the Standard Model processes. Additionally we discussed the identification of patterns based on 40 event identification criteria. It is found that these criteria allow one to discriminate among most of the patterns. An analysis of how one may lift degeneracies in the signature space, and how accurately one can determine the soft parameters using the LHC luminosities is also given. In addition, we also investigate the Higgs production at the Tevatron and at the LHC, and the direct detection of dark matter within the context of the sparticle pattern analysis.

It is hoped that the analyses of the type discussed here would help not only in the search for supersymmetry but also allow one to use the signatures to extrapolate back to the underlying supersymmetric model using the experimental data when such data from the LHC comes in. In the above our analysis was focused on supergravity unified models. However, the techniques discussed here have a much wider applicability to other models, including models based on gauge and anomaly mediated breaking, as well as string and brane based models.

Appendix

Dilepton Invariant Mass

Here we give some further details of the analysis of the kinematic signatures discussed in chapter (9). Specifically we study the kinematics of the dilepton invariant mass of SUSY chain decays. The process we consider here has two successive decays,

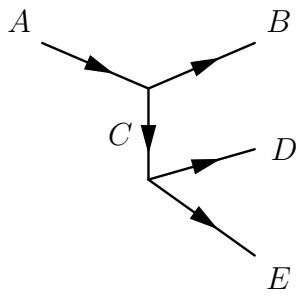

Figure 15.1: Particle A decays into particle B and C, and particle C continues to decay into particle D and E.

$A \to B + C$ followed by $C \to D + E$ as shown in Fig. (15.1). Let particles B and D be the Standard Model particles and the A, C and E be the SUSY particles. We will make the approximation that all SM particles are massless (except for the top quark).

Let us consider the decay process $A \to B+C$ in the rest frame of A. We will adopt the following notation $A \equiv m_A$, $B \equiv m_B$, and $C \equiv m_C$. Using energy-momentum conservation, one can obtain the following relations

$$P = \frac{\sqrt{A^2-(B+C)^2}\sqrt{A^2-(B-C)^2}}{2A}, \tag{15.1}$$

$$E_B = \frac{A^2+B^2-C^2}{2A}, \tag{15.2}$$

$$E_C = \frac{A^2-B^2+C^2}{2A}, \tag{15.3}$$

where $P = |\vec{P}_B| = |\vec{P}_C|$. We can do the same calculation for the second decay process $C \to D + E$ in the rest frame of C by the following substitutions $A \to C$, $B \to D$, and $C \to E$. However the calculation for these two successive decay process is carried out in two different inertial frames. Thus we introduce the following notation $(P_B^\mu)_A$ to indicate that the four vector momentum of particle B is defined in the rest frame of particle A. So we rewrite the Eqs. (15.1-15.3) for $A \to B + C$ and $C \to D + E$, and take the approximation that $B = D = 0$.

$$(P_{B,C})_A = \frac{A^2 - C^2}{2A}, \quad (E_B)_A = \frac{A^2 - C^2}{2A}, \quad (E_C)_A = \frac{A^2 + C^2}{2A}; \tag{15.4}$$

$$(P_{D,E})_C = \frac{C^2 - E^2}{2C}, \quad (E_D)_C = \frac{C^2 - E^2}{2C}, \quad (E_E)_C = \frac{C^2 + E^2}{2C}. \tag{15.5}$$

However, in order to reconstruct the invariant mass for the Standard Model particles B and D, we have to obtain the energy-momentum four-vector for both particles in the one frame. Thus one performs some Lorentz transformations to convert the energy-momentum vectors to the same frame, for instance, transforming $(P_D)_C$ to $(P_D)_A$. To do this, one has to know $(P_C^\mu)_A$ which has been done in Eq. (15.4)

$$(E_C)_A = \frac{A^2 + C^2}{2A}, \quad (P_C)_A = \frac{A^2 - C^2}{2A}. \tag{15.6}$$

And the Lorentz transformations are as follows

$$(P_D^T)_A = \sin\theta (P_D)_C, \tag{15.7}$$

$$(P_D^L)_A = (\gamma_C)_A \left[\cos\theta (P_D)_C + (\beta_C)_A (E_D)_C\right], \tag{15.8}$$

$$(E_D)_A = (\gamma_C)_A \left[(E_D)_C + \cos\theta (P_D)_C (\beta_C)_A\right], \tag{15.9}$$

where the angle θ is the angle between momentum $(\vec{P}_D)_C$ and $(\vec{P}_C)_A$ as shown in

Fig. (15.2); $\sin\theta(P_D)_C$ and $\cos\theta(P_D)_C$ are the transverse and longitudinal components of the momentum of particle D in the rest frame of particle C; and the Lorentz transformation variables γ and β are defined as

$$(\gamma_C)_A = \frac{(E_C)_A}{M_C}, \quad (\beta_C)_A = \frac{(P_C)_A}{(E_C)_A}. \tag{15.10}$$

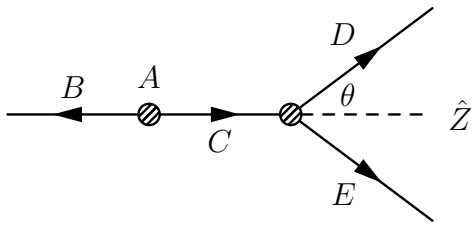

Figure 15.2: Angle θ is the angle between momentum $(\vec{P}_D)_C$ and $(\vec{P}_C)_A$. The z direction, or the longitudinal direction in the Eqs. (15.7-15.9) is along the direction of $(\vec{P}_C)_A$.

In the rest frame of particle A, the Lorentz invariant quantity, the invariant mass of the Standard Model particles B and D now can be calculated easily so that

$$M_{BD} = \sqrt{(E_B + E_D)^2 - (P_D^T)^2 - (P_D^L - P_B^L)^2} \tag{15.11}$$

where we have dropped the subscript A in Eq. (15.11) and will do so in the subsequent analysis. The Eq. (15.11) can be simplified

$$M_{BD} = A\sqrt{1 - \frac{C^2}{A^2}}\sqrt{1 - \frac{E^2}{C^2}}\sqrt{\frac{1 + \cos\theta}{2}} \tag{15.12}$$

which has a maximum value when $\cos\theta = 1$ so that

$$M_{BD}^{max} = A\sqrt{1 - \frac{C^2}{A^2}}\sqrt{1 - \frac{E^2}{C^2}}, \tag{15.13}$$

and it has a vanishing minimum when $\cos\theta = -1$. The results discussed here are utilized in the analysis given in chapter (9).

Benchmarks

Chargino Patterns (CPs)

SUGRA Pattern	m_0 (GeV)	$m_{1/2}$ (GeV)	A_0 (GeV)	$\tan\beta$ (v_u/v_d)	μ (sign)	NUH $(\delta_{H_u}, \delta_{H_d})$	NU3 $(\delta_{q3}, \delta_{tbR})$	NUG $(\delta_{M_2}, \delta_{M_3})$
mSP1	2001	411	0	30.0	+	(0,0)	(0,0)	(0,0)
mSP1	2366	338	-159	9.8	-	(0,0)	(0,0)	(0,0)
mSP1	1872	327	-1893	14.9	+	(0.107,0.643)	(0,0)	(0,0)
mSP1	1041	703	1022	11.6	+	(0,0)	(-0.524,-0.198)	(0,0)
mSP1	1361	109	1058	14.4	+	(0,0)	(0,0)	(0.929,0.850)
mSP2	1125	614	2000	50.0	+	(0,0)	(0,0)	(0,0)
mSP2	2365	1395	3663	42.2	-	(0,0)	(0,0)	(0,0)
mSP2	1365	595	3012	35.1	+	(0.116,-0.338)	(0,0)	(0,0)
mSP2	1166	507	-954	59.6	+	(0,0)	(0.325,0.458)	(0,0)
mSP2	1414	221	-551	54.3	+	(0,0)	(0,0)	(0.156,0.968)
mSP3	741	551	0	50.0	+	(0,0)	(0,0)	(0,0)
mSP3	1585	1470	3133	39.1	-	(0,0)	(0,0)	(0,0)
mSP3	694	674	-1564	27.0	+	(0.922,-0.293)	(0,0)	(0,0)
mSP3	570	559	1042	41.3	+	(0,0)	(-0.482,-0.202)	(0,0)
mSP3	392	312	320	41.3	+	(0,0)	(0,0)	(-0.404,0.908)
mSP4	1674	137	1985	18.6	+	(0,0)	(0,0)	(0,0)
mSP4	1824	127	-1828	6.4	-	(0,0)	(0,0)	(0,0)
mSP4	1021	132	-638	6.6	+	(0,0)	(-0.020,0.963)	(0,0)
mSP4	2181	127	-3859	3.9	+	(0,0)	(0,0)	(0.836,-0.248)
NUSP1	2738	1689	-4243	42.4	+	(0,0)	(-0.828,-0.899)	(0,0)
NUSP1	540	1190	2516	13.9	+	(0,0)	(0,0)	(-0.408,-0.660)
NUSP2	845	726	-75	48.4	+	(0,0)	(-0.694,-0.400)	(0,0)
NUSP3	396	1018	-179	18.3	+	(0,0)	(0,0)	(0.250,-0.452)
NUSP4	400	1558	2511	5.9	+	(0,0)	(0,0)	(-0.401,-0.607)

Table 15.1: Benchmarks for the class CP where the chargino $\widetilde{\chi}_1^{\pm}$ is the NLSP in mSUGRA and in NUSUGRA models. Benchmarks are computed with ${m_b}^{\overline{\rm MS}}(m_b) = 4.23$ GeV, ${\alpha_s}^{\overline{\rm MS}}(M_Z) = .1172$, and $m_t(\text{pole}) = 170.9$ GeV.

Stau Patterns (SUPs)

SUGRA Pattern	m_0 (GeV)	$m_{1/2}$ (GeV)	A_0 (GeV)	$\tan\beta$ (v_u/v_d)	μ (sign)	NUH $(\delta_{H_u}, \delta_{H_d})$	NU3 $(\delta_{q3}, \delta_{tbR})$	NUG $(\delta_{M_2}, \delta_{M_3})$
mSP5	111	531	0	5.0	+	(0,0)	(0,0)	(0,0)
mSP5	162	569	1012	15.8	-	(0,0)	(0,0)	(0,0)
mSP5	191	545	-722	17.2	+	(-0.340,-0.332)	(0,0)	(0,0)
mSP5	114	440	-50	15.2	+	(0,0)	(-0.204,-0.846)	(0,0)
mSP5	75	348	301	12.0	+	(0,0)	(0,0)	(0.234,-0.059)
mSP6	245	370	945	31.0	+	(0,0)	(0,0)	(0,0)
mSP6	1452	1651	2821	38.5	-	(0,0)	(0,0)	(0,0)
mSP6	356	545	927	31.7	+	(0.667,0.055)	(0,0)	(0,0)
mSP6	442	463	1150	41.0	+	(0,0)	(-0.187,-0.546)	(0,0)
mSP6	308	307	965	35.6	+	(0,0)	(0,0)	(-0.383,0.405)
mSP7	75	201	230	14.0	+	(0,0)	(0,0)	(0,0)
mSP7	781	1423	983	36.8	-	(0,0)	(0,0)	(0,0)
mSP7	428	671	484	43.8	+	(-0.392,-0.808)	(0,0)	(0,0)
mSP7	226	426	944	27.1	+	(0,0)	(0.176,-0.430)	(0,0)
mSP7	143	425	266	23.4	+	(0,0)	(0,0)	(0.718,0.100)
mSP8	1880	877	4075	54.8	+	(0,0)	(0,0)	(0,0)
mSP8	994	1073	3761	38.1	-	(0,0)	(0,0)	(0,0)
mSP8	602	684	805	49.6	+	(0.490,0.326)	(0,0)	(0,0)
mSP8	470	624	-88	55.4	+	(0,0)	(-0.531,-0.075)	(0,0)
mSP8	525	450	642	56.4	+	(0,0)	(0,0)	(0.623,0.246)
mSP9	667	1154	-125	51.0	+	(0,0)	(0,0)	(0,0)
mSP9	560	1156	-1092	39.5	-	(0,0)	(0,0)	(0,0)
mSP9	362	602	268	37.0	+	(0.969,-0.232)	(0,0)	(0,0)
mSP9	496	731	679	49.3	+	(0,0)	(-0.241,-0.452)	(0,0)
mSP9	485	478	-128	52.8	+	(0,0)	(0,0)	(0.971,0.653)
mSP10	336	772	-3074	10.8	+	(0,0)	(0,0)	(0,0)
mSP10	738	1150	-4893	15.5	+	(0,0)	(0.802,0.343)	(0,0)
mSP17	908	754	5123	25.4	-	(0,0)	(0,0)	(0,0)
mSP18	344	686	-2718	13.8	-	(0,0)	(0,0)	(0,0)
mSP18	322	806	-3069	9.3	+	(0.526,-0.707)	(0,0)	(0,0)
mSP18	60	290	-339	5.2	+	(0,0)	(0,0)	(0.967,-0.074)
mSP19	1530	1875	13081	16.3	-	(0,0)	(0,0)	(0,0)
mSP19	1828	1326	-5102	32.3	+	(0.592,-0.213)	(0,0)	(0,0)
mSP19	782	637	2688	37.9	+	(0,0)	(0,0)	(0.451,-0.551)
NUSP5	649	955	-1984	33.5	+	(0,0)	(-0.763,0.701)	(0,0)
NUSP6	1360	1736	-2871	46.1	+	(0,0)	(-0.466,0.694)	(0,0)
NUSP7	1481	1531	-3169	42.2	+	(0,0)	(0,0)	(0.117,-0.463)
NUSP8	670	1788	371	57.9	+	(0,0)	(0,0)	(-0.223,0.931)
NUSP9	46	1938	-48	13.0	+	(0,0)	(0,0)	(-0.412,-0.650)

Table 15.2: Benchmarks for the class SUP where the stau $\widetilde{\tau}_1$ is the NLSP in mSUGRA and in NUSUGRA.

Stop Patterns (SOPs)

SUGRA Pattern	m_0 (GeV)	$m_{1/2}$ (GeV)	A_0 (GeV)	$\tan\beta$ (v_u/v_d)	μ (sign)	NUH $(\delta_{H_u}, \delta_{H_d})$	NU3 $(\delta_{q3}, \delta_{tbR})$	NUG $(\delta_{M_2}, \delta_{M_3})$
mSP11	871	1031	-4355	10.0	+	(0,0)	(0,0)	(0,0)
mSP11	1653	909	7574	5.9	-	(0,0)	(0,0)	(0,0)
mSP11	1391	1089	8192	14.9	+	(0.470,0.632)	(0,0)	(0,0)
mSP11	2204	933	-1144	35.6	+	(0,0)	(0.642,-0.400)	(0,0)
mSP11	1406	1471	-2078	8.3	+	(0,0)	(0,0)	(-0.130,-0.690)
mSP12	1371	1671	-6855	10.0	+	(0,0)	(0,0)	(0,0)
mSP12	1054	1372	-5754	13.7	-	(0,0)	(0,0)	(0,0)
mSP12	915	927	-3993	20.7	+	(0.078,0.833)	(0,0)	(0,0)
mSP12	826	1016	-3926	12.8	+	(0,0)	(-0.630,-0.490)	(0,0)
mSP12	1706	1287	-4436	29.7	+	(0,0)	(0,0)	(0.416,-0.260)
mSP13	524	800	-3315	15.0	+	(0,0)	(0,0)	(0,0)
mSP13	765	1192	-4924	12.0	-	(0,0)	(0,0)	(0,0)
mSP13	1055	1601	-6365	13.6	+	(0.277,-0.820)	(0,0)	(0,0)
mSP13	1073	1664	-6528	11.6	+	(0,0)	(0.728,0.060)	(0,0)
mSP13	540	774	-2432	5.3	+	(0,0)	(0,0)	(0.705,-0.201)
mSP20	1754	840	7385	13.3	-	(0,0)	(0,0)	(0,0)
mSP21	792	845	6404	12.6	-	(0,0)	(0,0)	(0,0)
NUSP10	718	467	1657	19.0	+	(0,0)	(0,0)	(0.023,-0.810)

Table 15.3: Benchmarks for the class SOP where the stop $\widetilde{t}_1$ is the NLSP in mSUGRA and in NUSUGRA models.

Higgs Patterns (HPs)

SUGRA Pattern	m_0 (GeV)	$m_{1/2}$ (GeV)	A_0 (GeV)	$\tan\beta$ (v_u/v_d)	μ (sign)	NUH $(\delta_{H_u}, \delta_{H_d})$	NU3 $(\delta_{q3}, \delta_{tbR})$	NUG $(\delta_{M_2}, \delta_{M_3})$
mSP14	1040	560	450	53.5	+	(0,0)	(0,0)	(0,0)
mSP14	760	515	2250	31.0	+	(0.255,-0.500)	(0,0)	(0,0)
mSP14	740	620	840	53.1	+	(0,0)	(-0.530,-0.249)	(0,0)
mSP14	1205	331	-710	55.0	+	(0,0)	(0,0)	(0.380,0.250)
mSP15	1110	760	1097	51.6	+	(0,0)	(0,0)	(0,0)
mSP15	1395	554	-175	59.2	+	(0,0)	(-0.040,0.918)	(0,0)
mSP15	905	500	1460	54.8	+	(0,0)	(0,0)	(-0.350,-0.260)
mSP16	520	455	620	55.5	+	(0,0)	(0,0)	(0,0)
mSP16	282	464	67	43.2	+	(0.912,-0.529)	(0,0)	(0,0)
NUSP12	2413	454	-2490	48.0	+	(0,0)	(0,0)	(-0.285,-0.848)

Table 15.4: Benchmarks for the class HP where the Higgs boson (A, H) is the next nearest heavy particle after the LSP in mSUGRA and in NUSUGRA. The LSP and (A, H) sometimes are seen to switch.

Gluino Patterns (GPs)

SUGRA Pattern	m_0 (GeV)	$m_{1/2}$ (GeV)	A_0 (GeV)	$\tan\beta$ (v_u/v_d)	μ (sign)	NUH $(\delta_{H_u}, \delta_{H_d})$	NU3 $(\delta_{q3}, \delta_{tbR})$	NUG $(\delta_{M_2}, \delta_{M_3})$
NUSP13	2006	1081	-2027	21.1	+	(0,0)	(0,0)	(0.207,-0.844)
NUSP14	3969	1449	-6806	29.3	+	(0,0)	(0,0)	(0.611,-0.834)
NUSP15	1387	695	2781	50.5	+	(0,0)	(0,0)	(0.136,-0.827)

Table 15.5: Benchmarks for the class GP where the gluino $\widetilde{g}$ is the NLSP. Such a pattern was only seen to appear in NUSUGRA models with non universal gaugino masses. An analysis of light gluinos in the MSSM can be seen in [152].

Bibliography

[1] S. L. Glashow, "Partial Symmetries Of Weak Interactions," Nucl. Phys. **22** (1961) 579;
S. Weinberg, "A Model Of Leptons," Phys. Rev. Lett. **19** (1967) 1264;
A. Salam, in Elementary Particle Theory, ed. N. Svartholm (Almquist and Wiksells, Stockholm, 1969) p.367.

[2] D. J. Gross and F. Wilczek, "Ultraviolet Behavior Of Non-Abelian Gauge Theories," Phys. Rev. Lett. **30** (1973) 1343;
H. D. Politzer, "Reliable Perturbative Results For Strong Interactions?," Phys. Rev. Lett. **30** (1973) 1346.

[3] J. Wess and B. Zumino, Phys. Lett. B **49**, 52 (1974).

[4] P. Nath and R. Arnowitt, Phys. Lett. B **56**, 177 (1975); R. Arnowitt, P. Nath and B. Zumino, Phys. Lett. B **56**, 81 (1975); P. Nath and R. Arnowitt, Phys. Lett. B **65**, 73 (1976).

[5] D. Z. Freedman, P. van Nieuwenhuizen and S. Ferrara, Phys. Rev. D **13**, 3214 (1976); S. Deser and B. Zumino, Phys. Lett. B **62**, 335 (1976).

[6] A. H. Chamseddine, R. Arnowitt and P. Nath, Phys. Rev. Lett. **49** (1982) 970;

[7] P. Nath, R. Arnowitt and A.H. Chamseddine, Applied N=1 supergravity, Trieste Lectures, 1983(World Scientific, Singapore,1984);

[8] E. Cremmer, S. Ferrara, L. Girardello and A. Van Proeyen, Nucl. Phys. B **212**, 413 (1983); J. Bagger and E. Witten, Phys. Lett. B **118**, 103 (1982).

[9] G. F. Giudice and A. Masiero, Phys. Lett. B **206**, 480 (1988).

[10] I. Antoniadis, E. Gava, K. S. Narain and T. R. Taylor, Nucl. Phys. B **432**, 187 (1994) [arXiv:hep-th/9405024].

[11] R. Barbieri, S. Ferrara and C.A. Savoy, Phys. Lett. **B119**, 343 (1982).

[12] L. Hall, J. Lykken and S. Weinberg, Phys. Rev. **D27**, 2359 (1983).

[13] P. Nath, R. L. Arnowitt and A. H. Chamseddine, Nucl. Phys. B **227**, 121 (1983).

[14] H. P. Nilles, Phys. Rept. **110**, 1 (1984); H. E. Haber and G. L. Kane, Phys. Rept. **117**, 75 (1985).

[15] P. Nath, "Twenty years of SUGRA," arXiv:hep-ph/0307123.

[16] R. L. Arnowitt and P. Nath, "Supersymmetry and supergravity: Phenomenology and grand unification," arXiv:hep-ph/9309277.

[17] S. P. Martin, "A supersymmetry primer," arXiv:hep-ph/9709356; Howard Baer and Xerxes Tata, Weak Scale Supersymmetry: From Superfields to Scattering Events (Cambridge University Press, May 29, 2006); Manuel Drees, Rohini Godbole, and Probir Roy, Theory and Phenomenology of Sparticles (World Scientific Publishing Company, 1st edition, November 15, 2004).

[18] A small sample of early works on the phenomenological implications of SUGRA models consists of S. Weinberg, Phys. Rev. Lett. **50**, 387 (1983); R. Arnowitt, A. H. Chamseddine and P. Nath, Phys. Rev. Lett. **50** (1983) 232; A. H. Chamseddine, P. Nath and R. Arnowitt, Phys. Lett. B **129** (1983) 445 [Erratum-ibid. B **132** (1983) 467]; P. Nath, R. Arnowitt and A. H. Chamseddine, Phys. Lett. B **121** (1983) 33; P. Nath, R. Arnowitt and A. H. Chamseddine, HUTP-83/A077; D. A. Dicus, S. Nandi, W. W. Repko and X. Tata, Phys. Rev. Lett. **51**, 1030 (1983); Phys. Rev. D **29**, 67 (1984); Phys. Rev. D **29**, 1317 (1984); D. A. Dicus, S. Nandi and X. Tata, Phys. Lett. B **129**, 451 (1983); J. M. Frere and G. L. Kane, Nucl. Phys. B **223**, 331 (1983); H. Goldberg, Phys. Rev. Lett. **50**, 1419 (1983); J. R. Ellis, J. M. Frere, J. S. Hagelin, G. L. Kane and S. T. Petcov, Phys. Lett. B **132**, 436 (1983); J. R. Ellis, J. S. Hagelin, D. V. Nanopoulos and M. Srednicki, Phys. Lett. B **127**, 233 (1983); M. K. Gaillard, L. J. Hall, B. Zumino, F. del Aguila, J. Polchinski and G. G. Ross, Phys. Lett. B **122**, 355 (1983);

[19] U. Chattopadhyay, A. Corsetti and P. Nath, Phys. Rev. D **68**, 035005 (2003); J. R. Ellis, K. A. Olive, Y. Santoso and V. C. Spanos, Phys. Lett. B **565**, 176 (2003); H. Baer, A. Belyaev, T. Krupovnickas and J. O'Farrill, JCAP **0408**, 005 (2004); J. Edsjo, M. Schelke, P. Ullio and P. Gondolo, JCAP **0304**, 001 (2003); P. Gondolo, J. Edsjo, P. Ullio, L. Bergstrom, M. Schelke and E. A. Baltz, JCAP **0407**, 008 (2004); Y. Mambrini and E. Nezri, [hep-ph/0507263]; M. M. Nojiri, G. Polesello and D. R. Tovey, JHEP **0603**, 063 (2006); J. L. Feng, A. Rajaraman and B. T. Smith, Phys. Rev. D **74**, 015013 (2006); A. Belyaev, S. Dar, I. Gogoladze, A. Mustafayev and Q. Shafi, arXiv:0712.1049 [hep-ph].

[20] L. Roszkowski, R. Ruiz de Austri and R. Trotta, JHEP **0707** (2007) 075; R. R. de Austri, R. Trotta and L. Roszkowski, JHEP **0605**, 002 (2006).

[21] B. C. Allanach, C. G. Lester and A. M. Weber, JHEP **0612**, 065 (2006); B. C. Allanach, K. Cranmer, C. G. Lester and A. M. Weber, JHEP **0708**, 023 (2007);

[22] D. Feldman, Z. Liu and P. Nath, Phys. Rev. Lett. **99**, 251802 (2007) [Erratum-ibid. **100**, 069902 (2008)] [arXiv:0707.1873 [hep-ph]].

[23] D. Feldman, Z. Liu and P. Nath, Phys. Lett. B **662**, 190 (2008) [arXiv:0711.4591 [hep-ph]].

[24] D. Feldman, Z. Liu and P. Nath, JHEP **0804**, 054 (2008) [arXiv:0802.4085 [hep-ph]].

[25] D. Feldman, Z. Liu and P. Nath, arXiv:0806.4683 [hep-ph].

[26] D. Feldman, Z. Liu and P. Nath, arXiv:0808.1595 [hep-ph].

[27] P. Nath and R. Arnowitt, Phys. Rev. D **56**, 2820 (1997); A. Birkedal-Hansen and B. D. Nelson, Phys. Rev. D **67**, 095006 (2003); U. Chattopadhyay and D. P. Roy, Phys. Rev. D **68**, 033010 (2003); D. G. Cerdeno and C. Munoz, JHEP **0410**, 015 (2004); G. Belanger, F. Boudjema, A. Cottrant, A. Pukhov and A. Semenov, Nucl. Phys. B **706**, 411 (2005); H. Baer, A. Mustafayev, S. Profumo, A. Belyaev and X. Tata, JHEP **0507**, 065 (2005).

[28] B. Kors and P. Nath, Nucl. Phys. B **711**, 112 (2005).

[29] D. Feldman, B. Kors and P. Nath, Phys. Rev. D **75** (2007) 023503.

[30] V. Barger, C. Kao, P. Langacker and H. S. Lee, Phys. Lett. B **600**, 104 (2004).

[31] J. R. Ellis, S. Heinemeyer, K. A. Olive and G. Weiglein, JHEP **0502**, 013 (2005).

[32] L. S. Stark, P. Hafliger, A. Biland and F. Pauss, JHEP **0508**, 059 (2005).

[33] A. Djouadi, M. Drees and J. L. Kneur, JHEP **0603**, 033 (2006).

[34] J. R. Ellis, S. Heinemeyer, K. A. Olive and G. Weiglein, JHEP **0605**, 005 (2006).

[35] U. Chattopadhyay, D. Das, A. Datta and S. Poddar, Phys. Rev. D **76**, 055008 (2007).

[36] T. Bringmann, L. Bergstrom and J. Edsjo, JHEP **0801**, 049 (2008) [arXiv:0710.3169 [hep-ph]].

[37] N. Bhattacharyya, A. Datta and S. Poddar, arXiv:0807.0278 [hep-ph].

[38] S. P. Martin and P. Ramond, Phys. Rev. D **48**, 5365 (1993).

[39] M. R. Douglas and S. Kachru, Rev. Mod. Phys. **79**, 733 (2007) [arXiv:hep-th/0610102].

[40] S. P. Martin and M. T. Vaughn, Phys. Rev. D **50**, 2282 (1994) [arXiv:hep-ph/9311340]; M. E. Machacek and M. T. Vaughn, Nucl. Phys. B **249**, 70 (1985); M. E. Machacek and M. T. Vaughn, Nucl. Phys. B **236**, 221 (1984);

[41] S. R. Coleman and E. Weinberg, Phys. Rev. D **7**, 1888 (1973).

[42] R. L. Arnowitt and P. Nath, Phys. Rev. D **46**, 3981 (1992).

[43] L. Alvarez-Gaume, J. Polchinski and M. B. Wise, Nucl. Phys. B **221**, 495 (1983).

[44] L. E. Ibanez and G. G. Ross, Comptes Rendus Physique **8**, 1013 (2007) [arXiv:hep-ph/0702046].

[45] K. L. Chan, U. Chattopadhyay and P. Nath, Phys. Rev. D **58**, 096004 (1998); J. L. Feng, K. T. Matchev and T. Moroi, Phys. Rev. Lett. **84**, 2322 (2000); H. Baer, C. Balazs, A. Belyaev, T. Krupovnickas and X. Tata, JHEP **0306**, 054 (2003).

[46] For a review see, A. B. Lahanas, N. E. Mavromatos and D. V. Nanopoulos, Int. J. Mod. Phys. D **12** (2003) 1529.

[47] L. E. Ibanez, C. Lopez and C. Munoz, Nucl. Phys. B **256**, 218 (1985).

[48] P. Nath and T. R. Taylor, Phys. Lett. B **548**, 77 (2002) [arXiv:hep-ph/0209282].

[49] U. Chattopadhyay and P. Nath, Phys. Rev. D **70**, 096009 (2004) [arXiv:hep-ph/0405157].

[50] B. Kors and P. Nath, Nucl. Phys. B **681**, 77 (2004) [arXiv:hep-th/0309167].

[51] D. Lust, S. Reffert and S. Stieberger, Nucl. Phys. B **727**, 264 (2005) [arXiv:hep-th/0410074].

[52] G. L. Kane, P. Kumar, J. D. Lykken and T. T. Wang, Phys. Rev. D **71**, 115017 (2005) [arXiv:hep-ph/0411125].

[53] B. W. Lee and S. Weinberg, Phys. Rev. Lett. **38**, 1237 (1977).

[54] K. A. Olive, D. N. Schramm and G. Steigman, Nucl. Phys. B **180**, 497 (1981).

[55] H. Baer and M. Brhlik, Phys. Rev. D **53**, 597 (1996) [arXiv:hep-ph/9508321].

[56] K. Griest and D. Seckel, Phys. Rev. D **43**, 3191 (1991).

[57] P. Gondolo and G. Gelmini, Nucl. Phys. B **360**, 145 (1991).

[58] R. L. Arnowitt and P. Nath, Phys. Lett. B **299**, 58 (1993) [Erratum-ibid. B **307**, 403 (1993)] [arXiv:hep-ph/9302317].

[59] P. Nath and R. L. Arnowitt, Phys. Rev. Lett. **70**, 3696 (1993) [arXiv:hep-ph/9302318].

[60] S. Mizuta and M. Yamaguchi, Phys. Lett. B **298**, 120 (1993);

[61] J. R. Ellis, T. Falk and K. A. Olive, Phys. Lett. B **444** (1998) 367; J. R. Ellis, T. Falk, K. A. Olive and M. Srednicki, Astropart. Phys. **13**, 181 (2000);

[62] T. Nihei, L. Roszkowski and R. Ruiz de Austri, JHEP **0207**, 024 (2002) [arXiv:hep-ph/0206266].

[63] G. Belanger, F. Boudjema, A. Pukhov and A. Semenov, Comput. Phys. Commun. **176**, 367 (2007); G. Belanger, F. Boudjema, A. Pukhov and A. Semenov, Comput. Phys. Commun. **174**, 577 (2006); G. Belanger, F. Boudjema, A. Pukhov and A. Semenov, Comput. Phys. Commun. **149** (2002) 103.

[64] U. Chattopadhyay, A. Corsetti and P. Nath, Phys. Rev. D **66**, 035003 (2002) [arXiv:hep-ph/0201001].

[65] T. Ibrahim and P. Nath, Rev. Mod. Phys. **80**, 577 (2008) [arXiv:0705.2008 [hep-ph]].

[66] J. Ellis, J. S. Lee and A. Pilaftsis, arXiv:0808.1819 [hep-ph].

[67] P. Nath, Phys. Rev. Lett. **66**, 2565 (1991); Y. Kizukuri and N. Oshimo, Phys. Rev. D **46**, 3025 (1992).

[68] T. Ibrahim and P. Nath, Phys. Lett. B **418**, 98 (1998) [arXiv:hep-ph/9707409].; Phys. Rev. D **57**, 478 (1998) [arXiv:hep-ph/9708456]; Phys. Rev. D **58**, 111301 (1998) [arXiv:hep-ph/9807501]; M. Brhlik, G. J. Good and G. L. Kane, Phys. Rev. D **59**, 115004 (1999) [arXiv:hep-ph/9810457].

[69] A. Pilaftsis, Phys. Rev. D **58**, 096010 (1998) [arXiv:hep-ph/9803297]; A. Pilaftsis and C. E. M. Wagner, Nucl. Phys. B **553**, 3 (1999) [arXiv:hep-ph/9902371]; A. Pilaftsis and C. E. M. Wagner, Nucl. Phys. B **553**, 3 (1999) [arXiv:hep-ph/9902371]; S. Y. Choi, M. Drees and J. S. Lee, Phys. Lett. B **481**, 57 (2000) [arXiv:hep-ph/0002287]. T. Ibrahim and P. Nath, Phys. Rev. D **63**, 035009 (2001) [arXiv:hep-ph/0008237]; Phys. Rev. D **66**, 015005 (2002) [arXiv:hep-ph/0204092].

[70] P. Nath and P. Fileviez Perez, Phys. Rept. **441**, 191 (2007) [arXiv:hep-ph/0601023].

[71] D. N. Spergel *et al.* [WMAP Collaboration], Astrophys. J. Suppl. **170**, 377 (2007).

[72] G. Degrassi, P. Gambino and G. F. Giudice, JHEP **0012** (2000) 009; A. J. Buras et.al., Nucl. Phys. B **659** (2003) 3; M. E. Gomez, T. Ibrahim, P. Nath and S. Skadhauge, Phys. Rev. D **74** (2006) 015015; G. Degrassi, P. Gambino and P. Slavich, Phys. Lett. B **635** (2006) 335.

[73] E. Barberio *et al.* [Heavy Flavor Averaging Group (HFAG) Collaboration], arXiv:0704.3575 [hep-ex].

[74] M. Misiak *et al.*, Phys. Rev. Lett. **98** (2007) 022002.

[75] S. R. Choudhury and N. Gaur, Phys. Lett. B **451**, 86 (1999); C. Bobeth, T. Ewerth, F. Kruger and J. Urban, Phys. Rev. D **64**, 074014 (2001).

[76] V. M. Abazov *et al.* [D0 Collaboration], Phys. Rev. D **76**, 092001 (2007).

[77] CDF Public Note 8956; DØ Conference Note 5344-CONF; [CDF Collaboration], arXiv:0712.1708 [hep-ex].

[78] K. Anikeev *et al.*, "B physics at the Tevatron: Run II and beyond," [arXiv:hep-ph/0201071].

[79] R. Barate *et al.* [LEP Working Group for Higgs boson searches], Phys. Lett. B **565**, 61 (2003); The ALEPH, DELPHI, L3 and OPAL Collaborations, LHWG-Note 2005-01.

[80] G. Abbiendi *et al.* [OPAL Collaboration], arXiv:0707.0373 [hep-ex].

[81] G. Abbiendi *et al.* [OPAL Collaboration], Eur. Phys. J. C **35**, 1 (2004);

[82] T. C. Yuan, R. Arnowitt, A. H. Chamseddine and P. Nath, Z. Phys. C **26**, 407 (1984); D. A. Kosower, L. M. Krauss and N. Sakai, Phys. Lett. B **133**, 305 (1983); J. L. Lopez, D. V. Nanopoulos and X. Wang, Phys. Rev. D **49**, 366 (1994); U. Chattopadhyay and P. Nath, Phys. Rev. D **53**, 1648 (1996); T. Moroi, Phys. Rev. D **53**, 6565 (1996) [Erratum-ibid. D **56**, 4424 (1997)]; T. Ibrahim and P. Nath, Phys. Rev. D **61** (2000) 095008 [arXiv:hep-ph/9907555].

[83] K. Hagiwara, A. D. Martin, D. Nomura and T. Teubner, Phys. Lett. B **649**, 173 (2007).

[84] A. Djouadi, J. L. Kneur and G. Moultaka, Comput. Phys. Commun. **176**, 426 (2007).

[85] F. E. Paige, S. D. Protopopescu, H. Baer and X. Tata, arXiv:hep-ph/0312045.

[86] W. Porod, Comput. Phys. Commun. **153**, 275 (2003).

[87] B. C. Allanach, Comput. Phys. Commun. **143**, 305 (2002).

[88] P. Nath, J. z. Wu and R. Arnowitt, Phys. Rev. D **52** (1995) 4169 [arXiv:hep-ph/9502388]; B. Allanach, S. Kraml and W. Porod, [hep-ph/0207314]; J. R. Ellis, K. A. Olive, Y. Santoso and V. C. Spanos, Phys. Rev. D **69**, 095004 (2004); M. E. Gomez, T. Ibrahim, P. Nath and S. Skadhauge, Phys. Rev. D **70**, 035014 (2004); J. R. Ellis, S. Heinemeyer, K. A. Olive and G. Weiglein, JHEP **0502**, 013 (2005).

[89] H. Baer, J. Ferrandis, S. Kraml and W. Porod, Phys. Rev. D **73**, 015010 (2006).

[90] G. Belanger, S. Kraml and A. Pukhov, Phys. Rev. D **72**, 015003 (2005).

[91] B. C. Allanach, A. Djouadi, J. L. Kneur, W. Porod and P. Slavich, JHEP **0409**, 044 (2004).

[92] B. C. Allanach, S. Kraml and W. Porod, JHEP **0303**, 016 (2003). and arXiv:hep-ph/0207314.

[93] R. Arnowitt *et al.*, Phys. Lett. B **649**, 73 (2007); R. Arnowitt, B. Dutta, A. Gurrola, T. Kamon, A. Krislock and D. Toback, arXiv:0802.2968 [hep-ph].

[94] G. J. Gounaris, J. Layssac and F. M. Renard, Phys. Rev. D **77**, 013003 (2008).

[95] O. Buchmueller *et al.*, Phys. Lett. B **657**, 87 (2007).

[96] S. P. Martin, Phys. Rev. D **75**, 115005 (2007) [arXiv:hep-ph/0703097]; Phys. Rev. D **76**, 095005 (2007) [arXiv:0707.2812 [hep-ph]]; Phys. Rev. D **77**, 075002 (2008) [arXiv:0801.0237 [hep-ph]]; arXiv:0807.2820 [hep-ph].

[97] A. V. Gladyshev, D. I. Kazakov and M. G. Paucar, arXiv:0704.1429 [hep-ph].

[98] B. C. Allanach *et al.*, [arXiv:hep-ph/0202233].

[99] M. Battaglia, A. De Roeck, J. R. Ellis, F. Gianotti, K. A. Olive and L. Pape, Eur. Phys. J. C **33**, 273 (2004).

[100] G. L. Bayatian *et al.* [CMS Collaboration], J. Phys. G **34**, 995 (2007).

[101] J. Hubisz, J. Lykken, M. Pierini and M. Spiropulu, arXiv:0805.2398 [hep-ph].

[102] M. Spiropulu, arXiv:0801.0318 [hep-ex].

[103] G. Barenboim, P. Paradisi, O. Vives, E. Lunghi and W. Porod, arXiv:0712.3559 [hep-ph].

[104] J. R. Ellis, S. Heinemeyer, K. A. Olive and G. Weiglein, Phys. Lett. B **653**, 292 (2007).

[105] J. M. Frere, D. R. T. Jones and S. Raby, Nucl. Phys. B **222**, 11 (1983);

[106] J. A. Casas, A. Lleyda and C. Munoz, Nucl. Phys. B **471**, 3 (1996)

[107] A. Kusenko, P. Langacker and G. Segre, Phys. Rev. D **54**, 5824 (1996) [arXiv:hep-ph/9602414].

[108] J. R. Ellis, T. Falk, K. A. Olive and M. Srednicki, Astropart. Phys. **13**, 181 (2000) [Erratum-ibid. **15**, 413 (2001)].

[109] M. E. Gomez, G. Lazarides and C. Pallis, Phys. Lett. B **487**, 313 (2000)

[110] P. Skands *et al.*, JHEP **0407**, 036 (2004).

[111] T. Sjostrand, S. Mrenna, P. Skands, JHEP **0605**, 026 (2006).

[112] http://www.physics.ucdavis.edu/∼conway/research/software/pgs/pgs4-general.htm

[113] W. Beenakker, M. Klasen, M. Kramer, T. Plehn, M. Spira and P. M. Zerwas, Phys. Rev. Lett. **83**, 3780 (1999).

[114] S. Jadach, Z. Was, R. Decker and J. H. Kuhn, Comput. Phys. Commun. **76**, 361 (1993).

[115] CMS Collaboration, CERN/LHCC 2006-001 (2006).

[116] M. Chiorboli, M. Galanti, A. Tricomi, CMS NOTE 2006/133

[117] D. J. Mangeol, U. Goerlach, CMS NOTE 2006/096

[118] W. de Boer, et. al, CMS NOTE 2006/113

[119] N. Arkani-Hamed, G. L. Kane, J. Thaler and L. T. Wang, JHEP **0608**, 070 (2006).

[120] G. L. Kane, P. Kumar and J. Shao, J. Phys. G **34**, 1993 (2007).

[121] J. P. Conlon, C. H. Kom, K. Suruliz, B. C. Allanach and F. Quevedo, JHEP **0708**, 061 (2007)

[122] H. Baer, V. Barger, G. Shaughnessy, H. Summy and L. t. Wang, Phys. Rev. D **75**, 095010 (2007).

[123] P. G. Mercadante, J. K. Mizukoshi and X. Tata, Braz. J. Phys. **37** (2007) 549.

[124] R. Kitano and Y. Nomura, Phys. Rev. D **73**, 095004 (2006) [arXiv:hep-ph/0602096].

[125] H. Baer, K. Hagiwara and X. Tata, Phys. Rev. D **35**, 1598 (1987).

[126] P. Nath and R. Arnowitt, Mod. Phys. Lett. A **2**, 331 (1987); R. Arnowitt, R. M. Barnett, P. Nath and F. Paige, Int. J. Mod. Phys. A **2**, 1113 (1987); H. Baer, C. h. Chen, F. Paige and X. Tata, Phys. Rev. D **50**, 4508 (1994); V. D. Barger, C. Kao and T. j. Li, Phys. Lett. B **433**, 328 (1998); H. Baer, M. Drees, F. Paige, P. Quintana and X. Tata, Phys. Rev. D **61** (2000) 095007.

[127] G. J. Gounaris, J. Layssac and F. M. Renard, Phys. Rev. D **77**, 093007 (2008) [arXiv:0803.0813 [hep-ph]].

[128] G. L. Kane, B. D. Nelson, T. T. Wang and L. T. Wang, arXiv:hep-ph/0304134.

[129] M. S. Carena, D. Hooper and P. Skands, Phys. Rev. Lett. **97** (2006) 051801; M. S. Carena, D. Hooper and A. Vallinotto, Phys. Rev. D **75**, 055010 (2007).

[130] V. M. Abazov *et al.* [D0 Collaboration], Phys. Rev. Lett. **97**, 121802 (2006).

[131] J. Campbell, R. K. Ellis, F. Maltoni and S. Willenbrock, Phys. Rev. D **67** (2003) 095002; R. V. Harlander and W. B. Kilgore, Phys. Rev. D **68**, 013001 (2003); F. Maltoni, Z. Sullivan and S. Willenbrock, Phys. Rev. D **67** (2003) 093005; S. Dawson, C. B. Jackson, L. Reina and D. Wackeroth, Mod. Phys. Lett. A **21** (2006) 89; U. Aglietti *et al.*, arXiv:hep-ph/0612172.

[132] CDF Public Note 8594 v1.0; A. Anastassov, Aspen 2008 Winter Conference: "Revealing the Nature of Electroweak Symmetry Breaking".

[133] S. R. Choudhury and N. Gaur, Phys. Lett. B **451**, 86 (1999); K. S. Babu and C. Kolda, Phys. Rev. Lett. **84**, 228 (2000); A. Dedes, H. K. Dreiner, U. Nierste, and P. Richardson, Phys. Rev. Lett. **87**, 251804 (2001); R. Arnowitt, B. Dutta, T. Kamon and M. Tanaka, Phys. Lett. B **538** (2002) 121; S. Baek, P. Ko, and W. Y. Song, JHEP **0303**, 054 (2003); J. K. Mizukoshi, X. Tata and Y. Wang, Phys. Rev. D **66**, 115003 (2002); T. Ibrahim and P. Nath, Phys. Rev. D **67**, 016005 (2003).

[134] T. Ibrahim and P. Nath, Phys. Rev. D **67**, 016005 (2003) [arXiv:hep-ph/0208142].

[135] R. Bernhard *et al.* [CDF Collaboration], arXiv:hep-ex/0508058.

[136] A. Abulencia *et al.* [CDF Collaboration], Phys. Rev. Lett. **95** (2005) 221805 [Erratum-ibid. **95** (2005) 249905] [arXiv:hep-ex/0508036].

[137] U. Chattopadhyay, T. Ibrahim and P. Nath, Phys. Rev. D **60** (1999) 063505.

[138] A. Corsetti and P. Nath, Phys. Rev. D **64**, 125010 (2001) [arXiv:hep-ph/0003186].

[139] S. Baek, D. G. Cerdeno, Y. G. Kim, P. Ko and C. Munoz, JHEP **0506** (2005) 017; D. G. Cerdeno and C. Munoz, JHEP **0410** (2004) 015; D. G. Cerdeno, T. Kobayashi and C. Munoz, arXiv:0709.0858 [hep-ph]; R. Arnowitt, B. Dutta and Y. Santoso, Nucl. Phys. B **606** (2001) 59.

[140] B. C. Allanach and D. Hooper, arXiv:0806.1923 [hep-ph].

[141] V. Barger, W. Y. Keung and G. Shaughnessy, arXiv:0806.1962 [hep-ph].

[142] B. Altunkaynak, M. Holmes and B. D. Nelson, arXiv:0804.2899 [hep-ph].

[143] R. W. Schnee *et al.* [The SuperCDMS Collaboration], arXiv:astro-ph/0502435.

[144] M. Atac *et al.*, New Astron. Rev. **49** (2005) 283.

[145] T. Stiegler et.al., Fall Meeting of the Texas Sections of the APS and AAPT, 2007.

[146] R. Bernabei *et al.*, Phys. Lett. B **389** (1996) 757.

[147] V. Sanglard *et al.* [The EDELWEISS Collaboration], Phys. Rev. D **71** (2005) 122002.

[148] D. S. Akerib *et al.* [CDMS Collaboration], Phys. Rev. Lett. **96** (2006) 011302.

[149] G. J. Alner *et al.*, Astropart. Phys. **28** (2007) 287; Astropart. Phys. **23** (2005) 444.

[150] J. Angle *et al.* [XENON Collaboration], arXiv:0706.0039 [astro-ph].

[151] P. Nath and R. Arnowitt, Phys. Rev. D **56**, 2820 (1997).

[152] S. Profumo and C. E. Yaguna, Phys. Rev. D **69**, 115009 (2004) [arXiv:hep-ph/0402208].